National Library
of Canada

Acquisitions and
Bibliographic Services Branch

395 Wellington Street
Ottawa, Ontario
K1A 0N4

Bibliothèque nationale
du Canada

Direction des acquisitions et
des services bibliographiques

395, rue Wellington
Ottawa (Ontario)
K1A 0N4

Your file Votre référence

Our file Notre référence

NOTICE

The quality of this microform is heavily dependent upon the quality of the original thesis submitted for microfilming. Every effort has been made to ensure the highest quality of reproduction possible.

If pages are missing, contact the university which granted the degree.

Some pages may have indistinct print especially if the original pages were typed with a poor typewriter ribbon or if the university sent us an inferior photocopy.

Reproduction in full or in part of this microform is governed by the Canadian Copyright Act, R.S.C. 1970, c. C-30, and subsequent amendments.

AVIS

La qualité de cette microforme dépend grandement de la qualité de la thèse soumise au microfilmage. Nous avons tout fait pour assurer une qualité supérieure de reproduction.

S'il manque des pages, veuillez communiquer avec l'université qui a conféré le grade.

La qualité d'impression de certaines pages peut laisser à désirer, surtout si les pages originales ont été dactylographiées à l'aide d'un ruban usé ou si l'université nous a fait parvenir une photocopie de qualité inférieure.

La reproduction, même partielle, de cette microforme est soumise à la Loi canadienne sur le droit d'auteur, SRC 1970, c. C-30, et ses amendements subséquents.

Canada

University of Alberta

Bifurcations in the Convective Heat Transfer of Internally Heated Porous Layers and Hele-Shaw Cells

by

Donald K. Ryland

A thesis
submitted to the Faculty of Graduate Studies and Research
in partial fulfillment of the requirements for the degree of

Doctor of Philosophy

Department of Chemical Engineering

Edmonton, Alberta

Fall 1992

National Library
of Canada

Acquisitions and
Bibliographic Services Branch

395 Wellington Street
Ottawa, Ontario
K1A 0N4

Bibliothèque nationale
du Canada

Direction des acquisitions et
des services bibliographiques

395, rue Wellington
Ottawa (Ontario)
K1A 0N4

Your file Votre référence

Our file Notre référence

ISBN 0-315-77405-3

Canada

University of Alberta

Release Form

Name of Author:	**Donald K. Ryland**
Title of Thesis:	**Bifurcations in the Convective Heat Transfer of Internally Heated Porous Layers and Hele-Shaw Cells**
Degree:	Doctor of Philosophy
Year this degree granted:	Fall 1992

Permission is hereby granted to the **University of Alberta Library** to reproduce single copies of this thesis and to lend or sell such copies for private, scholarly or scientific research purposes only.

The author reserves all other publication and other rights in association with the copyright in the thesis, and except as hereinbefore provided neither the thesis nor any substantial portion thereof may be printed or otherwise reproduced in any material form whatever without the author's prior written permission.

....

(Student's signature)

Donald K. Ryland

1417 Avenue B North

Saskatoon, Saskatchewan

Canada

S7L 1G7

Date : OCTOBER 7 1992

University of Alberta
Faculty of Graduate Studies and Research

The undersigned certify that they have read, and recommend to the Faculty of Graduate Studies and Research for acceptance, a thesis entitled **Bifurcations in the Convective Heat Transfer of Internally Heated Porous Layers and Hele-Shaw Cells** submitted by **Donald K. Ryland** in partial fulfillment of the requirements for the degree of **Doctor of Philosophy**.

K. Nandakumar (Supervisor)

A. Jeje (University of Calgary)

J. H. Masliyah

W. H. Finlay

R. E. Hayes

Date : Oct. 6/92

Abstract

The steady natural convective heat transfer driven by internal heat sources in a rectangular finite geometry is examined. Bifurcation diagrams have been constructed in the case of a porous slab and a thin fluid layer using recently developed algorithms from bifurcation theory. In both cases, there is a uniform peripheral temperature. Tilt is an important factor in these systems, as it breaks the reflective symmetry in the system and unfolds the bifurcation diagram. This unfolding provides additional clues on the evolution of various structures. Hence, the effect of tilt on the solution structure has also been investigated.

As the porous slab is tilted, there is significant change in the stationary solution structure. Tilting the slab results in the evolution of the stationary structure from two isolated symmetric and six asymmetric branches for the untilted slab to seven isolated branches for the porous layer tilted one degree. At every angle of tilt, a primary solution branch exists with a unique solution region. As the slab is tilted to higher angles, the unique solution region increases. At 45° of tilt, this primary branch is always unique and the flows are globally stable. Several origins of Hopf bifurcations were also located. As the slab is tilted, these Hopf points move to higher Rayleigh numbers and will cross the stationary solution branches, causing these solution branches to become unstable.

A mathematical model for natural convective flow driven by internal heating in a vertical Hele-Shaw cell was developed. The stationary solution structure for an untilted fluid layer is qualitatively similar to that for a porous slab, although the former is derived from the Navier-Stokes equation, and the latter from the Darcy equation. A quantitative comparison shows that the bifurcation points in the porous layer structure are a limiting case for the fluid layer bifurcation points as the width of the gap approaches zero.

A vertical Hele-Shaw cell has been constructed to match the geometry of the fluid layer studied numerically. Flow patterns within the fluid layer are observed through the use of flow visualization. The unique solution region for an untilted layer was found to end at a Grashof number of 138000, which is 16% less than the numerical prediction of 165591. The range of stable two cell flows did not exist past a Grashof number of 283000 in the experimental study, while the simulations predicted stable two cell flows until a Grashof number of 300034. The difference in these values is 6%. The discrepancies between the numerically predicted limit points and the bounds on the experimental solution branches for the two and four cell flows are within the range of errors calculated for the experimental Grashof numbers.

Acknowledgments

The first person I must acknowledge is my thesis supervisor, Dr. K. Nandakumar. It has been his guidance and incredible patience that have helped me to mature as not only a researcher, but also as a person. Without him and his commitment to quality, this thesis would not have been possible. The other members of my supervisory committee, Dr. J. H. Masliyah and Dr. W. Finlay, also deserve thanks for their less extensive, but no less important, roles in the completion of this project.

Construction of my experimental apparatus and the purchasing of the computers to perform the numerical analysis was due to the financial support given by NSERC to Dr. Nandakumar in the form of equipment and operating grants. I must also thank the Department of Chemical Engineering for the Greenhalgh Scholarship, and the Faculty of Engineering for the Leonard E. Gads Teaching Assistant Award, each in 1989.

I am indebted to the people who have helped me with the construction and debugging of my equipment. This includes Bob Scott, Keith Faulder and Ron van den Heuvel in the Chemical Engineering Machine Shop for building the apparatus, as well as Don Sutherland, Walter Boddez and Richard Cooper in the Instrument Shop for ordering the instrumentation and fixing all the soldering mistakes I made. Special thanks to Bob Barton in the DACS Centre for writing the data acquisition routine for the experiments (twice), Barry Bara for his donation of the thesis macros and

helpful suggestions concerning the experimental program, the people from Photo Services for their patience and understanding, and Andrée Koenig for providing copper sulfate crystals and distilled water months before they were needed.

As well, the office staff of Bev Walker, Mildred Demers, Cindy Heisler, Audrey Mayes, and Laurie Heidebrecht must be mentioned for all their help in dealing with tedious administrative matters, and for providing me with new recipes for my collection.

There are many fellow graduate students who made it fun to be here. Paul Nawrocki, my office mate for four years, deserves great recognition for listening to my ramblings and never saying an ill word. Luigi Boccanfuso, Lyle Trytten, Greg Holloway, Dave Shook, Wellington Kwok, Philip Mees, and Kevin Dorma, among others, have shown me that you can have fun in graduate school, and in many cases more can be learned outside of the classroom and lab than inside it.

I owe a big debt of gratitude to my family in Saskatoon. My Mom (†) and Dad, along with my sisters Bette and Lori and my brother-in-law Dave, were a constant source of support, and they never asked questions when they tried to phone me for two hours while the line was busy as I was hooked up to the workstation through my modem. An equally large debt must be paid to Kendra Whitfield, who had no idea what I was doing, but nevertheless wanted to hear all about it.

Finally, a special mention must be made of Dr. Hubert Weinitschke, who passed away last December. I had only brief contact with him, but found him to be very wise and inspirational. He has my eternal gratitude, as it was through an algorithm he developed that I was able to generate much of the simulation data in this thesis.

Contents

Chapter 1

Chapter 2

Chapter 3

Chapter 4

Chapter 6

Chapter 7

List of Tables

List of Figures

Nomenclature

a	half-height of domain (m)
A'	dimensional area of the domain (m^2)
b	half-length of domain (m)
C_p	heat capacity (J/kgK)
d	spacing between vertical plates (m)
D, P	correction terms for (θ, ψ) in Newton method
g	gravity (m/s^2)
Gr	Grashof number, dynamic parameter for Hele-Shaw study
k	thermal conductivity (W/mK)
K	permeability (m^2)
Nu	Nusselt number
Q_g	rate of internal heating per unit volume of medium (W/m^3)
Ra	Rayleigh number, dynamic parameter for porous study
$\overline{T}$	temperature averaged across the fluid gap (K)
T	temperature (K)
t	time (s)
u	velocity component in x-direction (m/s)
$\mathbf{U}$	velocity vector using "small gap approximation" (m/s)

v	velocity component in y-direction (m/s)
x	direction along the length of the cell(m)
y	direction along the height of the cell(m)
$<>$	averaged quantity

Subscripts

b	bulk quantity
eff	effective property in the porous layer
f	fluid property
o	reference value
w	quantity at the wall
x	derivative with respect to x
y	derivative with respect to y

Superscripts

$'$	dimensional quantity
H	quantity for Hele-Shaw cell
P	quantity for porous layer

Greek

α	thermal diffusivity $(k/(rhoC_p)_f\ (m^2/s))$
β	coefficient of thermal expansion $(1/K)$
γ	aspect ratio (b/a)
Δ	Laplacian operator

ψ	stream function
θ	dimensionless temperature
ϕ	tilt angle above the horizontal (°)
μ	dynamic viscosity (kg/ms)
ν	kinematic viscosity (m^2/s)
ρ_f	density of fluid (kg/m^3)
Ω	vorticity
∇	gradient operator
σ	ratio of the thermal masses of porous medium and fluid $((\rho C_p)_m/(\rho C_p)_f)$

Chapter 1

Introduction

1.1 Background

There has been a great deal of interest in describing convective behavior within fluid-saturated porous media. The resulting enhancement in heat transfer is important in applications such as thermal methods of enhanced oil recovery and geothermal processes. Limiting this heat transfer is important in the design of thermal insulation systems. In addition, there is a fundamental curiousity about the physics of flow and heat transfer through a porous layer.

Major questions need to be resolved in the modelling of the flow and heat transfer within a porous medium. The flow is too complex to be described fully on a microscopic scale, but macroscopic equations are limited in applicability. For example, the computationally simple Darcy equation is applicable for slow flows in infinite media. Forchheimer and Brinkman suggested terms to account for fluid inertia and boundary effects, respectively, which are improvements on the Darcy equation.

To describe the heat transfer within a porous layer, expressions analogous to those used in fluid layers have been successful. Fourier's law of conduction is applied by implementing an effective thermal conductivity which incorporates the thermal characteristics of both the fluid and solid phases. The heterogeneous nature of the solid matrix and the fluid in a porous layer prevents the development of a simple expression for thermal conductivity. Simple approximations for the value of effective thermal conductivity yield unreasonable results. Thus, experimental measurement is the common method for determining the effective thermal conductivity of a porous layer.

Nevertheless, it is possible to obtain a reasonable description of the flow of fluid and heat within a porous layer. In the case of flow driven by natural convection, Darcy's equation is a good approximation due to the low velocities. If the fluid and solid phases of the medium have thermal conductivities of the same order of magnitude, a reasonable value of effective thermal conductivity for the porous layer may be obtained.

Another approximation for flow in a porous layer is through the use of a thin fluid gap. This idea comes from the close analogy between the mathematical expressions of the Darcy equation and the Navier-Stokes equation for isothermal flow between closely spaced plates. A thin fluid gap, also known as a Hele-Shaw cell, has been used successfully to learn about convection and two-phase displacement in porous layers. There are limits to the applicability of this analogy, and these factors have been extensively discussed by Koster and Müller [1, 2].

Previous studies of convection in both fluid and porous layers have usually dealt with the situation where the bottom of the layer is heated and the top is cooled. The resulting density inversion drives the convection. This situation has been extensively studied to find important practical information such as the stability of the discovered flows. Fundamental studies of porous layers heated from below have dealt with several phenomena. In addition to studies of the onset of convection and steady-state convective solutions, bifurcations of these steady solutions have been located. Some bifurcations have presented opportunites to study periodic states. Investigation of the dynamics of such periodic states led to the discovery of other solutions which are neither steady nor periodic. Such solutions are described as chaotic.

Fewer investigations have considered the related problem where the convection is driven by internal heat sources. Real systems which are modelled by internally heated porous media include flow around nuclear reactor cores, soil contaminated with nuclear debris, and packed bed reactors.

1.2 Motivation

Many investigations have considered the idealized problem of an infinite porous layer with bottom heating and top cooling. In the present study, a finite porous medium of square cross section bounded by an impermeable, isothermal periphery will be subjected to natural convective flow driven by internal heat sources. A bifurcation structure of the stationary solutions in such a system has been completed previously [3]. The initial phase of this dissertation considers the effect of tilting the medium on these solutions. This study reveals regions of the parameter space where interesting dynamical behaviour can be expected.

The analogy between flow in fluid and porous layers has been considered for bottom heated layers. In order to extend the realm of this analogy to internally heated layers, a bifurcation study comparable to that done for the porous layer is required. However, no investigations were found where convection in a vertical Hele-Shaw cell was driven by internal heating. Therefore, a model was developed to simulate the flow of fluid inside a finite geometry Hele-Shaw cell with an impermeable, isothermal periphery where convection is driven by internal heat sources. The steady-state bifurcation structure of this domain has been computed. Thus, a comparison of the two different models is possible to determine the applicability of the fluid layer as a substitute for a porous layer in terms of bifurcation structure.

Since no other study has been done with a vertical Hele-Shaw cell whose convection is driven by internal heat sources, an experimental study of the this system and geometry is a necessity. Steady-state convective flows inside a Hele-Shaw cell have been observed through flow visualization with polystyrene beads.

Taken as a whole, this study considers the very important question of model discrimination. For a porous layer, several models are used to describe the flow within. These include the Darcy equation, which has been used here. Other models which are effective in modelling the flow within porous media were put forward by Forchheimer and Brinkman. To account for the heat flow, an energy equation is required. This dissertation uses the simple form of heat equation, where one equation models the heat flow through both phases and interphase heat transfer is neglected. Another idea is to write separate energy equations for each phase, and include a term within each equation that considers the heat transfer between the fluid and solid. These mathematical expressions simulate real flows with varying degrees of accuracy. The accuracy of the model can only be determined through comparison with data taken from a real flow which matches the conditions outlined in the model formulation. Flow velocities, heat transfer values, and flow transitions from stationary to periodic solutions are a few of the criteria that may be used to analyze the usefulness of a mathematical model.

In this study, two such comparisons are recorded. One comparison is the numerical model for the Hele-Shaw cell with an experimental system designed to match the mathematical model. Qualitative comparison of the flow patterns observed in the experimental apparatus are made with simulation results. These flow patterns will often be referred to as flow cells. A flow cell is defined as the path in which a packet of fluid travels around the test region. These paths tend to be ovular in shape.

The other comparison is that of a thin fluid layer with a porous slab. Comparison is based on the location of bifurcation points within the solutions of numerical models based on appropriate flow equations. Qualitative examination of the relative positions of stationary solution branches will add strength to the argument that a thin fluid layer can be used to learn about the behaviour within a porous layer.

1.3 Outline of Thesis

The remainder of this dissertation contains the results of the studies described above. In Chapter 2, reviews of the relevant investigations that deal with convection in fluid and porous layers are presented. Consideration is given to bottom heated porous layers as well as internally heated ones. Literature works considering horizontal and vertical fluid layers heated from below are also outlined. These fluid layers may be considered to be thin enough to be Hele-Shaw cells, or of larger dimension. Internally heated fluid layers where the fluid lies in the plane of a table-top have also been studied, and these findings are included here.

In Chapter 3, the mathematical model for natural convective heat transfer within a thin porous slab driven by internal heat sources is developed. A two-dimensional form of the Darcy-Oberbeck-Boussinesq model results, and it is solved for steady state solutions and the origin of oscillatory solutions. Special emphasis is placed on the rearrangement of bifurcation structure as the slab is tilted from horizontal to one degree. The computer code for this study was developed by Weinitschke *et al* [3] and needed only minor modifications to account for variation of the tilt angle.

In Chapter 4, a model for convection in the internally heated Hele-Shaw cell of finite dimension is developed. The Navier-Stokes equation is the starting point in the development of the equations. The thin gap approximation has also been incorporated, as was done by Buhler *et al* [4]. Computation with the code developed for this model reveal the steady-state bifurcation structure and origins of oscillatory solutions. The effect of tilt is also examined for the Hele-Shaw cell.

An analysis of the similarities and differences in the two bifurcation structures is given in Chapter Five. The basis for comparison is:

- relative positions of bifurcation points and solution branches,
- the degree to which the porous layer solution can be seen to be a limiting case for the fluid layer structure, and
- similarity of flow patterns at comparable positions within the domain.

In Chapter 6, the experimental system and the observed flow patterns are discussed. A copper sulfate fluid layer within a square cross-section of length $3in$ and a gap width of $1/8in$ was contained by constant temperature copper walls on four sides and by plexiglas walls on the two large sides. Heating was provided electrolytically. Visualization with polystyrene beads revealed the flow patterns that existed within the test region. Comparisons with the numerical results center on the parameter values where a unique solution exists, and where a stable two cell flow ceases to exist.

In Chapter 7, the conclusions and recommendations from this study will be outlined. Suggestions for future work in this area will also be given.

Chapter 2

Literature Review

2.1 Fluid Layer

2.1.1 Layers Heated from Below

Modern studies of natural convection in fluid layers began with the work of Lord Rayleigh [5], who first formed the dimensionless grouping of the ratio of buoyant forces to viscous forces that now bears his name. It is the imbalance between these forces in a fluid within a gravitational field that cause convective currents.

Initial experimental work on convection in fluid layers heated from below was performed by Bénard [6]. When observed from above, the flows appeared to form hexagonal cells. Bénard believed the convection was driven by the bottom heating, but the flows were actually driven by surface tension as opposed to buoyancy forces. Nevertheless, convection in fluid layers heated from below is usually called Bénard convection.

Pellow and Southwell [7] neglected non-linear effects and determined that a particular size is associated with every shape of cell. In an infinite layer no cell mode was as likely to occur as any other. They speculated that the appearance of hexagonal cells was due to these neglected non-linear effects.

A finite amplitude study by Malkus and Veronis [8] found an infinite number of steady-state solutions. Relative stability was determined by ranking the solutions using the criterion of maximum mean-square temperature gradient. The convection is due to a distortion by the temperature field, and the observed self-distortion of the disturbance is of secondary importance. They also determined that square horizontal cells were preferred to hexagons in ordinary fluids with symmetric boundary conditions.

Palm [9] found that the temperature dependence of viscosity resulted in a second order term which led to the development of the hexagonal motion. For a fluid whose viscosity decreases with increasing temperature, the hexagons with flow upward through the center were stable. Fluids with viscosities that increase with increasing temperature form stable flows with downward flow through the center of the hexagon.

Segal and Stuart [10] modified Palm's result to say that hexagons may be the stable equilibrium state if the temperature variation of viscosity is large enough. A two-dimensional roll is also a possible equilibrium state under the same conditions. The observed mode is determined by the initial conditions, but most physical systems would lead to the production of hexagons.

Following the work of Malkus and Veronis, Schlüter *et al* [11] showed that not every linear solution approximated a non-linear solution, but there were an infinite number of finite amplitude solutions. Their stability theory claims three-dimensional convection flows are unstable to infinitesimal disturbances. Some two-dimensional rolls are stable depending on the wavenumber of the roll. The asymmetry due to temperature dependent parameters results in the stability of hexagons between the critical Rayleigh number and a certain supercritical value, beyond which the two-dimensional rolls are stable.

Krishnamurti considered the transition to turbulent flow in an infinite horizontal fluid layer heated from below. Her experiments were performed on a fluid layer which varied in depth from $2 - 5cm$. The first transition is the onset of convection, which occurs at R_c. The second transition [12] occurs at $12R_c$ and the flow moves from steady two-dimensional rolls to a steady periodic three-dimensional cellular pattern. There is hysteresis in this transition, which indicates it is caused by finite amplitude instability. Time dependent flows [13] occur in two modes. One mode can be seen as a tilting of the boundary of a flow cell. This tilting occurs at a time scale similar to the thermal diffusion time. The second mode of oscillatory flows showed the advection of a hot spot within the cellular motion. Measurement of temperature at a fixed point showed the oscillations of the hot spot. Increasing the frequency and number of these oscillations led to turbulence.

The study of Rayleigh-Bénard convection and the onset of turbulence in an infinite layer continues to be of interest to this day [14].

An excellent treatment of other topics concerning fluid layers heated from below, is given in the book by Chandrasekhar [15]. Fluid layers concurrently subjected to rotation and magnetic fields are also dealt with.

2.1.2 Layers with Internal Heat Sources

A phenomenon related to Bénard convection is natural convection within a fluid layer which is driven by internal heat sources. In these investigations, the depth of the fluid layer was significant compared with the lengths in the other two dimensions.

Qualitative experiments by Tritton and Zarraga [16] on a system heated internally and cooled from above showed similarity to Bénard convection. The main difference was that the fluid descended in the centre of the cells and ascended on the edges in the internally heated layer. At low Rayleigh numbers, the horizontal extent of the convection pattern was comparable to the fluid depth. For convection at higher Rayleigh numbers, the flow pattern had a horizontal extent of up to five times the fluid depth. This flow pattern appeared to change toward rolls as the Rayleigh number increased.

A theoretical paper by Roberts [17] studied the same system as Tritton and Zarraga [16]. A Fourier analysis of dominant terms showed that that three different flow structures were possible. These were rolls, hexagons with upward flow through the centres, and hexagons with downward flow through the centres. Only the downward flow hexagons were found to be stable, and this was only true as long as the Rayleigh number exceeded a critical value dependent on Prandtl number. For water, this critical Rayleigh number is approximately 8750. In between this value and a Rayleigh number of 2772, which is the critical value for the onset of convection, only the rolls were possible. However, these rolls were marginally stable. Also, the neutrally stable wavelength of the rolls decreased slightly with increasing Rayleigh number. All of these facts put the study of Roberts into conflict with the finding of Tritton and Zarraga.

Thirlby [18] numerically solved the full partial differential equations governing the stability of the convective motion in the internally heated layer. He suggested that the experiments of Tritton and Zarraga [16] found only hexagons due to large viscosity variations. Thirlby also confirmed most of the ideas presented by Roberts [17]. Schwiderski and Schwab [19] modified the apparatus of Tritton and Zarraga in an attempt to explain this discrepancy. They found that the non-uniform internal heating and poor electrical insulation of the cooling plate caused errors in the earlier experimental results. Their results were in agreement with the results of both Roberts and Tritton and Zarraga.

Kulacki and Goldstein [20] considered a fluid layer cooled above and below by isothermal plates at the same temperature. They considered the heat transfer at Rayleigh numbers up to 675 times the critical value from linear stability theory. The amount of energy transport at the upper boundary was more than twice that at the lower boundary.

Kulacki and Nagle [21] used a fluid layer cooled only from above to determine a correlation between Nusselt number and Rayleigh number over the range $114 \leq Ra/Ra_c \leq 1.8 * 10^6$, where $Ra_c = 1386$.

A numerical study of Tveiteried and Palm [22] showed that hexagons are stable up to $15R_c$, and that hexagons are formed even if the initial motion is different. For higher values of Prandtl number the hexagons have downflow through their centres, but if $Pr < 0.25$, hexagons with upward motion through their centre are stable.

Turbulent flow in a volumetrically heated fluid layer is also an area of active research [23], as are layers heated internally and below simultaneously [24, 25, 26].

2.1.3 Hele-Shaw Cells

A variation of the theme of convection in fluid layers involves studying very thin fluid layers. In 1898, Hele Shaw [27] showed the similarity between the isothermal flows between closely spaced parallel plates and in porous media. It wasn't until 1960 that Wooding [28] looked at the stability of a fluid at rest between two long vertical parallel plates under a vertical density gradient, and suggested that this may be an easier manner to study convection in porous layers.

Several authors have attempted to determine the limits on the use of Hele-Shaw cells for porous layer modeling. Hartline and Lister [29] suggested that the permeability of a Hele-Shaw cell be $d^3/12Y$ instead of the accepted $d^2/12$, where d is the spacing between the plates and Y is the width of the gap plus the containing walls. The maximum wall thickness allowed was $0.65cm$. The inclusion of the side walls into the permeability was to account for the heat loss through the side walls in non-isothermal flows.

Kvernvold [30] looked at the difference in the stability regions for non-linear convection, and found that Hele-Shaw convection is stable for a wider range of wave numbers and Rayleigh numbers. This was due to the existence of disturbances of arbitrary orientation in a porous layer, while the Hele-Shaw cell geometry limits disturbances to two dimensions with the axis parallel to the axis of the stationary roll.

Frick and Clever [31] considered the effect of side walls on the convection in fluid layers of arbitrary width. The presence of side walls led to three-dimensional flow patterns. The resulting change in wave number and three-dimensional effects of porous media convection cause strong deviation from Hele-Shaw flow for infinite aspect ratio. For finite aspect ratio, the Hele-Shaw approximation becomes less accurate as the convection amplitude increases. This leads to large differences for Rayleigh numbers greater than a few times the critical Rayleigh number, even though the analogy is almost perfect at the onset of convection.

The experimental investigation of Koster and Müller [1] used holographic interferometry to determine the effect of aspect ratio and thermal properties of the cell and fluid on the critical Rayleigh number. They also calculated bounds for stability of two-dimensional rolls. Oscillatory convection for high supercritical Rayleigh numbers was also seen, and it was determined that it was caused by instability of the thermal boundary layers at the horizontal walls. The period of these oscillations decreased with increasing Rayleigh number. Continuation of the study of these oscillatory solutions [2] resulted in the discovery of periodic, quasiperiodic and non-periodic structures. There were regions of non-periodic flows followed by quasiperiodic or periodic oscillations. Further study [32] showed that at certain Rayleigh numbers there were three regions: the centre with steady flow and the two end regions exhibiting different nonperiodic flows. However, no chaos was discovered, as higher transitions resulted in steady flows.

Recent works with Hele-Shaw cells have continued to look at thin gaps as a tool to aid in the study of behavior in porous media. These studies have considered topics such as two phase displacement [33], movement of bubbles [34, 35] and viscous fingering [36, 37, 38], which have direct application in enhanced oil recovery. Others have looked at the flow in these cells for its own sake, considering free boundaries [39] and non-Boussinesq effects [40].

2.2 Porous Layer

2.2.1 Heated from Below

The original research in convection within porous layers considered the criteria for the onset of convection in a porous layer saturated with a motionless fluid. A two-dimensional linear stability analysis showed that marginal stability was first reached when the filtration Rayleigh number attained a value of $4\pi^2$. Horton and Rogers [41] showed that this result applied to an infinitely long porous medium with free surfaces above and below and perfectly conducting media adjacent to the boundaries. Lapwood [42] found this criterion also applied to porous media bounded by infinitely long isothermal plates at different temperatures. This study led to so much further research that convection in porous layers heated from below is referred to as Lapwood convection.

Original studies of porous media convection used the thermal conductivity of the saturating fluid in evaluating the Rayleigh number. However, errors between experimental and theoretical values of the critical Rayleigh number were found. This discrepancy was resolved by Katto and Masuoka [43], who determined that the effective thermal conductivity for the porous layer must be used to obtain correct results.

In studies of Lapwood convection, authors have considered many possible variations. Some studies have looked at the effects of aspect ratio and other geometric effects in finite rectangular media [44, 45]. In order to remove the problems of the corners in a rectangular medium, cylindrical [46] or annular [47, 48, 49] geometries have been chosen. Different boundary conditions have also been considered, including constant flux boundaries [50, 51, 52] and systems heated from above and cooled from below [53].

The majority of work has considered flow in the Darcy regime, which neglects the effects of the boundaries and fluid inertia. Some effort has been directed at determining these effects by using the Forchheimer model [54, 55] or the Brinkman model [56, 57, 58] as a momentum equation.

Another set of investigations have considered non-uniform media [59] or media with embedded obstructions [60, 61, 62]. The evolution of stable convection into oscillatory convection [63] and chaos [64], as well as the mechanisms that begin this destabilization [65, 66], have been studied.

The study of convective structures in Lapwood convection within horizontal layers has received much attention. In 1972, Bories, Combarnous and Jaffrennou

[67] reported the transitions between the different types of convective motions in porous media. These states were adjacent polyhedral cells, unicellular flow, a system of stable coils and a fluctuating convective state characterized by the continuous creation and disappearance of convective cells. This fluctuating state was observed by Caltagirone, Cloupeau and Combarnous [68] in 1971, while the other states were experimentally observed by Bories and Combarnous [69] in 1973. An extensive review of developments in convective behaviors in bottom heated porous layers up to 1975 is given by Combarnous and Bories [70].

Vertical porous layers have been considered to a lesser extent. Some research has looked at layers at various tilt angles from horizontal to vertical [69], while other work has considered only vertical media [71, 72]. Only a unicellular flow has been found to exist in vertical porous layers.

There has also been some study of natural convection in inclined porous media. An initial investigation by Combarnous [73] found that a porous layer with a small slope bounded by isothermal plates exhibited a stable laminar convection state when $40 \leq Ra\cos\phi \leq 240 - 280$.

A mathematical treatment performed by Holst and Aziz [74] found that the maximum rate of heat transfer occurred at an angle of 40° from the vertical. Large velocity gradients were found near the system boundaries at low angles, and large effects were seen near the boundaries at increased angles. A concurrent experimental study indicated that multiplicity was possible in tilted porous layers and that the observed mode of convection depended on how the boundary conditions were established. Another study of Holst and Aziz [75] showed that three dimensional natural convection provides significantly more heat transfer than does two-dimensional motion.

In 1985, Caltagirone and Bories [45] published an extensive study that attempted to theoretically predict experimentally observed structures. The presence of finite dimensions was found to have a stabilizing effect when the layer was tilted. This meant the accepted stability criterion for an infinite layer, $Ra \cos \phi = 4\pi^2$, was not valid in the case of a finite layer. An earlier paper by Walch and Dulieu [76] discussed the existence of a reverse unicellular flow for angles less than 7°. This idea was extended to find three solutions. One of these was a positive unicellular flow, while the other two corresponded to reverse flows. A positive flow was defined to be an upward current along the hot boundary with a downward current along the cold boundary. Increasing the tilt angle shifted the point of transition for appearance of these reverse flows to higher Rayleigh numbers. For tilt angles greater than 6°, these reverse flows could no longer exist.

The experimental study of Kaneko et al [77] used the apparatus of Holst and Aziz and showed that the value of critical Rayleigh number for the onset of convection varied for different solids and fluids. This work confirmed an earlier statement of Combarnous [73]. The assumption of infinite heat transfer between solid and fluid is invalid, but is implicit when a model with only one energy equation is used. One energy equation models are commonly used for simplicity, but are only accurate when the thermal conductivity of both phases is of the same order of magnitude, and both phases are at the same temperature.

Other authors considered models which account for different thermal properties in the two phases and the possibility of heat transfer between fluid and solid. Combarnous and Bories [78] assumed that a porous layer is two continua, and wrote separate energy equations for each phase. These two energy equations are linked through a term which accounts for heat transfer between phases. The effect of different heat transfer coefficients and thermal conductivity ratios of the two phases on the overall heat transfer was shown. Chan and Banerjee [79] used a model with two energy equations as well, but solved for conduction in the solid phase as well as interphase heat transfer. Computations with this model were in close agreement with experimental data.

2.2.2 Internally Heated Porous Layers

Another set of researchers have focused on porous media systems with natural convective flow due to the presence of internal heat generation. Gasser and Kazimi [80] performed a linear stability analysis on such a system with a free upper surface and rigid lower surface to determine the value of the dynamic parameter at the onset of convection.

Analytical and experimental work by Buretta and Berman [81] considered a system with a rigid isothermal upper surface and a rigid adiabatic lower surface. They showed that the critical Rayleigh number for systems with internal heat sources was 31.8, as compared to $4\pi^2$ for natural convection due to heating from below. A discontinuity in the heat transfer curve was discovered. They postulated that this discontinuity was due to the existence of a bifurcation point at the critical Rayleigh number.

Tveitereid [82] performed a stability analysis and determined that two dimensional rolls and polyhedral cells were possible steady-state solutions. Only the rolls and polyhedral cells which flowed downward through the center were stable.

Other authors have considered a system with a fluid layer above a saturated porous layer, either heated from below [83] or internally [84, 85].

A three-dimensional case of internal heating was looked at by Beukema, Bruin and Schenk [86]. They attempted to simulate the cooling of agricultural products in cold storage and determine how convection aids in this cooling.

2.2.3 Other Studies of Porous Convection

Combined natural and forced convection has been studied by very few authors. Most of these works considered the effect of through flows on natural convection as opposed to the results of the interactions between the two phenomena. An analytical and numerical study by Haajizadeh and Tien [87] showed that the Nusselt number depends on the aspect ratio, Rayleigh number and Peclet number. Even a very small forced flow affects the temperature profile, while large flows suppress the effects of natural convection.

It has also been shown that the mathematical models of mixed convection and natural convection with internal heat generation are similar under certain conditions. Islam and Nandakumar [88] showed this to be true if axial conduction is negligible, a thermally developed state exists in the axial direction, and the Darcy equation is obeyed. This model exhibits dual solutions over a limited range of flow parameter. A subsequent study of this model [89] considered the transient evolution to stationary solutions as well as the development of sustained oscillatory solutions.

2.3 Bifurcation Studies

Bifurcation studies are often used to characterize the changes in steady-state behavior as parameters are varied. There have been recent bifurcation studies on systems such as mixed convection in horizontal rectangular ducts [90], laminar flow in rectangular curved tubes [91] and flow between concentric rotating cylinders [92].

Cliffe and Winters [93] looked at the cusp catastrophe for Bénard convection in a tilted rectangular cavity of unit aspect ratio. The state diagram for a slightly tilted cavity contained a limit point. Tracking this limit point as the tilt increased showed that it ceased to exist if the layer was incline more than 22° above or below the horizontal.

Many of the bifurcation studies considering porous medium convection have been undertaken by Riley and Winters. They used bifurcation theory to study two-dimensional Lapwood convection. Their purpose was to determine the effects of aspect ratio and tilt, and the existence of multiple solutions [94, 95]. A complete bifurcation structure for the stationary solutions has been generated. The preferred modes of convection were determined along with the exchanges in mode as these parameters were varied.

In order to perform any bifurcation study on a mathematical model, it is essential to determine the symmetries within the system geometry. For a rectangular, horizontal porous layer heated from below, there are two types of symmetries present. One is reflective symmetry about the mid-line axes of the layer, while the other is symmetry about the center point of the domain, known as centro-symmetry. The reflective symmetry about the horizontal axis and the centro-symmetry are due to the linear temperature gradient that exists in a stagnant layer which is bottom-heated and cooled at the top. This situation maintains itself as long as the thermal driving force remains below the critical value to initiate convection. When the mathematical model is made non-dimensional, the dimensionless temperature is scaled so that the difference between the temperature at the given point and the temperature at the mid-line is important. The result is symmetry about the horizontal and vertical centerlines, as well as the center point of the domain. In combination, this symmetry is referred to as $\mathbf{Z_2 X Z_2}$ symmetry. Tilting of the layer provides an asymmetric perturbation which breaks both reflective symmetries, but not the centro-symmetry. For a complete discussion of the symmetries in Lapwood convection, refer to Riley and Winters [95].

A bifurcation study of the model in [88] was performed by Weinitschke *et al* [3] to determine the structure of the heat transfer phenomena in an untilted, vertical porous slab. This model can describe both mixed convection heat transfer and natural convection with internal heat sources if certain conditions are met.

The symmetries present in the layer with internal heat sources are not as abundant. For an untilted layer, there is only reflective symmetry along the vertical centreline of the domain. With internal heating driving the convection, the fluid can only be stagnant if there is no heating. Due to the cooling on all sides, a stagnant layer in this situation is at the same temperature as the side walls. When internal heating begins, convective flow initiates within this system. There is no state within the system, other than its trivial state, where there is a symmetry about the horizontal centreline of the domain. Similarly, there cannot be symmetry about the center point. Upon tilting the layer, the reflective symmetry about the vertical centreline also disappears.

In this dissertation, only the porous layer with internal heat sources is considered. The model from [3] has been modified to include the effects of tilting the porous slab. The changes in the solution structure due to the effects of the asymmetric perturbation of tilt will be the main consideration.

Chapter 3

Porous Layer Simulations

3.1 System Description

The system under study is a rectangular, two-dimensional porous slab of length 2b and height 2a. The cell is filled with a homogeneous, isotropic porous material with permeability K, and is saturated with a single phase fluid of density ρ_f, heat capacity C_p and viscosity μ. Interphase heat transfer resistance is neglected, requiring the two phases to be in thermal equilibrium. Bounding the porous slab are impermeable surfaces held at a uniform constant temperature T_w'. The entire geometry can be tilted at an angle ϕ above the horizontal. Within the porous layer there is a uniform internal heat generation per unit volume Q_g. This internal heating provides the horizontal temperature gradient in the gravity field that can generate a natural convective flow within the slab. A sketch of the geometry in this model porous system is shown in Figure 3.1.

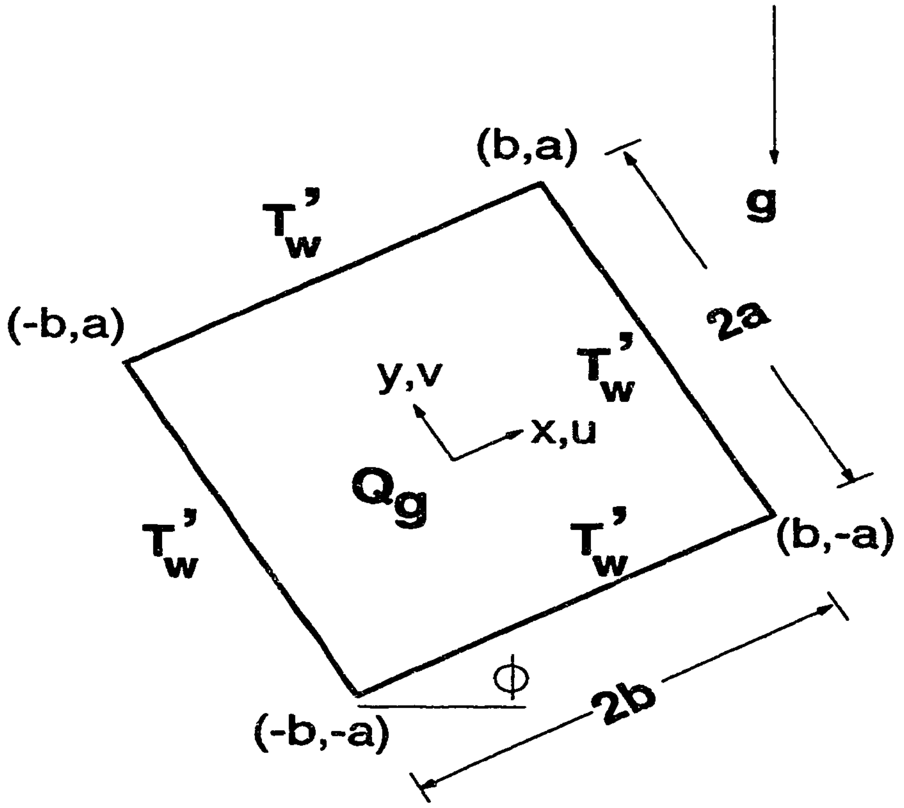

Figure 3.1: Geometry of the Porous Layer System

3.2 Mathematical Description

The following model was originally derived by Weinitschke et al [3]. All equations have been volume averaged so that macroscopic quantities are utilized. The two-dimensional form of the continuity equation is:

$$\frac{D\rho}{Dt'} + \rho[\nabla' \cdot \mathbf{v}'] = 0 \tag{3.1}$$

For the flow equation, the Darcy equation is used due to its simplicity. It also sets an upper limit on the flows which may be studied. Its form is:

$$\mathbf{v}' = -\frac{K}{\mu}[\nabla' p' + \rho \mathbf{g}] \tag{3.2}$$

Since there is no resistance to interphase heat transfer, only one energy equation is needed. It is of the form:

$$\sigma \left[\frac{\partial T'}{\partial t'} + (\mathbf{v}' \cdot \nabla')\mathrm{T}' \right] = \alpha \Delta' T' + \frac{Q_g}{(\rho C_p)_f} \tag{3.3}$$

where, for the porous medium:

$$\alpha = k_{eff}/(\rho C_p)_f$$

The Boussinesq approximation is incorporated into the energy equation. It assumes all material properties are invariant over the temperature range of interest except for the buoyancy term which causes the convection. Within the buoyancy term, the density of the fluid is assumed to vary linearly with temperature according to:

$$\rho = \rho_o[1 - \beta(T' - T_o')]$$

The model equations are considered in a rectangular two-dimensional region

$$R' := \{(x', y') \mid -b \leq x' \leq b, -a \leq y' \leq a\}.$$

Cross-differentiating the two components of the Darcy equation eliminates the pressure term, and introducing the stream function

$$u' = \frac{\partial\psi'}{\partial y'} \qquad v' = -\frac{\partial\psi'}{\partial x'} \tag{3.4}$$

satisfies the continuity equation by definition. In order to make the equations dimensionless, the following scale factor are utilized.

$$\begin{array}{ll} x = \dfrac{x'}{b} & y = \dfrac{y'}{a} \\ u = \dfrac{u'}{(\alpha/a)} & v = \dfrac{v'}{(\alpha/b)} \\ \psi = \dfrac{\psi'}{\nu} & \theta = \dfrac{T'_w - T'}{(Q_g A'/k_{eff})} \\ A' = 4ab & \tau = \dfrac{t'}{(\sigma a^2/\nu)} \end{array}$$

Only steady state solutions are considered here, so all time dependent terms are neglected. The resulting mathematical model is:

$$\Delta_\gamma\theta - \gamma[\theta, \psi] + \gamma/4 = 0 \tag{3.5}$$

$$\Delta_\gamma\psi - Ra\gamma(\theta_x \cos\phi - \gamma\theta_y \sin\phi) = 0 \tag{3.6}$$

where:

$$\begin{array}{ll} Ra = \dfrac{Q_g K \beta A b}{k\nu\alpha} & \gamma = b/a \\ \Delta_\gamma = \dfrac{\partial^2}{\partial x^2} + \gamma^2\dfrac{\partial^2}{\partial y^2} & [\theta, \psi] = \theta_x\psi_y - \psi_x\theta_y \end{array}$$

The boundaries are impermeable and are maintained at a uniform peripheral temperature, and thus the boundary conditions are written as

$$\psi = 0 \qquad \theta = 0 \tag{3.7}$$

A rectangular duct with a horizontal orientation has reflective symmetry. This allows consideration of only half the domain, known as R^+, when determining the symmetric solutions of the bifurcation structure. In computational terms, this corresponds to

$$R^+ := \{(x, y) \mid 0 \leq x \leq 1, -1 \leq y \leq 1\}.$$

All asymmetric solutions must be located using a full domain, even in an untilted geometry. However, when the duct is tilted, the reflective symmetry is broken, which necessitates solution within the full domain:

$$R := \{(x, y) \mid -1 \leq x \leq 1, -1 \leq y \leq 1\}.$$

Solutions of slabs with negative tilt, which are those tilted below horizontal, can be constructed from solutions with positive tilt using the following symmetry properties:

$$u(x, y; \phi) = u(-x, y; -\phi) \qquad v(-x, y; \phi) = v(x, y; \phi)$$

$$\theta(-x, y; -\phi) = \theta(x, y; \phi) \qquad \psi(-x, y; \phi) = -\psi(x, y; \phi)$$

In the idealized case of infinite horizontal extent, the basic state is motionless, and only above a critical Rayleigh number does a convective motion begin through a supercritical bifurcation. In the case studied here, there is always a state of motion within the fluid for a non-zero Rayleigh number. The value of θ_x near the vertical boundary is always non-zero, so there is always a forcing term in Equation 3.6. Combining this with the symmetries in the domain and the geometry results in a basic state which has two counter rotating vortices. The bifurcations that occur in the solution correspond to the formation of additional vortices within the slab, and are due to instabilites of the solution branch.

Nusselt number is the parameter used to illustrate the behavior of this system for the majority of results presented here. The expression used to determine the

Nusselt number is unique to this specific geometry. The details for the derivation of this expression are shown in the paper by Ryland and Nandakumar [96]. Once a temperature field is computed for any instant of time, a spatially averaged Nusselt number is computed using the following expression:

$$< Nu >= \frac{\gamma}{1+\gamma^2}\frac{1}{< \theta_b >} \tag{3.8}$$

where the bulk mean temperature is

$$< \theta_b >= \int_R \theta dxdy \; / A.$$

3.3 Numerical Methods

The system of two coupled non-linear partial differential equations was solved using a Newton method at regular points along the path. The system may be written as one operator of the form

$$f(\mathbf{u}, \mathrm{Ra}, \gamma, \phi) = 0 \qquad \mathbf{u} = [\theta(\mathrm{x}, \mathrm{y}), \psi(\mathrm{x}, \mathrm{y})] \tag{3.9}$$

The linearized problem that is solved is

$$f_u(\mathbf{u}_n, Ra, \gamma, \phi)\mathbf{U}_n = \mathbf{r}_n \qquad U_n = [\mathrm{D_n}(\mathrm{x}, \mathrm{y}), \mathrm{P_n}(\mathrm{x}, \mathrm{y})] \tag{3.10}$$

The corrections D and P are obtained from the linearized form of Equations 3.5 and 3.6. These linearized Newton equations are

$$\Delta_\gamma D + \gamma[\psi, D] - \gamma[\theta, P] = r_1 \qquad r_1 = \tfrac{\gamma}{4} - \Delta_\gamma \theta_x - [\psi, \theta]$$

$$\Delta_\gamma P + Ra\gamma(D_x \cos\phi - \gamma D_y \sin\phi) = r_2 \qquad r_2 = -\Delta_\gamma \psi - \gamma Ra(\theta_x \cos\phi - \gamma\theta_y \sin\phi)$$

The system was discretized in the interior of R by central difference approximations with a uniform grid. Boundary conditions are of the Dirichlet type, so are easily imposed. The resulting sparse system of linear algebraic equations was solved using SPARSPAK [97], an efficient linear solver routine.

Initial guesses are required for the temperature and stream function values at the next value of Rayleigh number to be considered. These are determined using Euler-Newton continuation. A tangent vector to the solution path, $\dot{\mathbf{u}} = \frac{\partial \mathbf{u}}{\partial \mathbf{Ra}}$, is calculated from the expression

$$f_{\mathbf{u}}(\mathbf{u}, \mathrm{Ra}, \gamma, \phi)\dot{\mathbf{u}} = \frac{\partial \mathbf{f}}{\partial \mathbf{Ra}}$$

where

$$\frac{\partial f}{\partial Ra} = (0, -\gamma[\theta_x \cos\phi - \gamma\theta_y \sin\phi])$$

Only one back substitution of the right hand side is required following the last Newton step to produce the tangent.

Failure of the regular continuation scheme to converge is an indication that there is a singular point nearby. At a limit point, the operator f_u is singular. Accurate values of the parameter at bifurcation points are determined through the use of extended systems. In the case of a simple limit point, the extended system of equations shown by Moore and Spence [98] is utilized:

$$f(\mathbf{u}, \mathrm{Ra}, \gamma, \phi) = 0 \qquad f_{\mathbf{u}}(\mathbf{u}, \mathrm{Ra}, \gamma, \phi)\mathbf{v} = 0 \qquad m(\mathbf{v}) = 1 \tag{3.11}$$

where $\mathbf{v}$ is the right null eigenvector. The unknowns to be solved for are [**u**, **v**, Ra].

Within the extended system, the bordered scheme of Weinitschke [99] was implemented to minimize the number of situations where nearly singular matrices were required to be inverted. The extended system can be combined with regular continuation to track the locus of limit point positions with respect to parameters other than Rayleigh number.

Another observed behavior is a branch of asymmetric solutions emanating from a branch of symmetric solutions. The origin of the asymmetric branch is known as a symmetry-breaking point. Werner and Spence [100] showed that a symmetry-breaking bifurcation point of the pitchfork type is an isolated solution of the extended system of Equation 3.11, except that null vector **v** must be anti-symmetric with respect to the vector **u**. In this problem, the symmetry is expressed as:

$$\theta(x,y)=\theta(-x,y) \qquad \psi(x,y)=-\psi(-x,y) \tag{3.12}$$

Therefore, the anti-symmetry condition that **v** must satisfy is:

$$\theta(-x,y)=-\theta(x,y) \qquad \psi(-x,y)=\psi(x,y) \tag{3.13}$$

In addition, the calculation of symmetry-breaking points requires that the symmetry condition on $x=0$ be replaced with:

$$\theta_x(0,y)=\psi(0,y)=0 \qquad g(0,y)=h_x(0,y)=0 \tag{3.14}$$

A Hopf bifurcation is one where a branch of time-periodic solutions emanates from a steady solution branch. The point where the origin of periodic solutions occurs on the stationary branch is called a B-point. These points are characterized by the fact that the extended system for a limit point has an eigenvalue zero of multiplicity two while the null space of the extended system remains one-dimensional. This necessitates that the right and left null eigenvectors of the extended system (Ψ^{t_i},Φ^{t_i}) are orthogonal. The null eigenvectors (Ψ^{t_i},Φ^{t_i}) must be scaled so that they are nearly in the same direction as the eigenvectors of the previous point calculated. This is to say

$$\Psi^{t_{i-1}}\Psi^{t_i}>0 \qquad \Phi^{t_{i-1}}\Phi^{t_i}>0$$

This will allow the null vectors to rotate continuously as the fold curve is followed. Roose and de Dier [101] suggest that a monitor on the cosine of the angle between these null eigenvectors be implemented. If these vectors become orthogonal, the cosine of the angle between them is zero. Thus, the cosine of the angle between the two null eigenvectors will change sign as a B-point is passed.

Regular continuation fails when a simple limit point has been reached. To find solutions on the path beyond the limit point, the pseudo-arc length continuation scheme of Keller [102] is used. The equations are reparameterized with s, an arc-length parameter. An arc length constraint equation is also required. The equations are of the form:

$$f(\mathbf{u}(\mathrm{s}), \mathrm{Ra}(\mathrm{s}); \gamma, \phi) = 0 \qquad N(\mathbf{u}(s), Ra(s); \gamma, \phi) = 0 \tag{3.15}$$

At positions close to the limit point, it takes several iterations for the solution to converge. This is due to the sharp curvature of the solution path at the limit point, which results in poor initial guesses from extrapolation of the tangent vector. When the solution did not converge in a specified number of iterations, the step length was halved. This method was sufficient to turn around all limit points encountered here.

Grid sensitivity tests were performed to determine the minimum acceptable grid for the computations. The results of these tests are shown in Tables 3.1 and 3.2. The positions of the limit points changed little on refinement of the grid, while the solution structure was unchanged. The smallest changes were evident when the number of interior points in the grid was refined from 39 × 39 to 47 × 47 in each case. Therefore, all the remaining results presented are for a grid spacing of $h = 0.05$, which corresponds to a 39 × 39 grid of interior points for a porous slab of unit aspect ratio.

Grid Size	Ra=500	Ra=4000 low	Ra=4000 high
19x19	8.45682	13.0472	13.8712
29x29	8.47321	13.2517	14.1339
39x39	8.47890	13.3353	14.2216
47x47	8.48196	13.3788	14.2606

Table 3.1: Grid Sensitivity of Nusselt Number at Selected Rayleigh Numbers on Branch PM, $\phi = 1.0°, \gamma = 1.0$

Grid Size	L1	L3	L6
29x29	2606.20	4573.70	6526.93
39x39	2587.16	4506.78	6560.16
47x47	2578.47	4470.04	6492.32

Table 3.2: Grid Sensitivity of Rayleigh Numbers at Limit Points for the Porous Slab Simulations, $\phi = 0°, \gamma = 1.0$

3.4 Solutions Structure

3.4.1 Horizontal Orientation

As mentioned, the starting point for this study is the work presented in [3]. Figure 3.2 shows the overall bifurcation structure for a porous slab of unit aspect ratio and horizontal orientation. This solution was discussed thoroughly in [3]. A magnified view of the high Rayleigh number region is shown in Figure 3.3. The details of these figures are the same as in [3] except for the discovery of three new branches of asymmetric solutions. One branch is labelled AS4 and has a limit point AL13. There was no symmetric branch found that meets with this asymmetric branch at a symmetry breaking point. Winters [31] suggested that asymmetric branches may contain limit points. Such a situation has been located here. These

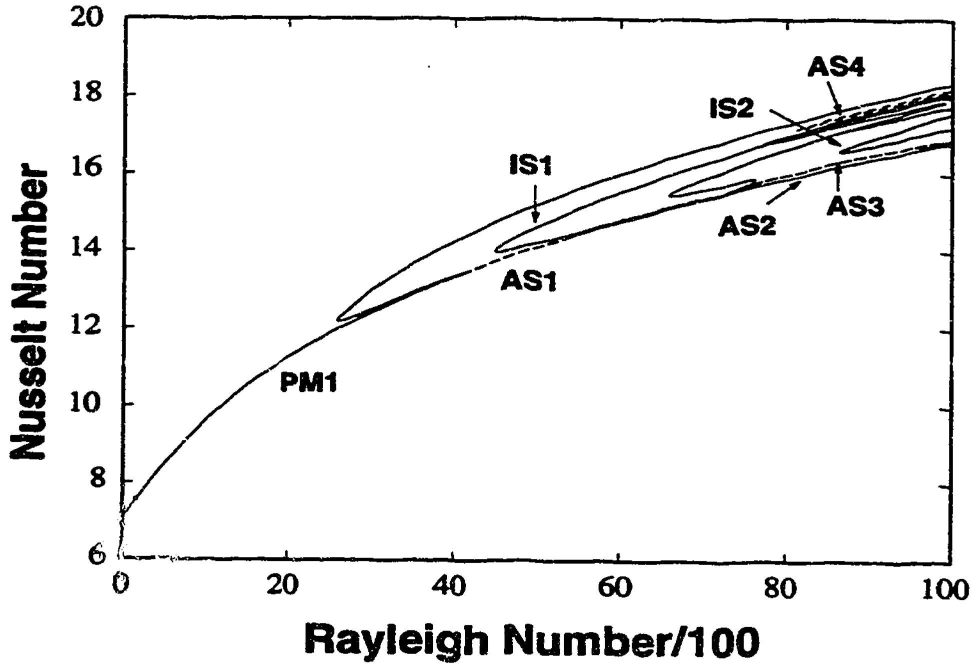

Figure 3.2: Bifurcation Diagram for a Horizontal Porous Slab, $\gamma = 1.0$. Solid lines represent symmetric solutions. Dashed lines represent asymmetric solutions.

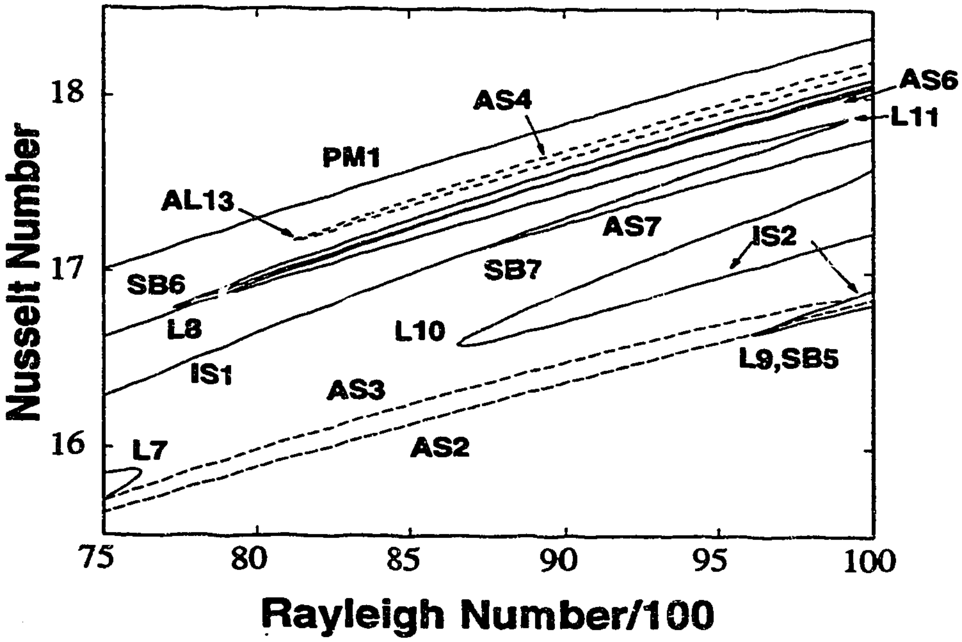

Figure 3.3: Bifurcation Diagram for a Horizontal Porous Slab: Detail of High Rayleigh Number Region, $\gamma = 1.0$

Point	Rayleigh Number
AL13	8117.86
SB6	7733.16
SB7	8693.76

Table 3.3: New Bifurcation Points Found, $\phi = 0°, \gamma = 1.0$

asymmetric branches usually occur in pairs, with the second branch having the same limit point and containing contours which are mirror images of the first branch. Extension of the ends of AS4 up to Rayleigh number values of 40000 showed no connection to any known symmetric solution branch.

Two other branches were discovered for the untilted solution structure. These were branches AS6 and AS7 that emanate from IS1 through symmetry-breaking points SB6 and SB7. As was the case with AS4, extension of these branches beyond the domain of interest did not lead to any new symmetric solutions. Branches AS6 and AS7 turn out to be very important when considering the transition of the solution structure as the slab is tilted from 0° to 1°. The positions of the bifurcation points on these newly discovered branches are given in Table 3.3.

3.4.2 Unfolding of the Solution upon Tilt

When the porous slab is tilted 1°, a very different solution structure emerges. It is illustrated in Figure 3.4, and the detail of the multiple solution branches in the high Rayleigh number region is shown in Figure 3.5. For the horizontal slab, the solution structure contains three symmetric branches with twelve limit points and six asymmetric branches for the range $0 \leq Ra \leq 10000$. A slab tilted only one degree above or below the horizontal has a structure which contains nine limit points on seven branches isolated form the origin, and an eighth branch from the

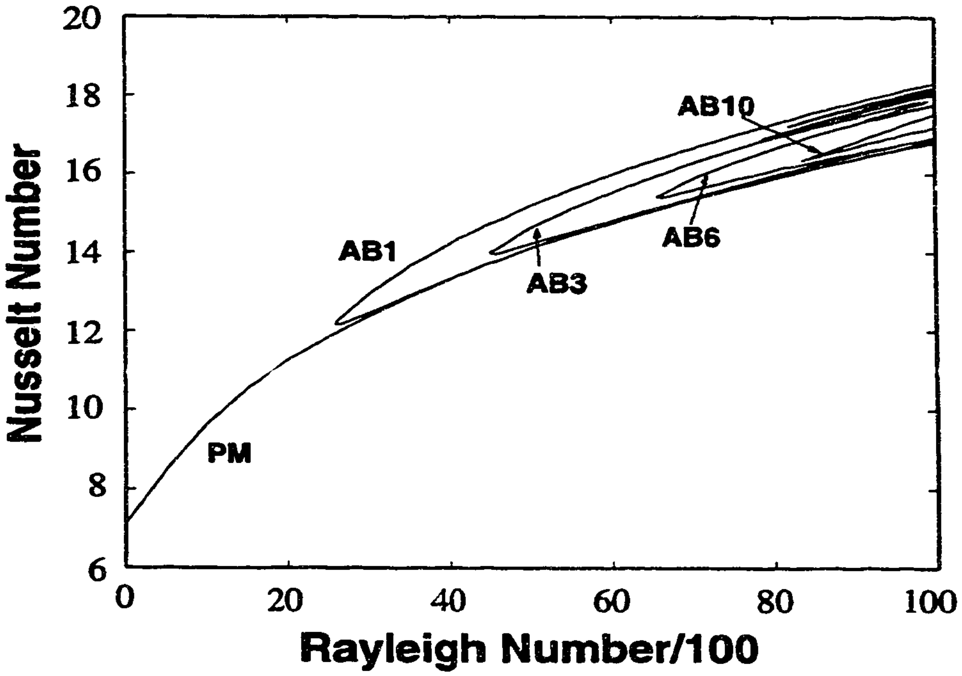

Figure 3.4: Bifurcation Diagram for a Tilted Porous Slab, $\phi = 1.0°, \gamma = 1.0$

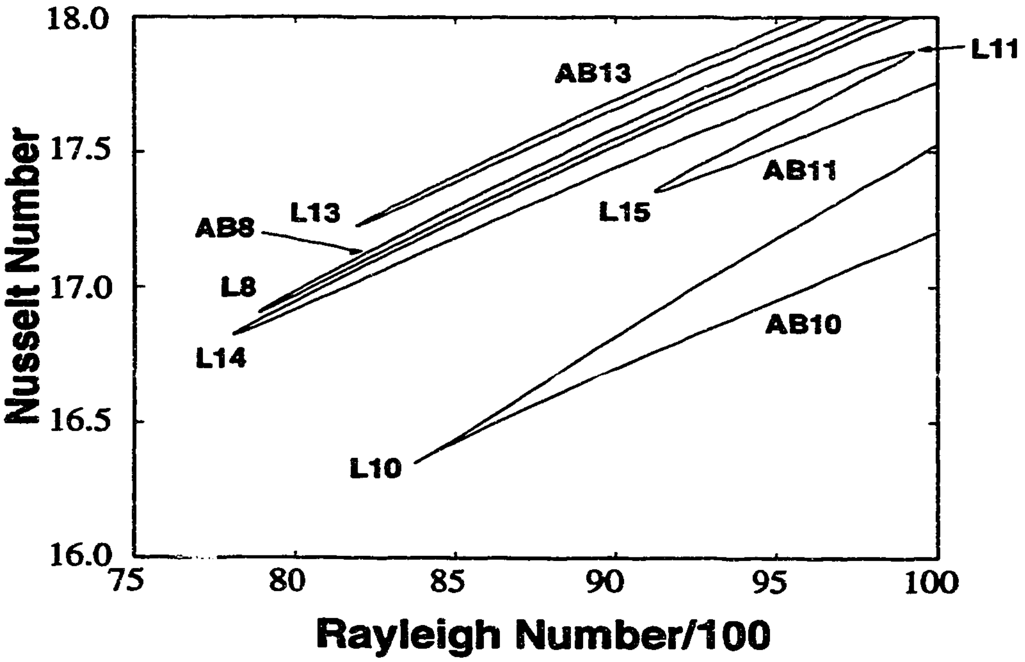

Figure 3.5: Bifurcation Diagram for a Tilted Porous Slab: Branches with Limit Points in the High Rayleigh Number Region. $\phi = 1.0°, \gamma = 1.0$

Limit Point	Rayleigh Number	Limit Point	Rayleigh Number
L1	2586.03	L7	7622.09
L2	4166.41	L8	7728.30
L3	4507.78	L9	9611.48
L4	5369.95	L10	8651.91
L5	5542.28	L11	9917.02
L6	6594.95	L13	8117.86

Table 3.4: Location of Limit Points in Horizontal Slab, $\gamma = 1.0$

origin which has no limit points. These limit points are labelled to correspond with those in the horizontal slab structure.

All isolated branches in the structure for the tilted slab open toward the right except for AB11, which has a section which opens to the left. Five of the six limit points that disappear upon tilt are located near symmetry-breaking points in the untilted structure. Only L11 does not follow this description, as no symmetry-breaking point has been detected near it in the horizontal solution structure. The isolated branch AB11 contains three limit points.

The exact positions of the limit points in the horizontal structure, as determined with an extended system, are given in Table 3.4. Limit points in the slab tilted one degree are shown in Table 3.5. In all cases, the Rayleigh number only changes a few percent.

3.5 Branch Rearrangement with Tilt

The rearrangement of connectivity of solution branches with tilting of the slab is interesting due to the resulting change in bifurcation structure. The graphs shown up

Limit Point	Rayleigh Number	Limit Point	Rayleigh Number
L1	2587.16	L10	8372.09
L3	4506.78	L11	9925.06
L6	6560.16	L13	8191.60
L8	7889.20	L14	7807.87
		L15	9124.72

Table 3.5: Location of Limit Points in Tilted Slab, $\phi = 1.0°, \gamma = 1.0$

to now are incapable of revealing the detailed structure. The asymmetric solution branches shown in previous figures appear as only one line. In fact, they are a pair of superposed branches, but this character is hidden by the use of averaged temperature in the determination of Nusselt number. When a state variable other than Nusselt number is chosen at a grid point away from the line of symmetry, the distinct character of these two branches becomes evident.

Stream function and dimensionless temperature are two quantities which have been selected to show the evolution of the solution structure as the slab is tilted. The value of these quantities are determined at a point with co-ordinates (0.1b, -0.9a) within the domain. In the previous investigation [3], this is a point where a secondary flow cell is located within the domain. Large differences in stream function and temperature occur there, depending on the presence or absence of a secondary flow cell.

The stream function representation of the bifurcation structure for an untilted slab is given in Figure 3.6. Note that asymmetric branches, such as AS1, which are straight lines when Nusselt number is the state variable, consist of two separate branches that connect SB1 and SB2. There are many branches in the high Rayleigh number region of the domain. The high Rayleigh number region is shown in

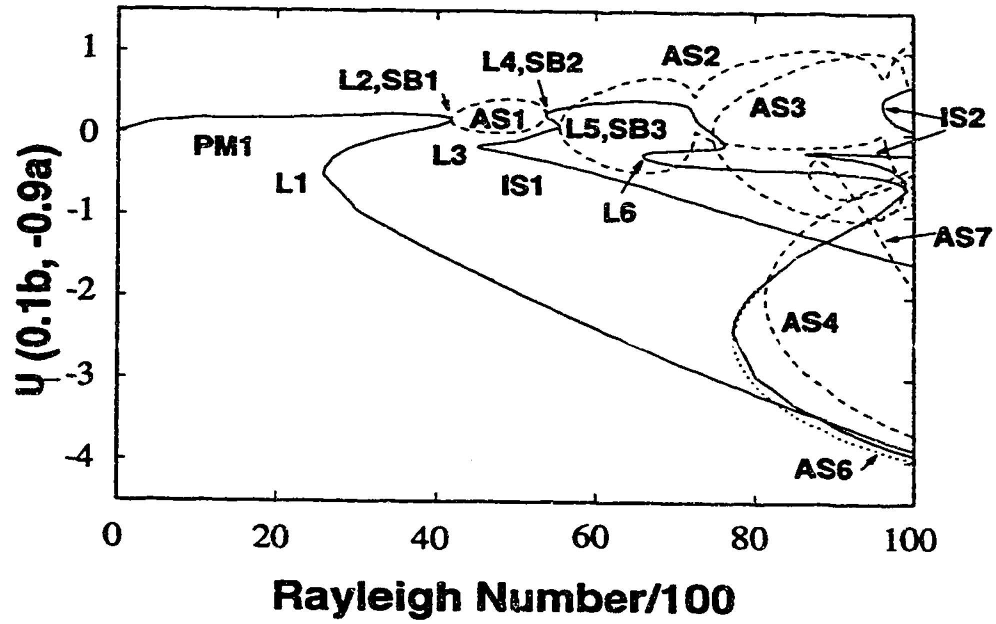

Figure 3.6: Solution Structure for an Untilted Porous Slab using Stream Function as the State Variable, $\gamma = 1.0$

Figure 3.7.

Another view of the solution is given by using dimensionless temperature as the state variable. The plots generated with this variable better illustrate the branch rearrangement with tilt. For an untilted slab, the solution is shown in Figure 3.8, while a layer tilted one degree above the horizontal is given in Figure 3.9.

Rearrangement of the solution structure is due to the following factors. As the layer is tilted, all symmetry is broken. Thus, symmetric solutions cannot exist. Symmetry breaking (SB) points are unstable to tilt, and they tend to coalesce with nearby limit points. Pitchfork bifurcations, of which a symmetry breaking point is one, unfold to eventually form a continuous branch and an isolated branch. Due to the multitude of SB points present in the untilted structure, a number of SB unfoldings occur. The ultimate result is a significantly different structure for a porous slab, even if tilted only one degree.

3.5.1 Tracing the Origins of Solution Branches

Each solution branch in the structure for the tilted slab consists of several sections of branches found in the untilted solution. The nature of the rearrangement can be understood by looking at the changes in solution structure in one region as the slab is tilted.

Consider the unfolding of SB1 into the limit point L2. An illustration of this unfolding is given in Figure 3.10. Since the SB point is structurally unstable to an asymmetric perturbation, it unfolds into a structurally stable singularity, which is a second limit point *L2'*. Upon further tilting, the two limit points *L*2 and *L2'* move closer together, and eventually coalesce as a double limit point. The double limit point dissappears as a hysteresis point.

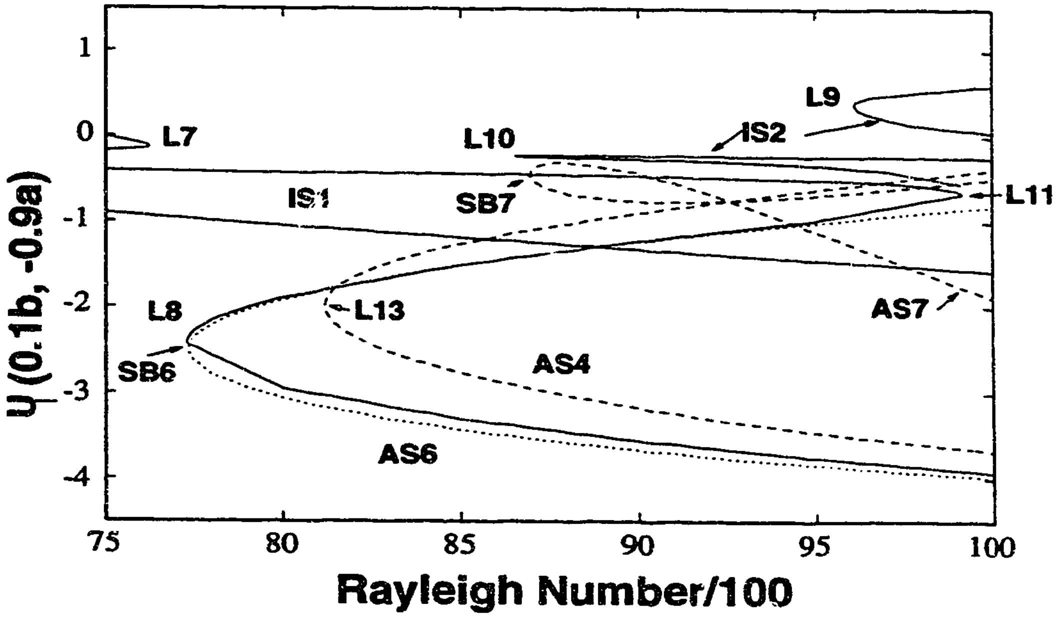

Figure 3.7: Solution Structure for an Untilted Porous Slab using Stream Function as the State Variable, $\gamma = 1.0$. Branches PM1, AS2 and AS3 have been removed for clarity.

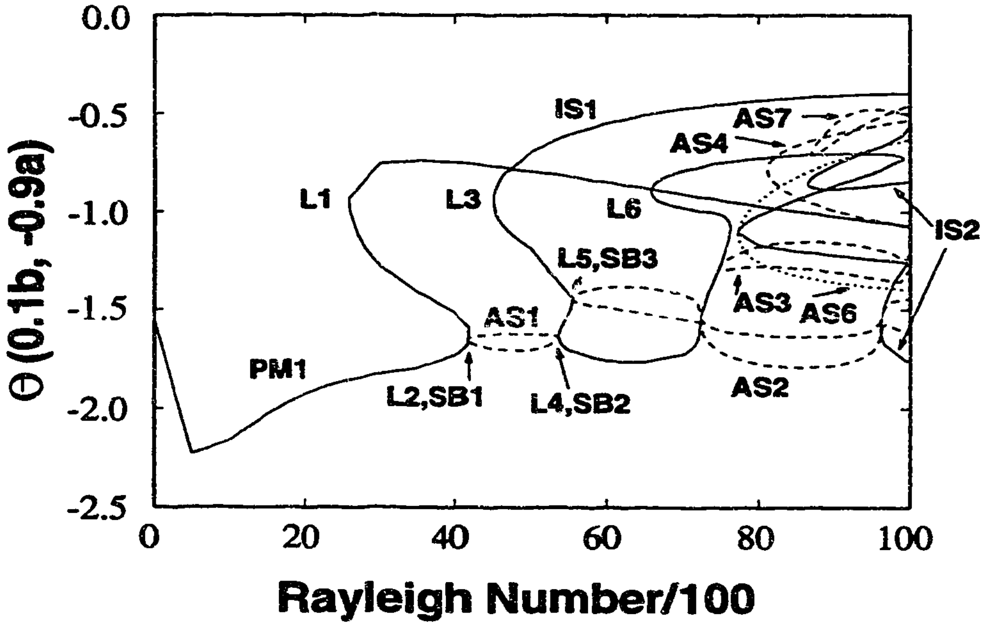

Figure 3.8: Overall Solution Structure using Dimensionless Temperature as State Variable, $\phi = 0°, \gamma = 1.0$

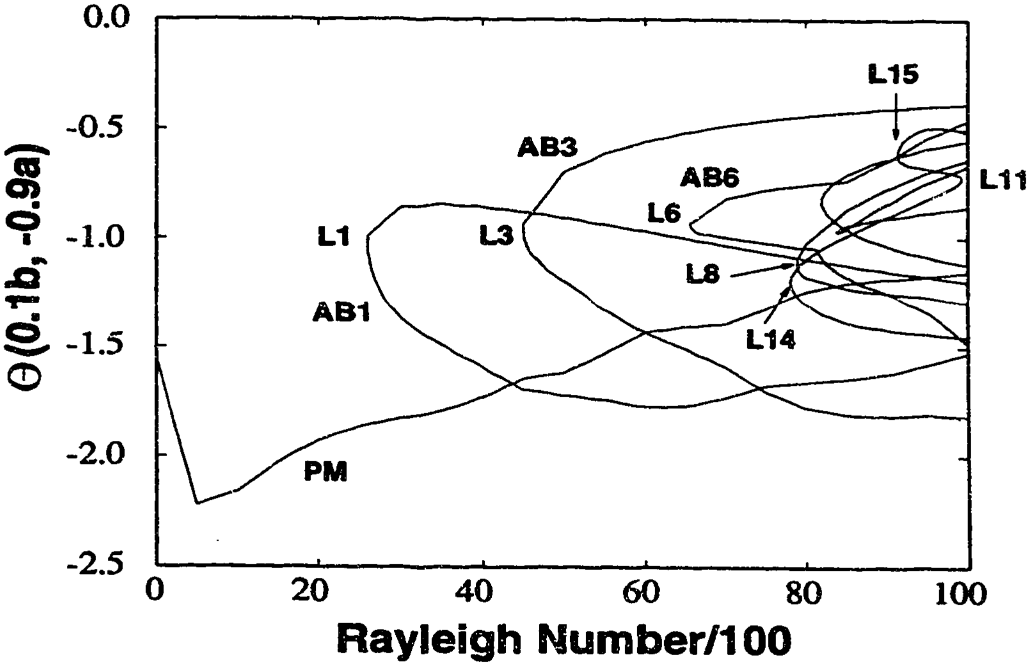

Figure 3.9: Overall Solution Structure using Dimensionless Temperature as state Variable, $\phi = 1°, \gamma = 1.0$

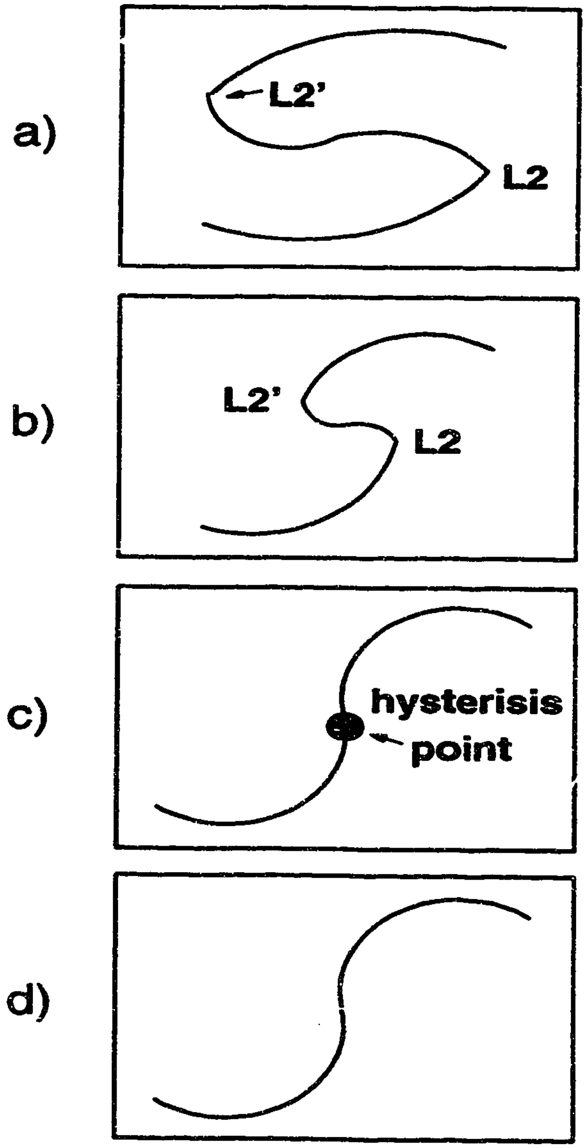

Figure 3.10: Unfolding of SB1 with Nusselt number as Illustrative Variable

In this case, unfolding of SB1 results in the lower section of primary branch PM1 joining with the upper branch of AS1, while the upper section of PM1 joins with the lower section of AS1. This particular rearrangement occurs due to the flow patterns which naturally occur in these branches. As shown in Figure 3.11, at positive tilt angles, the separation line is to the left of the slab centreline at the bottom of the slab for section *a* of the primary branch. A smooth rearrangement results if this branch joins with the asymmetric branch section where the separation line also is to the left of the slab centreline. In this case, that is the upper branch of AS1, labelled *d*. Similarly, the upper section of PM1, labelled *b*, may smoothly join with the lower branch of AS1, labelled *c*, as they have similar flow patterns.

If the slab is tilted below horizontal, which is the negative direction, the opposite rearrangement would occur. The section of PM1 coming from the origin would join with the lower branch of AS1, and the upper branch of AS1 would join with the section of PM1 coming from limit point L1.

This behaviour occurs in several places in the solution structure, as the large number of SB points present unfold. Ultimately, a very different solution structure is present for a tilted slab as compared to a horizontal slab.

As examples, the origin of branches PM and AB1 in the structure at $\phi = 1^\circ$ will be traced. The unique solution branch PM in Figure 3.9 has no limit point. Looking at Figure 3.8 and starting at the basic state ($Ra = 0$), the branch PM1 is followed to the point where limit point L2 and symmetry breaking point SB1 exist. The upper branch of AS1 is taken to the other end, where L4 and SB2 are. The upper branch is selected since PM and AB1 cross in the tilted structure. Following branch IS1 until the merger of L7 and SB4, the path follows the upper part of AS3 until the edge of the domain is reached.

To trace AB1, begin at the end of PM1 that exits the domain at $Ra = 10000$ in

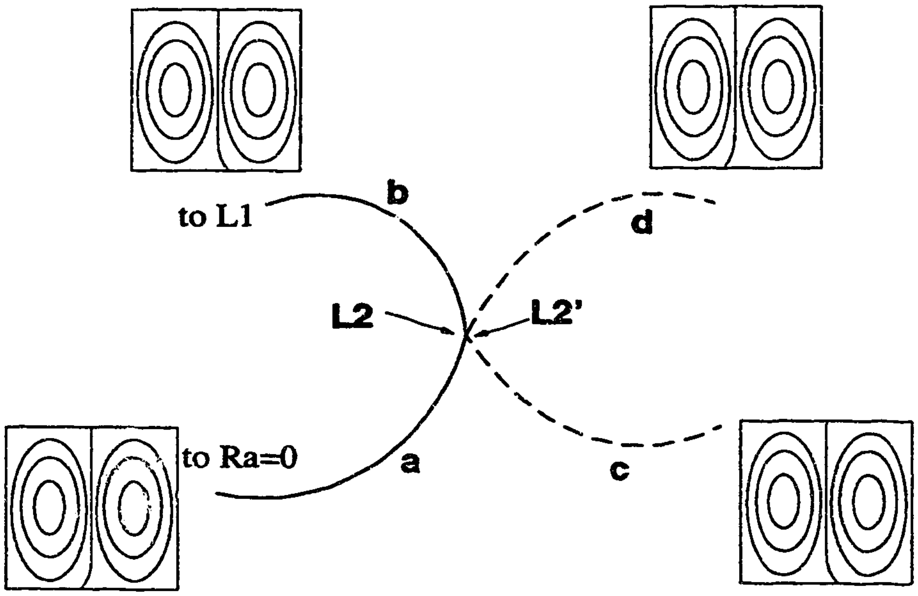

Figure 3.11: Unfolding of SB1 with Dimensionless Temperature as the Illustrative Variable. Flow Patterns for each Solution Branch appear beside the branch.

Figure 3.8. Follow PM1 back to the limit point L1 and down toward L2 and SB1. Follow the lower branch of AS1 to L4 and SB2. The section of IS1 from that leads to L7 and SB4 has been accounted for, so follow IS1 in the other direction to L5 and SB3. Since AB1 leaves the domain above AB3 in Figure 3.9, follow the upper branch of AS2 to $Ra = 10000$.

The remainder of the branches in Figure 3.9 can be traced in a similar manner from the structure of the untilted slab in Figure 3.8. Limit point L9 moved out of the domain of interest when tilting occurred. The section of IS2 which contained L9 was found to sensitive to the grid spacing. Thus, it was not accounted for in any of the results shown.

3.5.2 Merging of Limit and Symmetry-Breaking Points

The merging of limit and symmetry-breaking points is essential in the solution structure rearrangement described previously. This phenomenon also indicates the regions of parameter space where oscillatory solutions might be possible. Again, consider the unfolding of SB1 into L2. The fold curves in tilt for $L2$ and $L2'$ are shown in Figure 3.12. The limit points $L2$ and $L2'$ occupy the same position in the structure at a tilt angle of 0.0034.25g.

The fold curve of $L2'$ was found to contain an origin of a Hopf bifurcation, which is also known as a B-point. This point was determined at a tilt angle of 0.0028°, and is labelled on Figure 3.12. This type of behavior is referred to as a Takens-Bogdanov singularity [101]. A path of homoclinic bifurcations emanate from such a singularity. This behavior is important in the study of the dynamics of this system. However, the present work has been limited to the discovery of such points. Dynamic evolution of this system is outside of the scope of this thesis. However, such evolution has been considered in a companion paper by Ryland and Nandakumar [96].

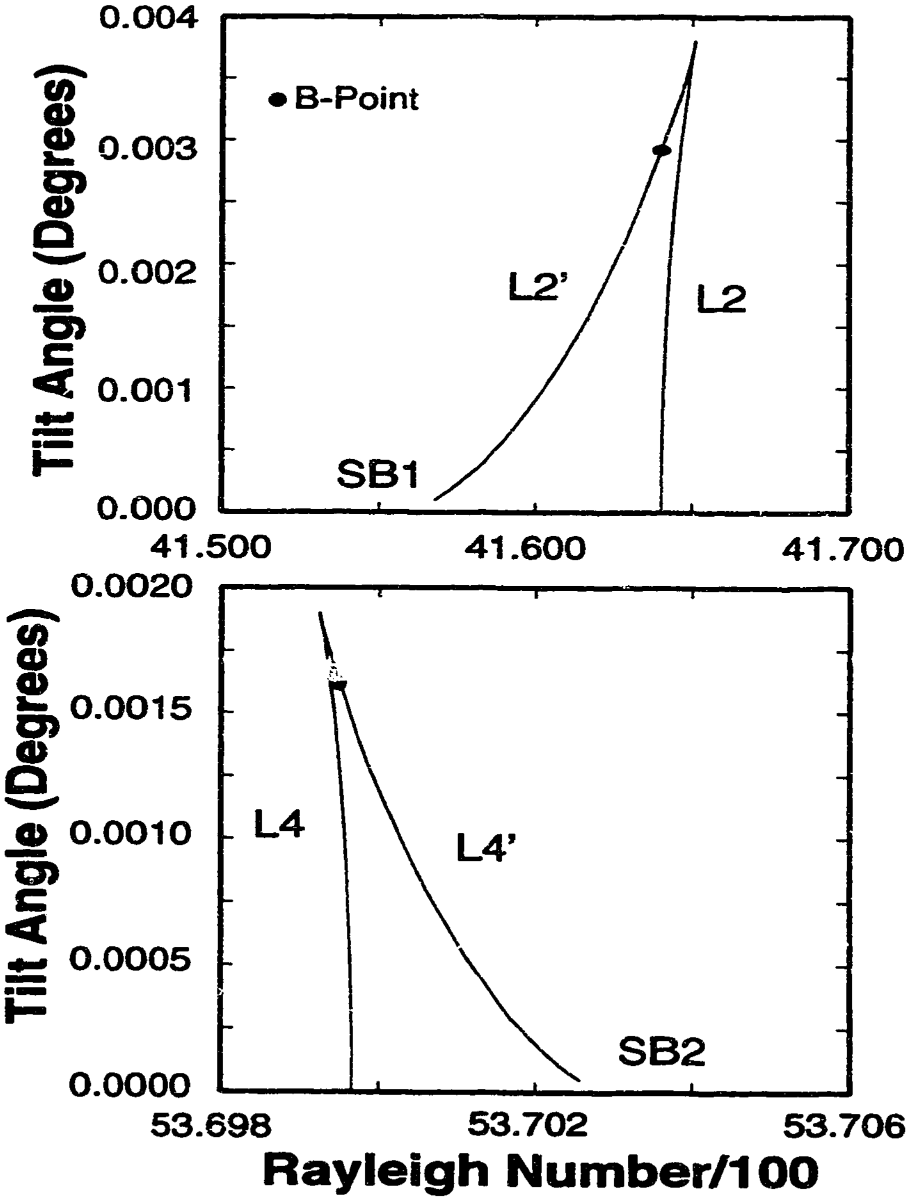

Figure 3.12: Unfolding of Symmetry-Breaking Points into a Limit Points on either end of AS1, $\gamma = 1.0$

At the other end of the asymmetric solution AS1, the symmetry-breaking point SB2 unfolds into limit point *L4′* and merges with limit point L4. The plot of this merging is also shown in Figure 3.12, and a B-point is also present of the fold curve of *L4′*. It has been speculated by Ryland and Nandakumar [96] that the path of oscillatory solutions originated on *L2′* actually ends on *L4′*, but this cannot be confirmed. This postulate is based on results from stability analysis. At a tilt angle of 1°, there is a change of stability along PM at a Rayleigh number of between 4400 and 4600. There is no apparent bifurcation point in the region that could cause such a change in stability. However, a path of oscillatory solutions passing the stationary solution branch could give this result. Another fact which supports this postulate is that the section of IS1 beyond L4 is stable in the untitled slab.

Other SB points unfold into limit points over equally small tilt angles. In a practical sense, it is impossible to observe these phenomena. The tilt angles involved are much smaller than the error in levelling any experimental apparatus.

There is another possibility for unfolding of a SB point with a limit point. The point SB6 has a limit point nearby, namely L8. The difference is that L8 opens away from the origin. No other limit point that opens to the right has a SB point in its vicinity, and still exists at a tilt angle of 1°. Figure 3.13 diagrams the structure before and after this interaction. At first, branches *e* and *f* are the symmetric solution with a limit point at *Lz*. Nearby are asymmetric branch sections *g* and *h* with emanate from symmetric breaking point *SBy*. At a small angle of tilt, the resulting structure is a pair of limit points in the same vicinity that are not connected. After this occurs, branch *e* is joined with branch *h* at a limit point *Lw*, while branches *f* and *g* form another branch with a limit point at *Lv*. In the case of L8 and SB6, the two resulting limit points are labelled L8 and L14. This transition occurs at a tilt angle of less than 0.1°, due to the close proximity of L8 and SB6 in the untilted structure.

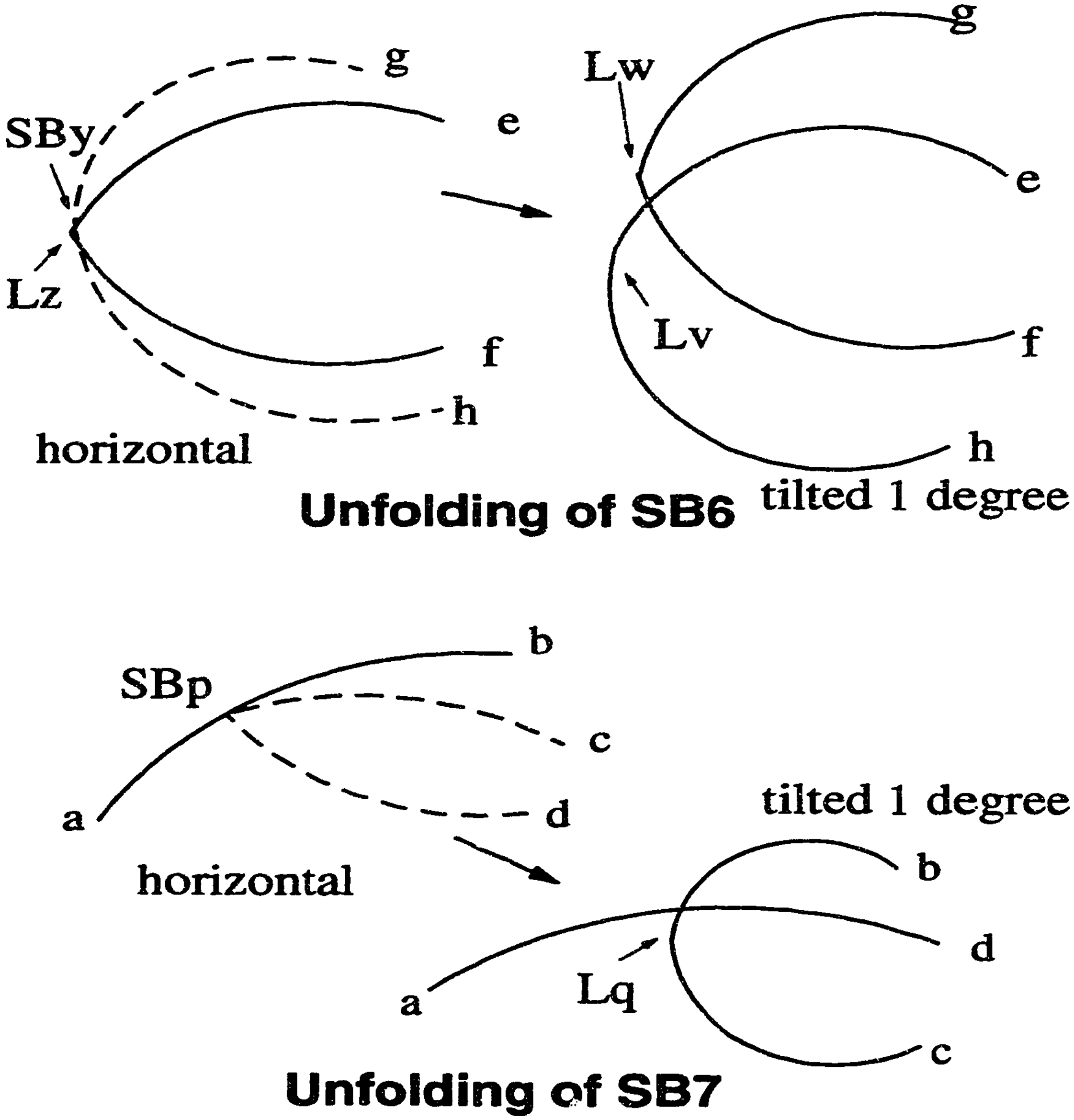

Figure 3.13: Unfolding of SB6 and SB7 when the Slab is Tilted

Classical unfolding of a pitchfork bifurcation occurs when SB7 unfolds. It is structurally unstable to asymmetric perturbation. The result is a continuous branch and an isolated branch, but with the view used here, the branches do cross. However, these branches do not intersect. A sketch of what takes place is also shown in Figure 3.13. Symmetric branch sections *a* and *b* form a continuous path, with asymmetric branches *c* and *d* meeting at symmetry-breaking point *SBp*. When tilting occurs, the unfolding of *SBp* results in the joining of branches *a* and *c* as the continuous branch, and branches *b* and *d* forming an isolated branch with limit point *SBq*. For the case of SB7 unfolding, the limit point is labelled L15.

3.6 Stability of Solution Branches

In order to monitor the stability on the various solution branches discovered, the following routine was used. For stable solutions, all eigenvalues of the Jacobian matrix A, which is the discretized form of $f_{\mathbf{u}}(\mathbf{u}, \mathrm{Ra}, \gamma, \phi)$ calculated at each Newton step, must have a negative real part. The complex function

$$w = \frac{(1+z)}{(1-z)}$$

maps the left half plane, which is the area of stability, onto the interior of a unit circle. If all eigenvalues of A have negative real parts, then the eigenvalues of the matrix

$$B = -(A-I)^{-1}\ (A+I)$$

will all fall inside the unit circle. This requires only the value of the largest eigenvalue as a test quantity, and it may be found through the use of a power iteration scheme.

Analysis of the stability of the solution branches for a porous slab of unit aspect ratio tilted one degree is summarized in Table 3.6. At a Rayleigh number of 500,

Rayleigh Number = 1000			
Branch	**Nusselt Number**	**Eigenvalue**	**Stability**
PM	9.6619	0.9118	stable
Rayleigh Number = 3000			
PM	12.4052	0.946±i0.0135	stable
AB1	12.4654	1.027	unstable
AB1	12.9772	1.029	unstable

Branch PM1		
Rayleigh Number	**Eigenvalue**	**Stability**
4000	0.9564±i0.0171	stable
4200	0.9825±i0.0276	stable
4400	0.9973±i0.0426	stable
4600	1.0053±i0.0542	unstable

Table 3.6: Onset of Instability within Tilted Porous Slab, $\gamma = 1.0, \phi = 1^\circ$

the unique solution branch PM was found to be stable. Branch PM continues to be stable at $Ra = 3000$, but is not the only solution. The upper and lower branches of AB1 are also present, but are both unstable. A Rayleigh number of 4000 is very near the point where the limit point L2 and symmetry-breaking point SB1 merge in a slightly tilted slab. At this point, branch PM was stable, while both branches of AB1 were again unstable. At a Rayleigh number between 4400 and 4600, branch PM became unstable. It is believed that this change in stability is due to the passing of the Hopf bifurcation originating with the unfolding of SB1 into L2. Confirmation of this conjecture is not possible at this time, as a scheme that could follow the path of oscillatory solutions has not been developed. Even if such a scheme did exist, the solution for a large dimensional discrete system such as this one would require more computing power than we have available.

The Hopf bifurcation continues to travel through the domain, generating oscillatory solutions and changing the stability of stationary branches. Figure 3.14 shows the points where this bifurcation point affects the stability of the unique solution branch PM at various tilt angles. Over a small range of Rayleigh number, up to 3000, there is a oscillation in the value of the largest eigenvalue, but it does not affect the stability of the branch. This oscillation disappears at higher Rayleigh number for the most part, and again does not affect the stability of the solution. These oscillations do not appear to be an artifact of the algorithm, as they are still apparent with the use of smaller tolerances in the power method. The point at which the unique solution branch became unstable moves to higher Rayleigh number as the tilt angle increased. For a slab tilted 20°, there was considerable waviness, but the branch remained stable. It appears that instability suddenly occurs at $Ra = 19500$, but this was not pursued as it may be only an artifact of the solution. At such a high Rayleigh number more sensitive grids would be required. Further study of such

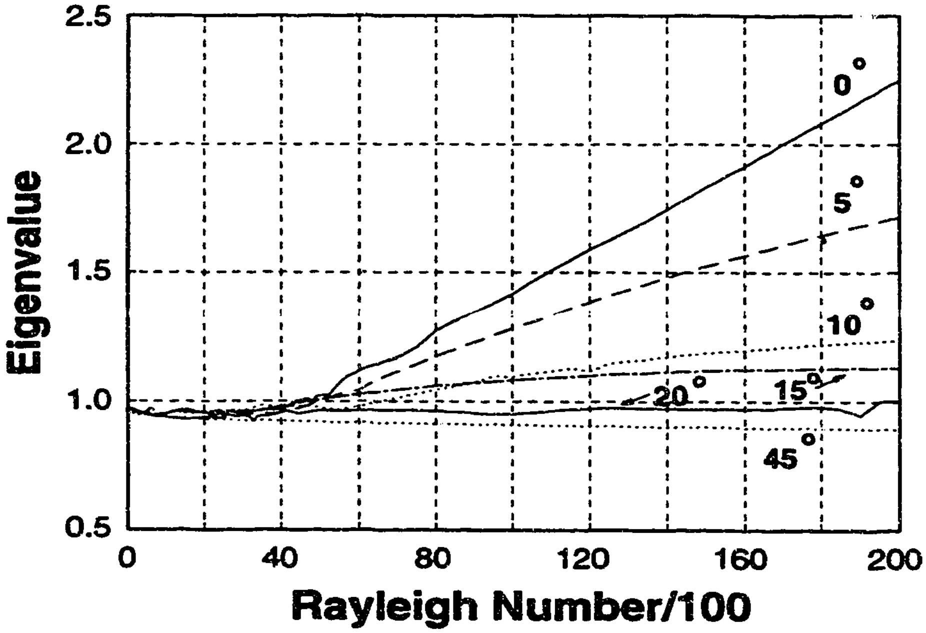

Figure 3.14: Eigenvalues of the Unique Solution Branch at Various Tilt Angles, $\gamma = 1.0$

a phenomenon was deemed to be outside the objectives of this study, but is also beyond our computational power at present.

For a slab tilted 45°, there was no sign of the primary solution branch becoming unstable. In fact, its largest eigenvalue was still decreasing at a Rayleigh number of 20000. This indicates that this branch is not only unique but is also globally stable. This is only evident for a slab with a unit aspect ratio. For nonsquare layers, there were always multiple solutions present at 45° of tilt. Only a slab with an aspect ratio of unity has a degree of reflective symmetry return at a tilt angle of 45°.

For a slab tilted one degree, all seventeen solutions were found to be unstable at the highest flows considered. This corresponds to no physically realizable solutions. The eigenvalues for these branches at $Ra = 10000$ are given in Table 3.7. All of the branches have their largest eigenvalues considerably greater than unity.

3.7 Flow Patterns and Isotherms

All seventeen solutions found at a Rayleigh number of 10000 for a unit aspect slab tilted one degree are shown in Figures 3.15 and 3.16. These figures includes streamline and isotherm plots. The odd number of solutions throughout the structure is due to the presence of a unique solution at low values of Rayleigh number. This solution branch is labelled PM in Figures 3.4 and 3.9. It corresponds to a two-cell pattern that is only slightly asymmetric, even at Rayleigh number of 10000. The asymmetry is shown in the slightly off-centered line in the middle of the streamline plot and the slightly greater spacing of isotherms in the lower right hand corner of the slab as compared to the lower left hand corner.

The streamlines and isotherms for AB1 and AB3 appear to be evolving into a new state. Branch AB1 is more advanced in this transition. The lower branches contain

Branch	**Flow Pattern**	**Eigenvalue**	**Stability**
F[illegible]M	2 cell	1.390±i0.2703	unstable
AB1 low	2 cell	1.178±i0.3550	unstable
AB1 high	4 cell	1.043	unstable
AB3 low	2 cell	1.092±i0.4215	unstable
AB3 high	4 cell	1.266	unstable
AB6 low	2 cell	1.363±i0.2928	unstable
AB6 high	weak 4 cell	1.327±i0.0558	unstable
AB8 low	developing 4 cell	1.227	unstable
AB8 high	4 cell	1.128	unstable
AB10 low	2 cell	1.530±i0.0614	unstable
AB10 high	developing 4 cell	1.487	unstable
AB13 low	developing 4 cell	1.205	unstable
AB13 high	4 cell	1.112±i0.0077	unstable
AB11 low	weak 4 cell	1.317±i0.0533	unstable
AB11 high	weak 4 cell	1.215	unstable

Table 3.7: Eigenvalues of Solution Branches, $Ra = 10000, \gamma = 1.0, \phi = 1.0°$. Maximum of 30 iterations for convergence, Tolerance $= 1.0E - 5$

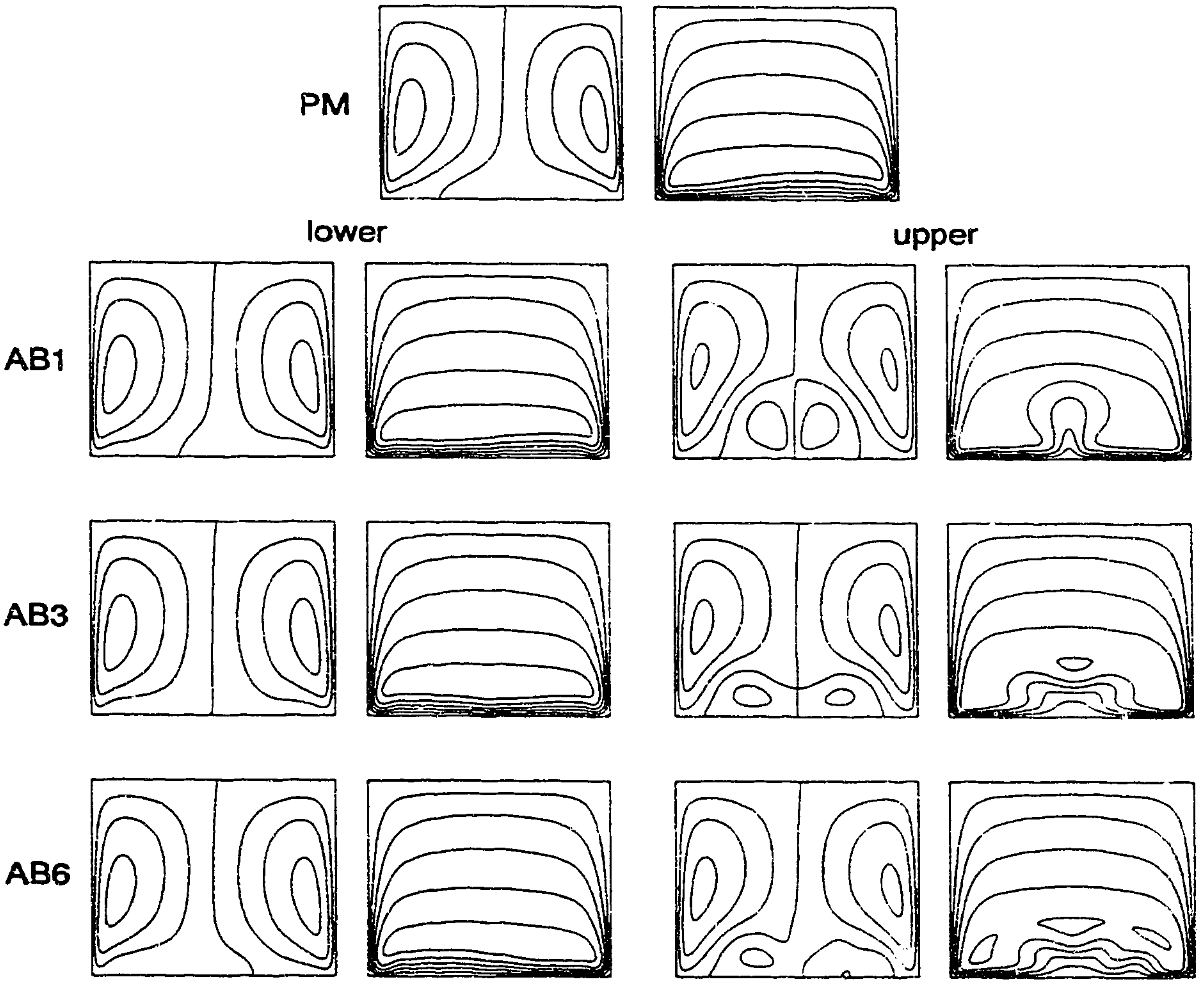

Figure 3.15: Streamline and Isotherm Plots of Stationary Solutions at $Ra = 10000, \gamma = 1.0, \phi = 1°$

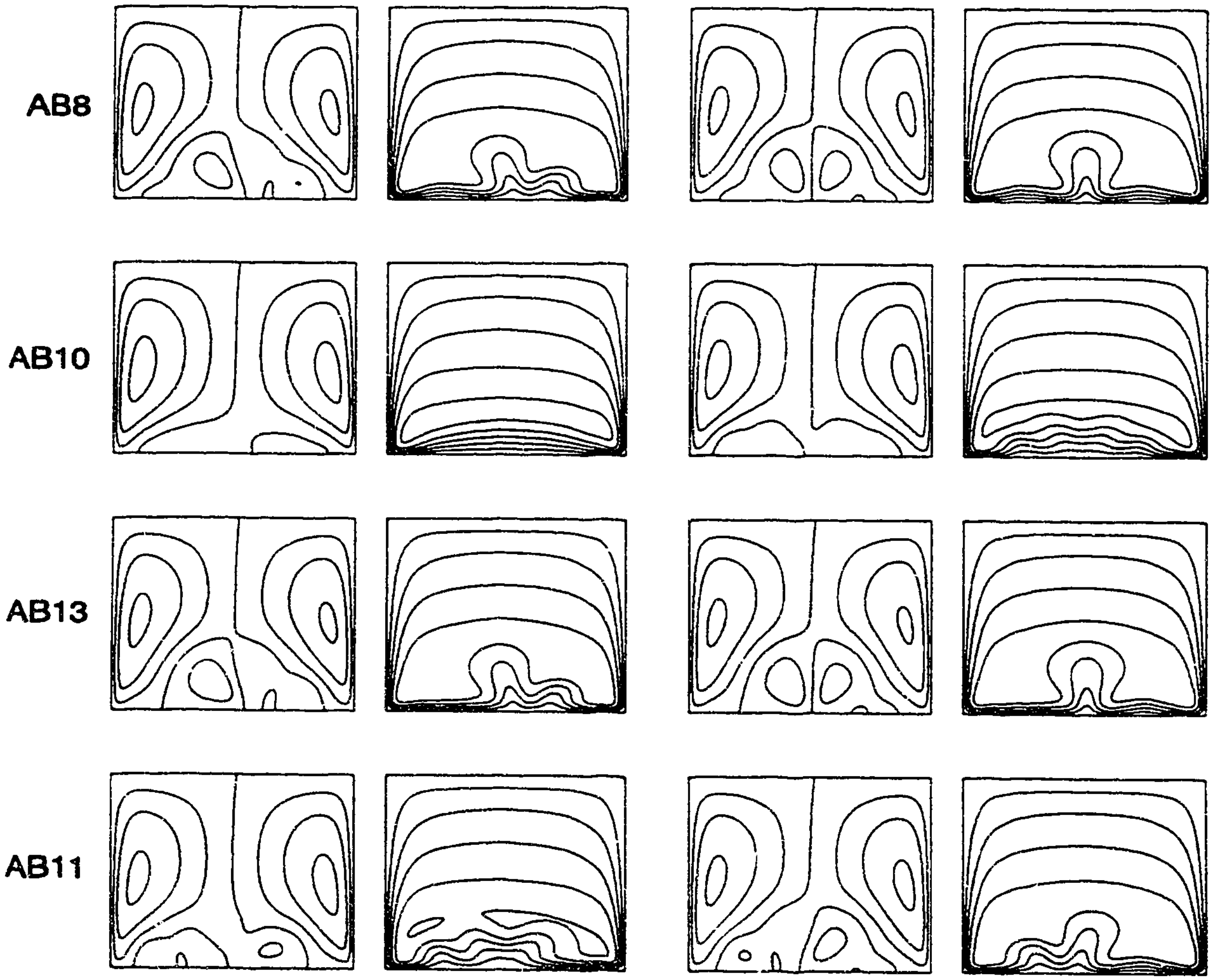

Figure 3.16: Streamline and Isotherm Plots of Stationary Solutions at $Ra = 10000, \gamma = 1.0, \phi = 1^\circ$ (continued)

strong two-cell flow, while the upper branches contain strengthening four-cell flow. The secondary flow cells in the center near the bottom wall are not as large in the streamlines of AB3 as in AB1. Isotherms at the center near the bottom wall in AB3 are wavy, but are not penetrating up the middle of the cell like their counterparts in AB1. At aspect ratios greater than unity, the solution branch corresponding to this part of AB3 in the untilted slab is expected to bifurcate into a flow pattern with six flow cells. When these transitions are complete, and other flow structures like a six-cell flow begin, another limit point is expected.

The limit point is the transition point between a two-cell and four-cell flow in AB1 and AB3. In the case of AB6 and AB10, the four-cell flows are also present in the upper branch. One of these cells dissipates as the Rayleigh number increases when following the upper branch. The waviness at the bottom of the isotherm plots of the upper branches of AB6 and AB10 are a sign that the four cell flow is diminishing.

The streamline and isotherm patterns for both branches of AB8 and AB13 are strikingly similar to each other. Both upper branches contain strong four-cell flow patterns and the beginnings of the creation of two cells in the isotherms. The lower branches both contain three strong flow cells and the beginnings of a fourth flow cell.

The most complicated flows are seen at either end of AB11. Both solutions may be characterized as three cell flows, but there appears to be the beginnings of a fourth cell. The isotherms in both cases are beginning to rise in the center. This is an indication that the fourth cell is gaining in strength.

All of these solution branches have been calculated to be unstable. However, transient studies on this system have shown that these flow patterns do exist. The transient path hops between these unstable solutions. Discussion of such phenomena can be found in the paper by Ryland and Nandakumar [96].

3.8 Effect of Larger Tilt Angles

3.8.1 Unique Solution Region

The effect of tilting the slab very slightly has been investigated. Consideration of the change in solution structure when the slab is tilted larger amounts is now considered. Fold curves for the limit points robust to tilt when the tilt angle changes are shown in Figure 3.17 for a slab with unit aspect ratio. In general terms, the Rayleigh number of the limit point increases with increasing tilt angle. The fold curves of most limit points in this system eventually become vertical and are asymptotic to a certain tilt angle. In the case of bottom heated porous layers, at high tilt angles, some limit points eventually merge together at a second turning point and form an isola which shrinks and disappears upon further tilting [95]. Behaviour of this type was not discovered in this system.

In the case of L1, the fold curve is asymptotic to an angle of 42.9155°. Beyond this angle, there is no multiplicity in the solution. Only the unique solution branch exists, and it is stable for all values of Rayleigh number, as was mentioned when stability was discussed.

3.8.2 Discontinuities in Fold Curves with Tilt

The fold curves of limit points L3, L6 and L10 do not follow the trend of increasing Rayleigh number with increasing tilt angle over various values of tilt angle, as is apparent in Figure 3.17. In the case of L3, the Rayleigh numbers at

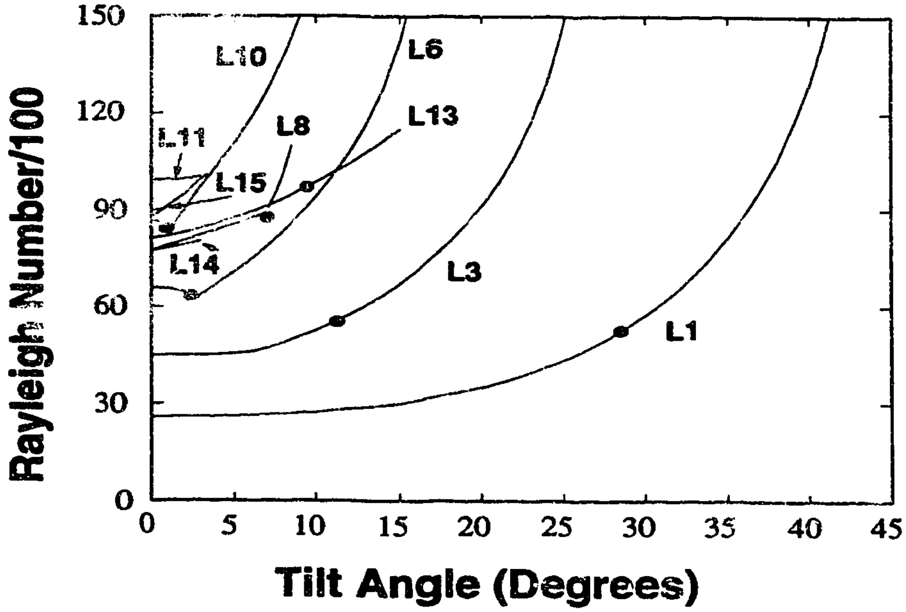

Figure 3.17: Fold Curves in Tilt of Limit Points Robust with Tilt, $\gamma = 1.0$

the limit point decrease slightly with increasing tilt angle until $\phi = 2.5°$, where the curve bottoms out and follows the trend of the other fold curves. This transition is very smooth, indicating the absence of a higher order singularity.

In the case of the fold curve of L6 with tilt, at first the Rayleigh number increases with tilt, and then gradually begins to decrease after the slab has been tilted 0.3°. However, in order for the Rayleigh number to again increase with increasing tilt, a transition in the form of a discontinuity occurs at $\phi = 2.7°$. Just before this discontinuity occurs, a B-point was discovered in the structure. The presence of a B-point here indicates that this discontinuity is also of the Takens-Bogdanov form.

Consideration of the value of stream function near the discontinuity gives an indicator of where to search for the physical reason behind these discontinuities. As shown in Figure 3.18 the values of stream function at the position (0.9b, 0.1a) jump significantly when the break in the fold curve is encountered. Thus, a study of the contour plots on either side of the discontinuity should shed some light on what is happening there.

A physical explanation of the reasons behind this discontinuity can be deduced from inspection of the streamline plots of the solutions near the discontinuity. Figure 3.19 shows the contour plots for the limit point solutions at 2.7° and 2.8°. The symmetric solution of a horizontal slab contains a strong four-cell solution. Upon tilting, the cell on the lower right begins to lose strength. This accounts for the reduction of heat transfer upon tilt and the drop in Rayleigh number for the limit point position. Inspection of the streamline plots on either side of the discontinuity shows that the discontinuity is due to the change from a four-cell pattern into a three-cell pattern. The lower right hand secondary flow cell has been incorporated into the large primary cell on the left. This strenghtens the two primary flow cells and thus leads to increased heat transfer and higher Rayleigh numbers of the limit

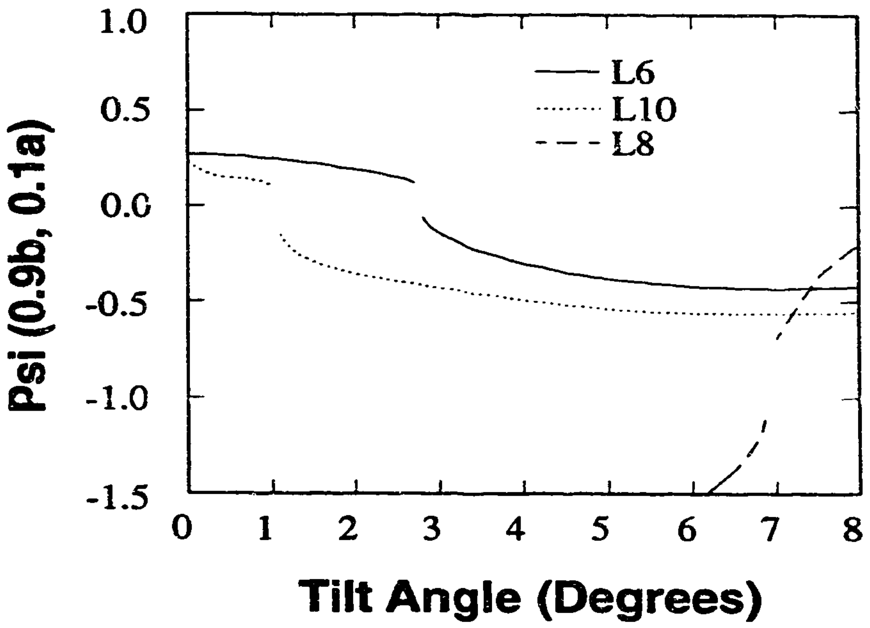

Figure 3.18: Stream Function values near the Discontinuities in the Fold Curves of L6, L8 and L10 with Tilt, $\gamma = 1.0$

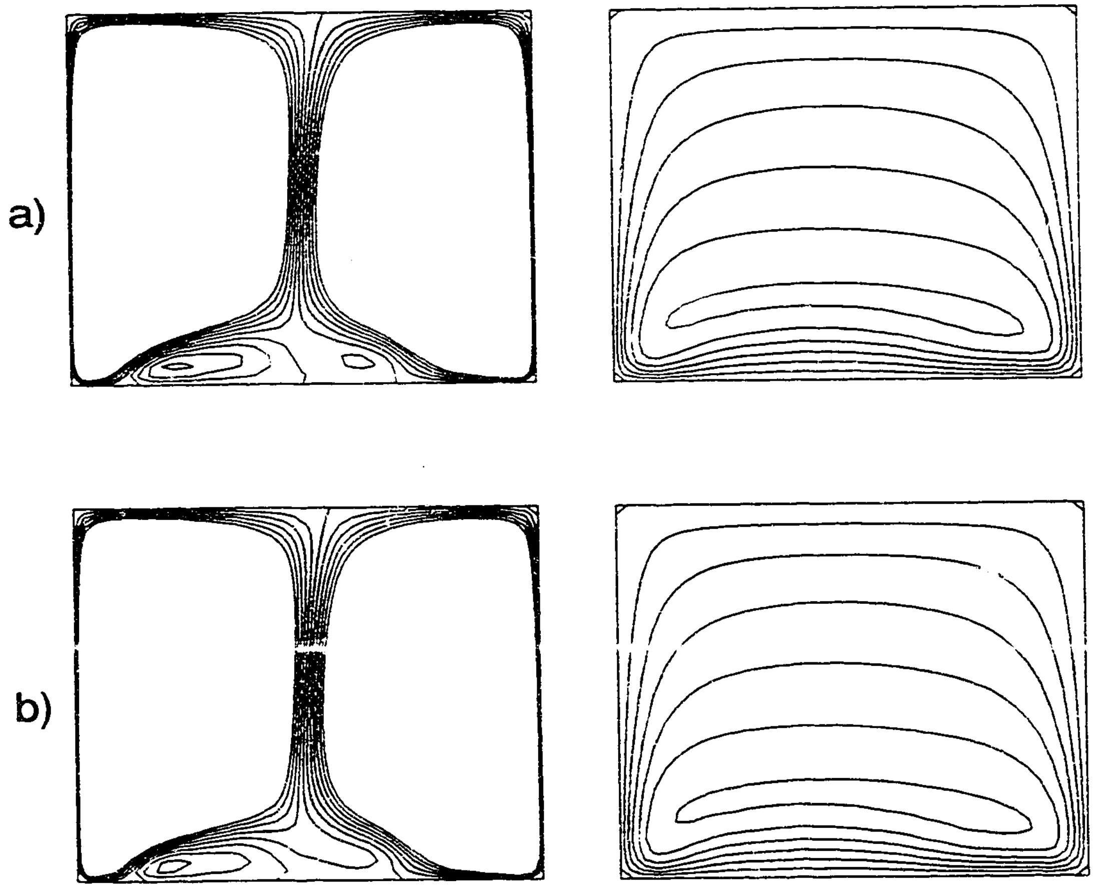

Figure 3.19: Streamline and Isotherm Plots near the Discontinuity in the Fold Curve of L6 with Tilt, $\gamma = 1.0$. a)$\phi = 2.7°$, b)$\phi = 2.8°$.

point as tilt further increases.

A similar discontinuity to that found on the fold curve with tilt for L6 is also found on the tilt fold curve for L10. In this case it is found at $\phi = 1.1°$. Again, there is a B-point present just before the occurrence of the discontinuity. Contour plots near this discontinuity, shown in Figure 3.20, indicate that there are physical phenomena here similar to those which caused the discontinuity in L6. A four-cell flow pattern becomes a three-cell pattern after the discontinuity, resulting in increased heat transfer due to the growth of the primary cells.

There is also a discontinuity present in the fold curve of L8, which again is closely preceeded by a B-point. This is a different situation, as the change in slope of the fold curve is not from negative to positive. Again, inspection of contour plots near the abrupt change, shown in Figure 3.21, lead to a physical explanation. It is a reverse situation of the previous discontinuities. A new flow cell is formed along the lower right-hand surface of the slab, emerging from a primary cell.

At the discontinuity, the fold curve ceased to exist, yet was not vertical. The thought was that a higher order bifurcation similar to those seen in the fold curves of aspect ratio was present. In an attempt to continue travelling along this branch, computations were performed to circumvent this point. The following path was calculated. From a tilt angle of one degree and a unit aspect ratio, the aspect ratio was increased to two. From here, the slab was tilted to a value of 10°. The aspect ratio was then reduced to unity. Lastly, the slab was returned to a tilt of one degree. It was expected that this path would fail at some point, this giving an extension of the fold curve of L8. However, the complete path was traced and resulted in a different value of Rayleigh number for the same values of tilt angle and aspect ratio. This branch is labelled AS4 in the horizontal structure and contains the limit point AL13. In the tilted structure the limit point is again L13, but the resulting branch

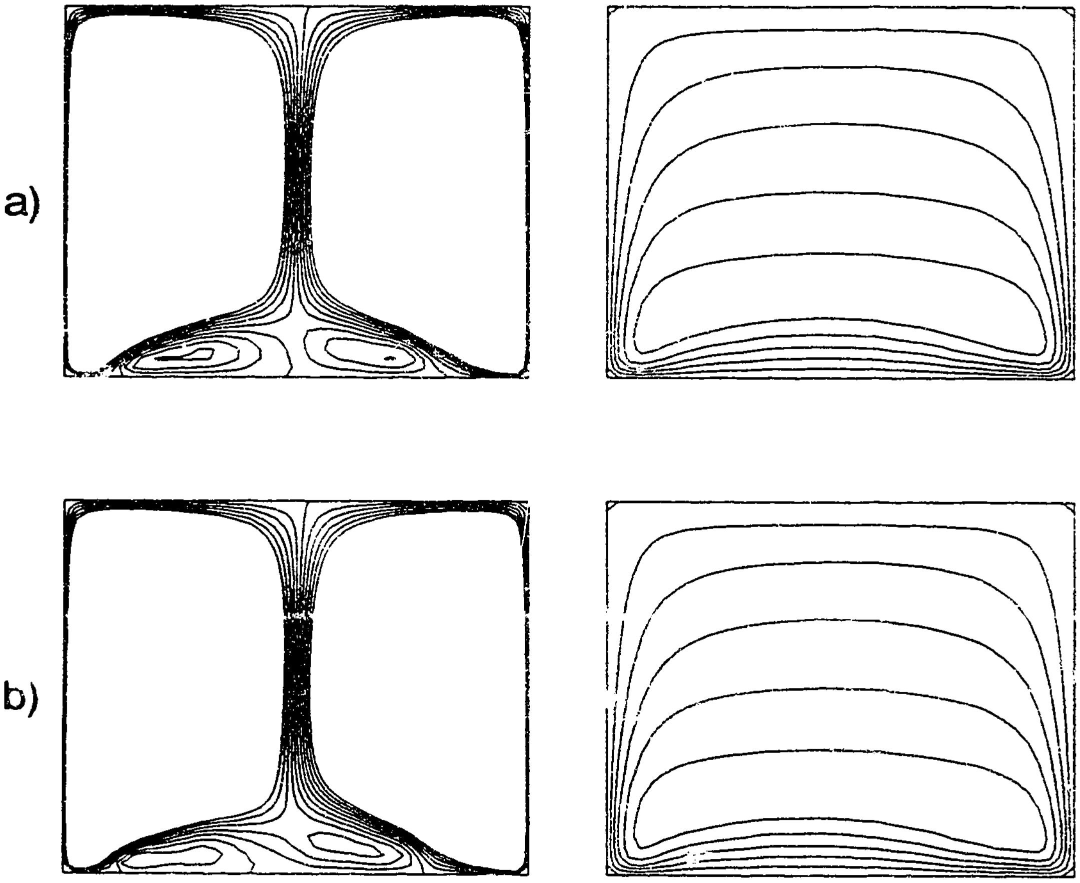

Figure 3.20: Streamline and Isotherm Plots near the Discontinuity in the Fold Curve of L10 with Tilt, $\gamma = 1.0$. a)$\phi = 1.0°$, b)$\phi = 1.1°$.

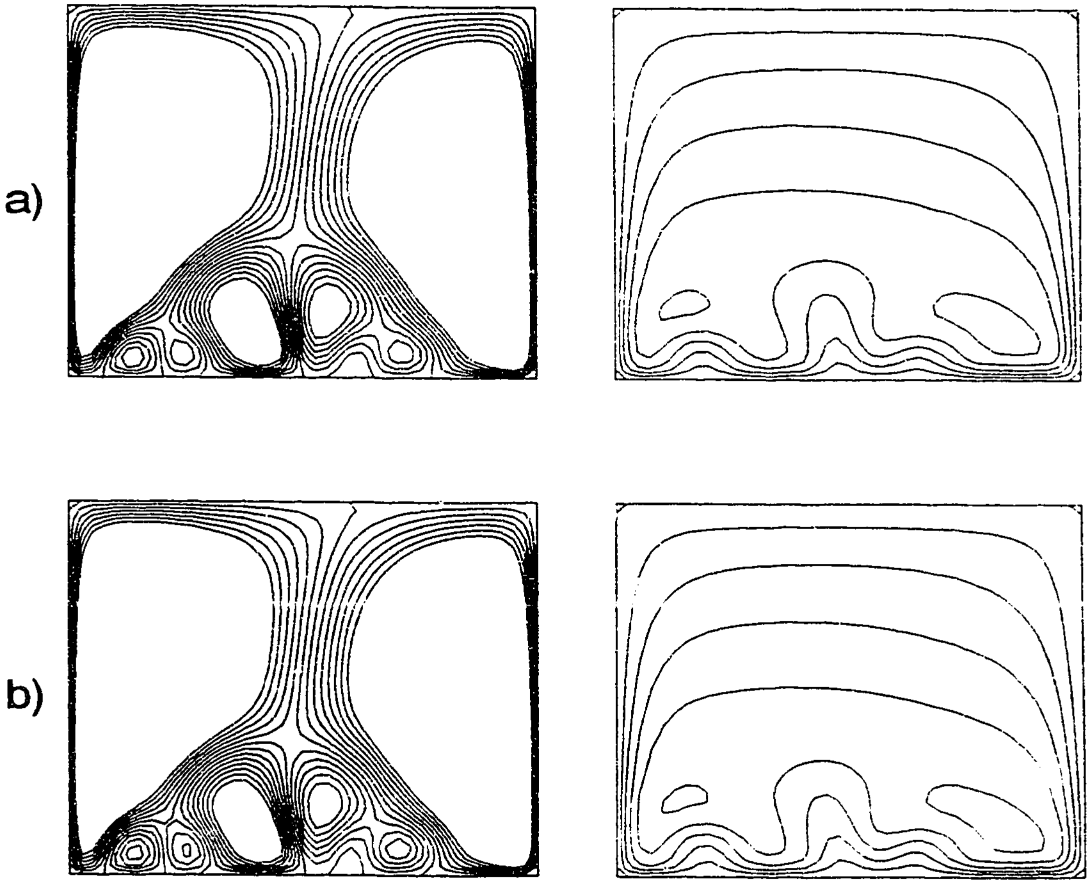

Figure 3.21: Streamline and Isotherm Plots near the Discontinuity in the Fold Curve of L8 with Tilt, $\gamma = 1.0$. a)$\phi = 6.8°$, b)$\phi = 7.0°$.

is labelled AB13.

It is obvious that the branches AB8 and AB13 are connected in some way. Their fold curves in aspect ratio are very close together for an aspect ratio of 2.0. The fold curve in tilt of L8 ends very close to the position of L13 at the same angle. The contour plots at 1° are strikingly similar. These facts suggest that branches AB8 and AB13 are connected in some way. One possibility is a connection by a cusp catastrophe or some other type of higher order behavior.

3.9 Variation of Aspect Ratio

Limit points which were robust to tilt were tracked throughout the parameter range of aspect ratio using Euler-Newton continuation on the extended system. The fold curve for extrapolation in aspect ratio in shown in Figure 3.22. The relative length to height of the slab was varied. In general, the value of Rayleigh number at the limit point decreased with increasing aspect ratio. The fold curves of L6, L8 and L10 did no exist all the way to the lower edge of the domain at $\gamma = 0.5$. The curve of L10 ends at $\gamma = 0.992$, while the fold curves of L6 and L8 end at $\gamma = 0.65$ and $\gamma = 0.63$, respectively. Higher order bifurcations, such as limit points on fold curves, could not be handled by the routine used in these simulations. Efforts to extend these branches any further failed. No B-points were discovered on any of these fold curves.

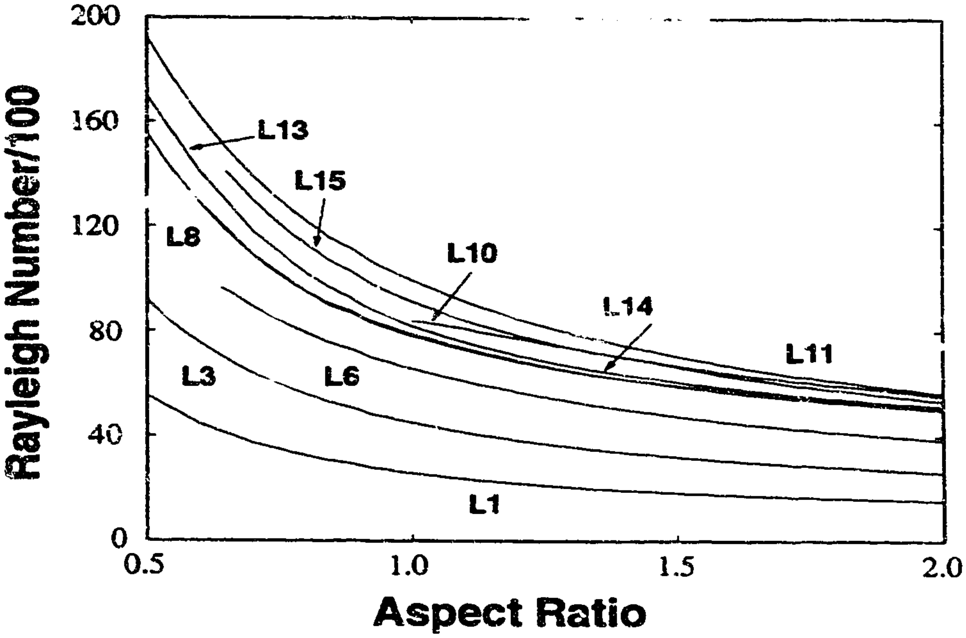

Figure 3.22: Fold Curves in Aspect Ratio of Limit Points Robust with Tilt, $\phi = 1^\circ$

Chapter 4

Hele-Shaw Cell Simulations

4.1 Physical Description

A Hele-Shaw cell is defined as thin fluid-filled gap. It was first considered for study by Hele-Shaw [27] in 1898. At that time it was suggested that an analogy between the flows in these cells and the flow in porous media did exist. This idea was based on the similarity between the Darcy equation and the Navier-Stokes equations for flow in a thin gap. In order to use this analogy, a *permeability* for the fluid layer has to be defined. The value used most often is $d^2/12$, where d is the width of the thin gap. Others have attempted to account for the heat loss through the large side walls in non-isothermal flows within the permeability [29]. The similarity between flow within fluid and porous layers is often exploited by using Hele-Shaw cells as a substitute for a porous layer in an experimental program. The results from these studies are then adapted for use in practical situations, such as two-phase displacements in oil reservoirs [36, 38].

In the case investigated in this dissertation, the Hele-Shaw cell is of vertical orientation and rectangular cross-section, as shown in Figure 4.1.

The cell may be tilted at any angle above or below the horizontal. It is filled with a fluid which may be heated internally. The peripheral walls are impermeable and are at a uniform, constant temperature. The geometry of this test cell system is meant to correspond with the porous cell described earlier.

4.2 Governing Equations

The cell is a closed system, which means there is no flow in or out. The continuity equation is of the form:

$$\frac{D\rho}{Dt'} + \rho(\nabla' \cdot \mathbf{u}') = 0 \tag{4.1}$$

The Navier-Stokes equation is applied to describe the momentum transfer within the fluid. Other mathematical models for Hele-Shaw cells have simplified the Navier-Stokes equation through the use of the boundary layer approximation [103]. The boundary layer approach has merit due to the defined small dimension in the direction of the gap. It is possible that the hydrodynamic boundary layers of both side walls do meet within the center of the fluid gap. However, they may not, and thus will not account for flow within the center of the region. It is also not necessary to simplify the model with introduction of boundary layers, as solution without them is possible. The Navier-Stokes equation is written in the following form:

$$\rho[\mathbf{u}'_{t'} + (\mathbf{u}' \cdot \nabla')\mathbf{u}'] = -\nabla' p' + \mu\Delta\mathbf{u}' - \rho\mathbf{g} \tag{4.2}$$

In the direction across the thin gap, the momentum equation need not be solved. The so-called "small-gap approximation" can be used, as was done in [4]. For Poiseuille flow between closely spaced flat plates which are infinite in two directions, the Navier-Stokes equation will give a parabolic velocity profile as a solution. The

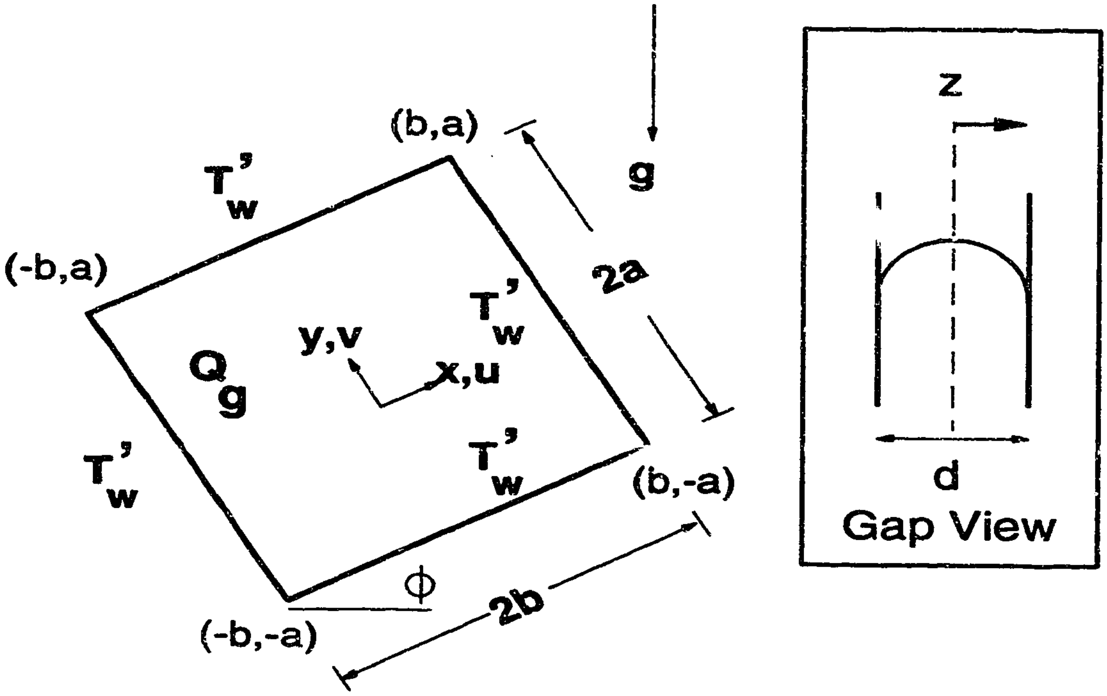

Figure 4.1: Geometry of Hele-Shaw cell

parabolic profile will be the exact solution for this limiting case. A system where the flat plates are finite and closely spaced is present here. However, if the dimensions of the flat plates are much larger than the width of the gap between them, the use of a parabolic velocity profile is a good approximation of the flow. In the experimental portion of this study, the length of the flat plate is $3in$ while the width of the fluid gap is $1/8in$. This corresponds to a length to gap width aspect ratio of 24/1, which is sufficient to justify the use of a parabolic velocity profile. In mathematical terms, the parabolic profile is of the form:

$$f(z') = \frac{3}{2}[1 - (2\frac{z'}{d})^2] \tag{4.3}$$

and the velocity components may be written as:

$$\mathbf{u}'(\mathbf{x}', \mathbf{y}', \mathbf{z}', \mathbf{t}') = \mathbf{U}'(\mathbf{x}', \mathbf{y}', \mathbf{t}')\mathbf{f}(\mathbf{z}') \tag{4.4}$$

The expression for the parabolic velocity profile is correct for the case where the boundaries of the domain in the z' direction are labelled as $z' = \pm\frac{d}{2}$. The resulting fluid velocity terms are neither superficial nor interstitial velocities. The averaging that has taken place is different than that found in volume averaging due to the use of the parabolic velocity profile in the direction of the gap.

Substitute these functions and the linear temperature dependence of the fluid density within the buoyancy term into the Navier-Stokes equation. The following form for the momentum equation is the result:

$$f(z')\mathbf{U}'_{t'} + [f(z')^2(\mathbf{U}' \cdot \nabla')\mathbf{U}'] = -\nabla' p'/\rho + \nu\Delta'[\mathbf{U}' f(z')] + \beta(T' - T'_o)\mathbf{g} \tag{4.5}$$

The only new term that emerges in this equation is $\Delta[U' f(z')]$. The second derivative of $f(z')$ has a value of $-12/d^2$. This term will now be referred to as $-1/K$, since it is the inverse of the permeablility defined for the fluid gap. If the momentum equation is now integrated across the gap, it takes the form:

$$\mathbf{U}'_{t'} + \frac{6}{5}(\mathbf{U}' \cdot \nabla')\mathbf{U}' = -\nabla' p'/\rho + \nu[\Delta'\mathbf{U}' - \frac{1}{K}\mathbf{U}'] + \beta[\overline{T} - T'_o]\mathbf{g} \qquad (4.6)$$

The factor 6/5 is due to the fact that:

$$\frac{1}{d}\int_{-d/2}^{d/2} f(z')^2 dz = 6/5$$

The energy equation must contain a term to account for the internal heat sources. It is of the form

$$T'_{t'} + (\mathbf{u}' \cdot \nabla')T' = \alpha\Delta' T' + Q_g/(\rho_f C_{p_f}) \qquad (4.7)$$

where:

$$\alpha = k_f/(\rho C_p)_f$$

It is assumed that the large sidewalls are adiabatic, and that the fluid temperature does not vary across the gap. Invariant fluid temperature in the z-direction is reasonable as long as the internal heating rate remains low. Integration of the energy equation across the gap leads to averaged quantities for the temperature, but the form of the equation is the same.

$$\overline{T}_{t'} + (\mathbf{U}' \cdot \nabla')\overline{T} = \alpha\Delta'\overline{T} + Q_g/\rho_f C_{p_f} \qquad (4.8)$$

Cross-differentiation of the two momentum equations eliminates the pressure term. The stream function-vorticity formulation is introduced here as well. The resulting three equations are of the form:

$$\Omega'_{t'} = -\frac{6}{5}[\psi', \Omega'] + \nu(\Delta'\Omega' - \frac{1}{K}) + \beta g(\cos\phi\frac{\partial(\overline{T} - T'_o)}{\partial x'} - \sin\phi\frac{\partial(\overline{T} - T'_o)}{\partial y'}) \qquad (4.9)$$

$$\Delta'\psi' + \Omega' = 0 \qquad (4.10)$$

$$\overline{T}_{t'} = \psi_{x'}\overline{T}_{y'} - \psi_{y'}\overline{T}_{x'} + \alpha\Delta'\overline{T} + Q_g/\rho_f C_{p_f} \qquad (4.11)$$

These equations are made dimensionless using the following scale factors

$$x = x'/b \qquad \psi = \psi'/\nu$$
$$y = y'/a \quad \Omega = \Omega'/(\nu/a^2)$$
$$\tau = t'/(a^2/\nu) \quad \theta = \frac{T - T_o'}{(Q_g a^2/k)}$$

The final form of the equations describing the flow and heat transfer in a Hele-Shaw cell are

$$\Omega_\tau = \Delta_\gamma^H \Omega - \frac{6}{5\gamma}[\psi, \Omega] - \frac{1}{\xi}\Omega + Gr(\frac{1}{\gamma}\theta_x \cos\phi - \theta_y \sin\phi) \tag{4.12}$$
$$\theta_\tau = \frac{1}{Pr}\Delta_\gamma^H \theta - \frac{1}{\gamma}[\Psi, \theta] + \frac{1}{Pr} \tag{4.13}$$
$$\Delta_\gamma^H \psi + \Omega = 0 \tag{4.14}$$

where:

$$Gr = \frac{Q_g \beta g a^5}{k\nu^2} \quad Pr = \nu/\alpha$$
$$\gamma = b/a \quad \xi = d^2/12a^2$$
$$\Delta_\gamma^H = \frac{1}{\gamma^2}\frac{\partial^2}{\partial x^2} + \frac{\partial^2}{\partial y^2}$$

Only steady-state solutions are considered, so all time dependent terms are neglected.

This problem has five independent parameters. These are the Grashof number or flow parameter, the aspect ratio of the sl[illegible] tilt angle, the Prandtl number, and an inertia parameter. For this study, we are considering an analogy to a porous layer saturated with a dilute aqueous fluid, so the Prandtl number will be set at a value of 7.0. The inertia parameter ξ is fixed by the size of the gap that is chosen. In the experimental program, the test region has a unit aspect ratio, with a height of $3in$. The width of the fluid gap is $1/8in$. This results in a ξ value of 0.000579.

Grid Size	Gr=100000	Gr=300000 high
19x19	10.3787	14.0949
29x29	10.3568	14.1057
39x39	10.3262	14.0285

Table 4.1: Grid Sensitivty of Nusselt Number at Points along Branch PM1, $\phi = 0°, \gamma = 1.0, \xi = 0.000579, Pr = 7.0$

4.3 Numerical Methods

The resulting numerical model for the Hele-Shaw cell is similar to that posed for the porous medium with the following execeptions. There are three non-linear coupled partial differential equations present instead of only two. These equations also include the contribution of vorticity terms. The form of these equations is very similar to the model of forced flow within an empty heated duct put forward by Nandakumar and Weinitschke [90]. The difference in these models is that the forced flow model requires an extra equation to account for the forced flow in the direction perpendicular to the cross-section. Such an equation is extraneous in the Hele-Shaw cell. There is also no term to correspond with the inertia parameter within the model for an empty heated duct.

The domains, symmetry properties and numerical methods presented for the solution of the porous slab problem are also applicable to solve the flow within the Hele-Shaw cell.

A grid sensitivity analysis was also performed on the Hele-Shaw cell solution structure. The results of these tests are shown in Tables 4.1 and 4.2. A grid spacing of 39 × 39 interior points was chosen for this system to facilitate the comparison of the solution obtained here with the solutions for the porous slab of comparable geometry. The change in grid spacing did have a significant effect on the Grashof

Grid Size	Rayleigh Number	Nusselt Number
19x19	169542.7	11.7948
29x29	167577.0	11.7616
39x39	165991.1	11.6941

Table 4.2: Grid Sensitivity of Position and Nusselt Number at Limit Point L1, $\phi = 0°, \gamma = 1.0, \xi = 0.000579, Pr = 7.0$

number of limit point L1, but this effect was decreasing at the selected grid.

4.4 Solution Structure for Hele-Shaw Cell

4.4.1 State Diagram with Nusselt Number

The solution structure for convection in the vertical Hele-Shaw cell with internal heat sources is shown in Figure 4.2. The structure is very complicated, with one unique symmetric solution branch, two isolated symmetric solution branches, and seven asymmetric solution branches. To clearly show the large number of solution branches for $Gr \geq 500000$, and enlarged view of this region in shown in Figure 4.3. There are a total of fifteen solutions at a Grashof number of 700000, which is the edge of the domain studied. Several simple limit points and symmetry-breaking points exist within the structure. A summary of the locations of these points are given in Tables 4.3 and 4.4. The labelling of bifurcation points and solution branches has been conducted so that a bifurcation point within the Hele-Shaw structure has a matching label with a corresponding point within the porous slab solution structure.

As was the case with the porous slab, symmetry breaking points were detected near several limit points. The primary branch PM1 contains two limit points L1 and L2 and a symmetry breaking point SB1. The symmetric branch IS1 contains three

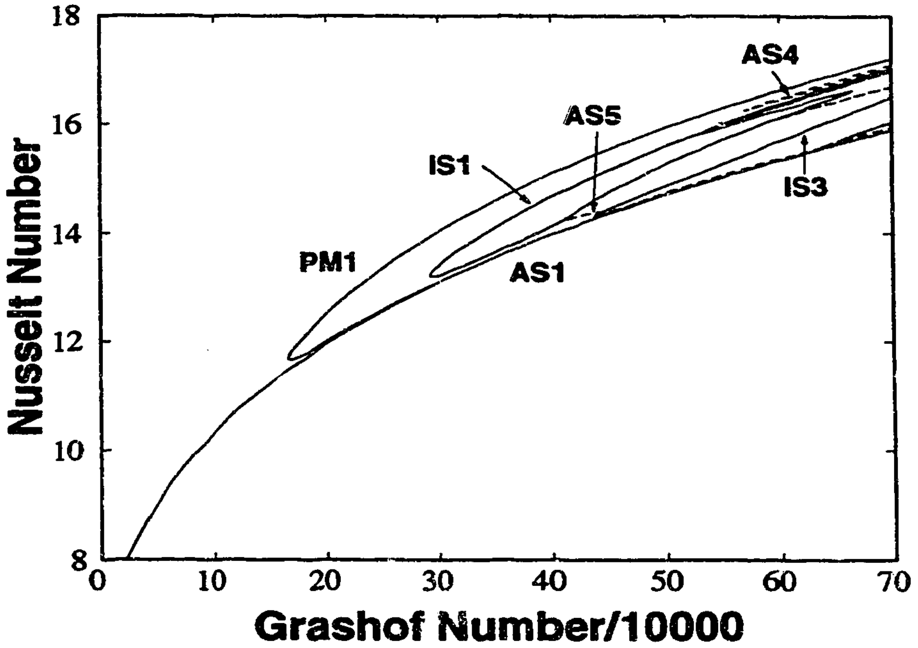

Figure 4.2: Solution Stucture for a Hele-Shaw cell, $\phi = 0°, \gamma = 1.0, \xi = 0.000579, Pr = 7.0$

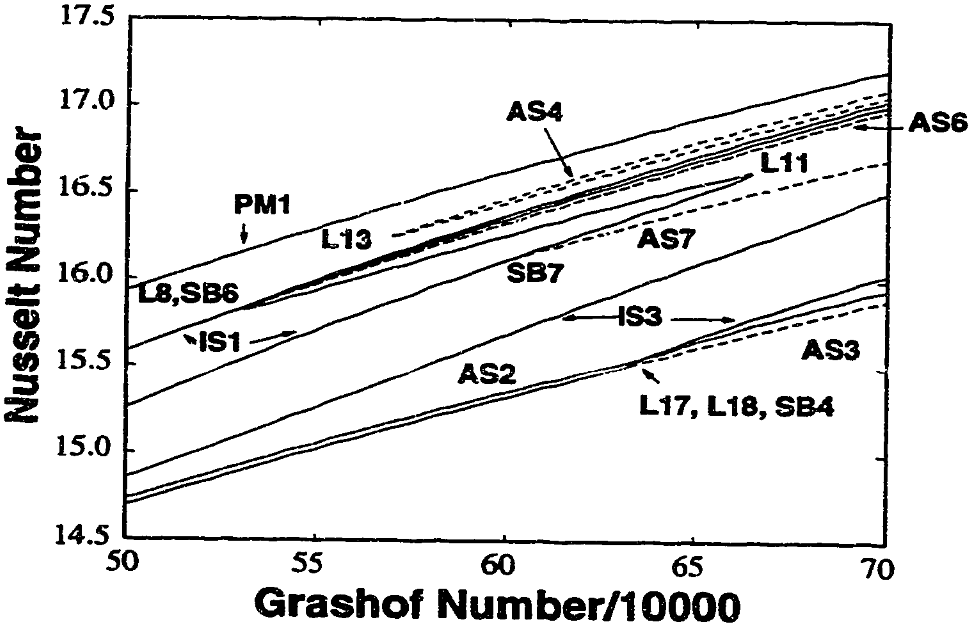

Figure 4.3: Solution Structure for a Hele-Shaw cell, $\phi = 0°, \gamma = 1.0, \xi = 0.000579, Pr = 7.0$

Label	**Branch**	**Grashof Number**	**Nusselt Number**
L1	PM1	165991.1	11.6941
L2	PM1	300034.0	13.0968
L3	IS1	291616.6	13.2121
L4	IS3	435923.1	14.2502
L5	IS3	438081.4	14.2909
L8	IS1	530662.4	15.8248
L11	IS1	664659.4	16.6222
L13	AS4	569434.8	16.2456
L16	IS3	438079.1	14.2946
L17	IS3	631818.6	15.5122
L18	IS3	632003.6	15.5093

Table 4.3: Limit Points in the Hele-Shaw Cell Structure, $\phi = 0°, \gamma = 1.0, \xi = 0.000579, Pr = 7.0$

Label	**Branches**	**Grashof Number**	Nusselt Number
SB1	PM1+AS1	299925.4	13.0964
SB2	IS3+AS1	436088.6	14.2502
SB3	IS3+AS2	437806.6	14.2773
SB4	IS1+AS3	631984.8	15.5095
SB6	IS1+AS6	531209.9	15.8333
SB7	IS1+AS7	600437.1	16.1174
SB8	IS1+AS5	410275.4	14.2442
SB9	IS3+AS5	443367.7	14.3776

Table 4.4: Symmetry-Breaking Points in the Hele-Shaw Cell Structure, $\phi = 0°, \gamma = 1.0, \xi = 0.000579, Pr = 7.0$

limit points and two symmetry-breaking points. It is an isolated branch that sits just above branch AS1. Symmetric solution branch IS3 is much more complicated than IS1. The differences in the Nusselt number on the upper and lower sections of this branch are not large. However, there are five limit points and four symmetry-breaking points on this branch alone.

The most complicated region of branch IS3 is at the end with lowest Grashof number, where there are three limit points and three symmetry-breaking points in close vicinity. This region, with a Grashof number of about 430000, is shown in more detail in Figure 4.4. All of these limit points are in close vicinity with symmetry breaking points. The merging of these limit points with symmetry-breaking points upon tilt results in significant changes in the solution structure. The fact that so many simple limit points are in the same vicinity of symmetry-breaking points leads to complex interactions as parameters are varied.

At Grashof number values of about 630000, another pair of limit points are found along the lower branch of IS3. This region of the parameter space is isolated in Figure 4.5. The limit point L18 and the symmetry-breaking point SB4 will merge upon tilt, leaving the limit point L17 to continue. The symmetry-breaking point SB4 is the genesis of the asymmetric branch AS3, which continues out of the domain.

There are five other asymmetric solutions within the structure. Branch AS1 is the link between the primary solution branch and the isolated symmetric solution branch IS3. Branch AS4 seems to float within the domain attached to no symmetric branch through a symmetry breaking point. Extension of the ends of this branch to Grashof numbers of 2400000 gave no indication of a limit point or symmetry-breaking point. This branch was discovered in a similar manner to branch AS4 in the porous slab solution structure. Asymmetric solution branches AS6 and AS7 are similar to the corresponding branches found in the porous slab solution. Connecting

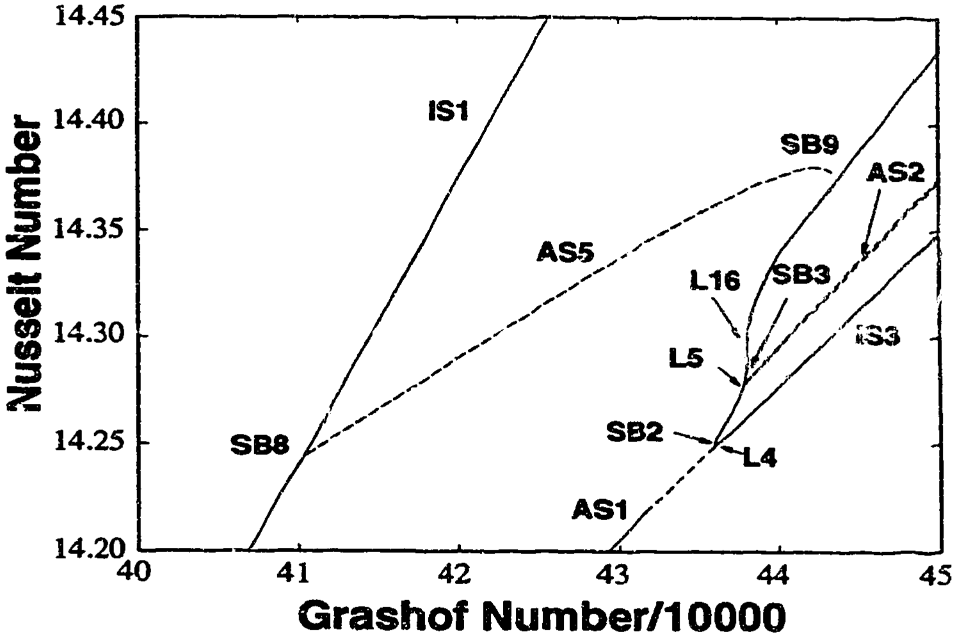

Figure 4.4: Region Near $Gr = 430000, \phi = 0°, \gamma = 1.0, \xi = 0.000579, Pr = 7.0$

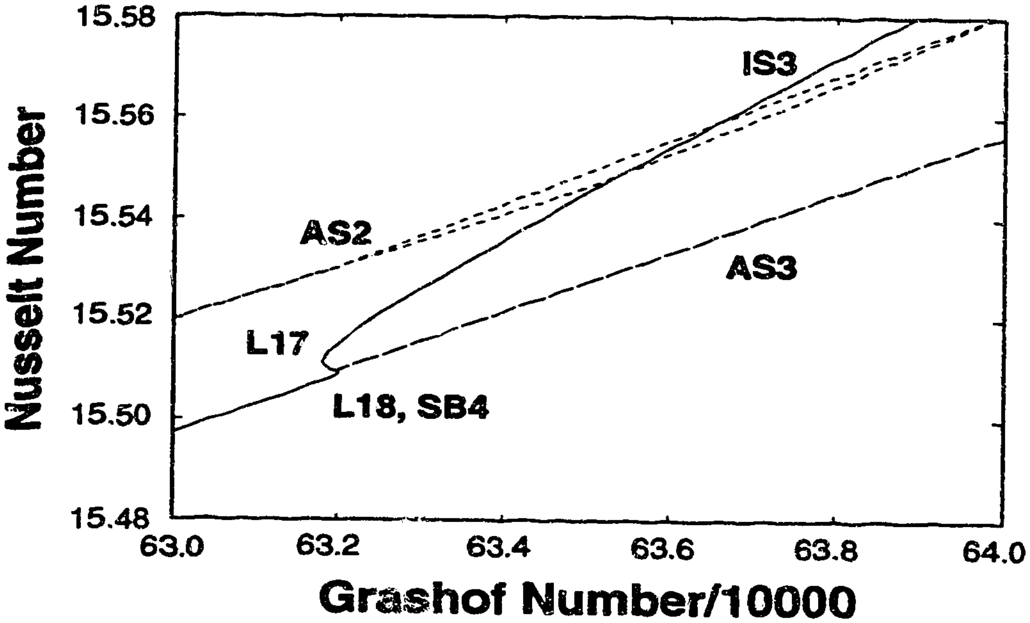

Figure 4.5: Region Near $Gr = 630000, \phi = 0°, \gamma = 1.0, \xi = 0.000579, Pr = 7.0$

the two isolated symmetric solution branches is asymmetric solution AS5.

4.4.2 State Diagrams with Dimensionless Temperature and Stream Function

A different look at the heat transfer solution structure for the Hele-Shaw cell with internal heating is given by using the dimensionless temperature or stream function at a point within the structure as the illustrative quantity instead of Nusselt number. These plots are shown in Figures 4.6 and 4.7, for dimensionless temperature and Figures 4.8 and 4.9 for stream function. The point chosen for the measurement of these quantities is a distance $0.1a$ from the top wall of the cell and $0.1b$ to the right of the centerline of the cell. This position was chosen as it is an area where a secondary flow cell emerges as a bifurcation point is passed. This is especially true when the slab is tilted above the horizontal, as the convection cell to the right of the centreline changes size and character.

The plot of the dimensionless temperature gives a clearer view of the separate character in each solution branch. The separate character of the asymmetric branches AS2 and AS3 are quite evident in Figure 4.6, even though their Nusselt numbers are quite similar. The branch AS5 is not very large, but it has very sharp changes near the symmetry-breaking points at its ends. It is also possible to observe the three closely spaced limit points on IS3 and their proximity with symmetry-breaking points.

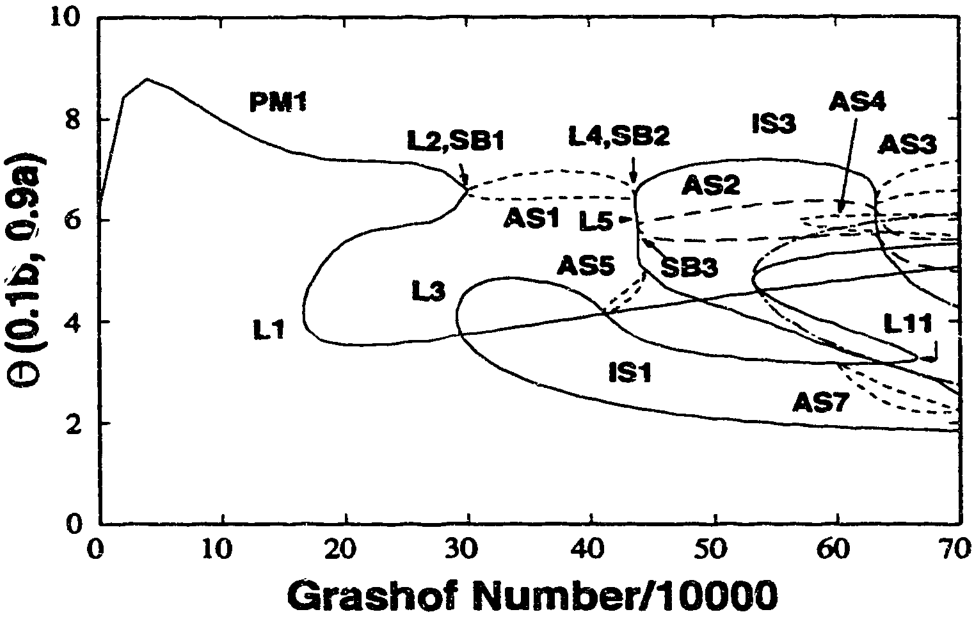

Figure 4.6: Solution Structure using Dimensionless Temperature as Parameter, $\phi = 0°, \gamma = 1.0, \xi = 0.000579, Pr = 7.0$

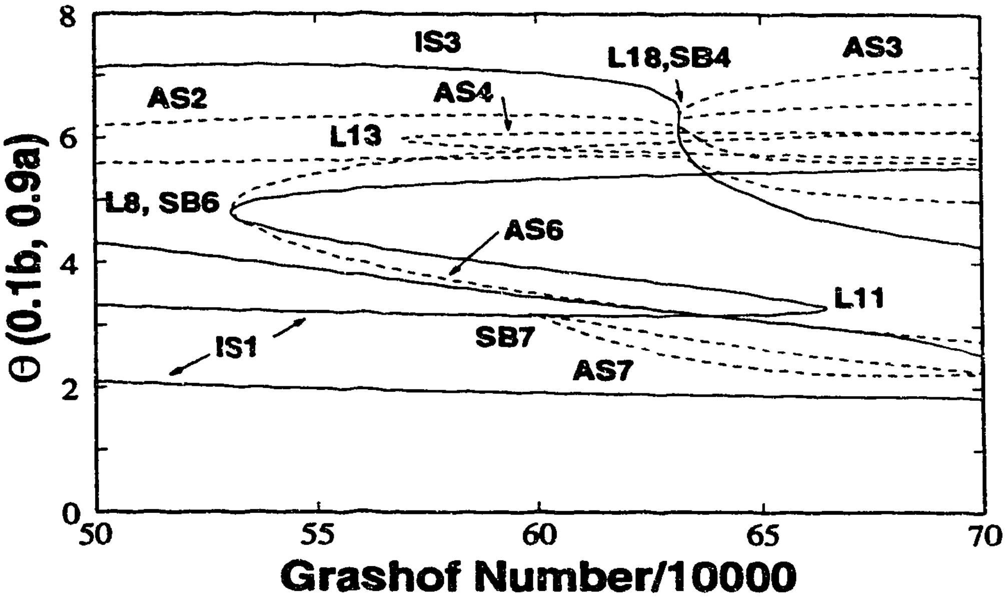

Figure 4.7: Solution Structure using Dimensioless Temperature as Parameter: High Grashof Number Region, $\phi = 0°, \gamma = 1.0, \xi = 0.000579, Pr = 7.0$

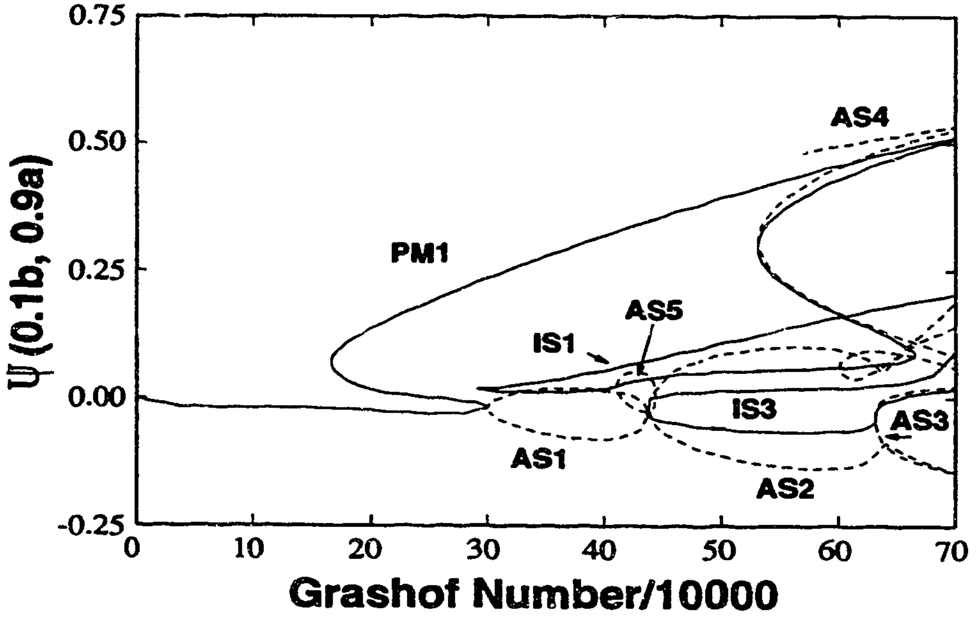

Figure 4.8: Solution Structure using Stream Function as Parameter, $\phi = 0°, \gamma = 1.0, \xi = 0.000579, Pr = 7.0$

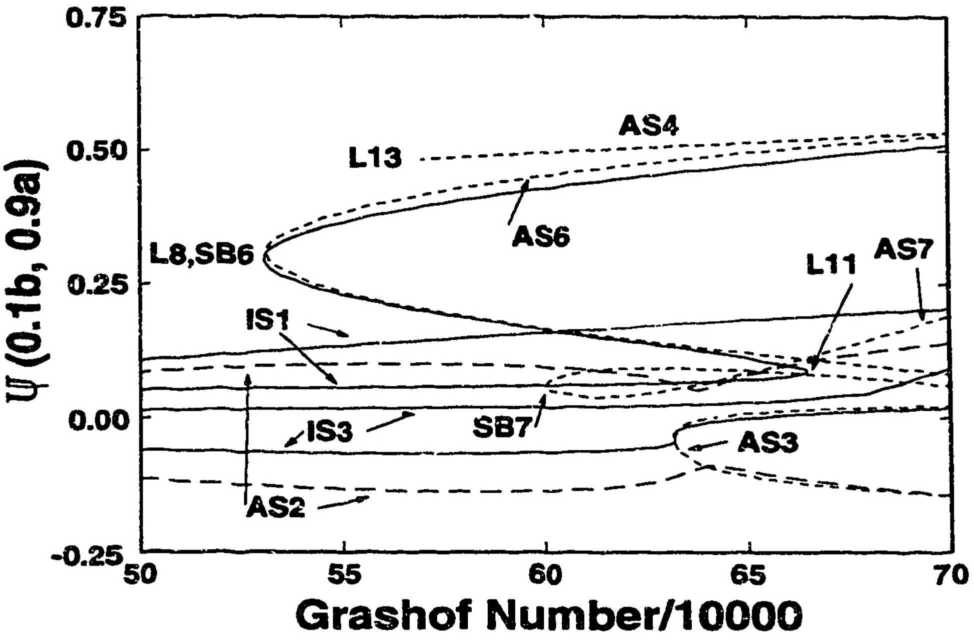

Figure 4.9: Solution Structure using Stream Function as Parameter: High Grashof Number Region, $\phi = 0°, \gamma = 1.0, \xi = 0.000579, Pr = 7.0$

4.5 Flow and Temperature Patterns

The streamlines and isotherms of all fifteen distinct solutions at a Grashof number of 700000 for an untilted layer of fluid with a unit aspect ratio are shown in Figures 4.10 and 4.11. There are an odd number of solutions due to the presence of the primary solution branch PM1. The region of PM1 from $Gr = 0$ to limit point L2 corresponds to a stable two-cell flow pattern. The upper section of PM1 has four strong flow cells. There are two hot spots in the upper corners of the system, and a cool plume is descending from the upper wall.

The lower branch of IS1 is shown to have a weaker four cell structure than does PM1, while there is a waviness in the isotherm plot, which may be indicative of a change of structure nearby. The upper branch shows the formation of two small flow cells at the upper boundary of the system. The isotherms exhibit a behavior similar to the isotherms of PM1. It should be noted that although there is a significant difference in the streamlines and isotherms at each end of branch IS1, the Nusselt numbers are almost identical.

In the case of IS3, the lower branch shows only two flow cells and no unusual behavior in the isotherm plot. The upper branch show the beginnings of secondary cell formation along the upper boundary. The waviness of the isotherms near the upper wall also indicate that some change in flow pattern is taking place.

The reflective symmetry of a pair of asymmetric solutions is evident by obsevation of the streamlines and isotherms of AS2 and AS3. The asymmetry in the isotherm plots is very subtle, but can be observed by inspection of the spacing of isotherms in the upper corners of the system. The asymmetry is more pronounced in AS2 than AS3, but is not large in either case. It is evident why these solution branches are in such close proximity at $Gr = 700000$. Observation of a point near

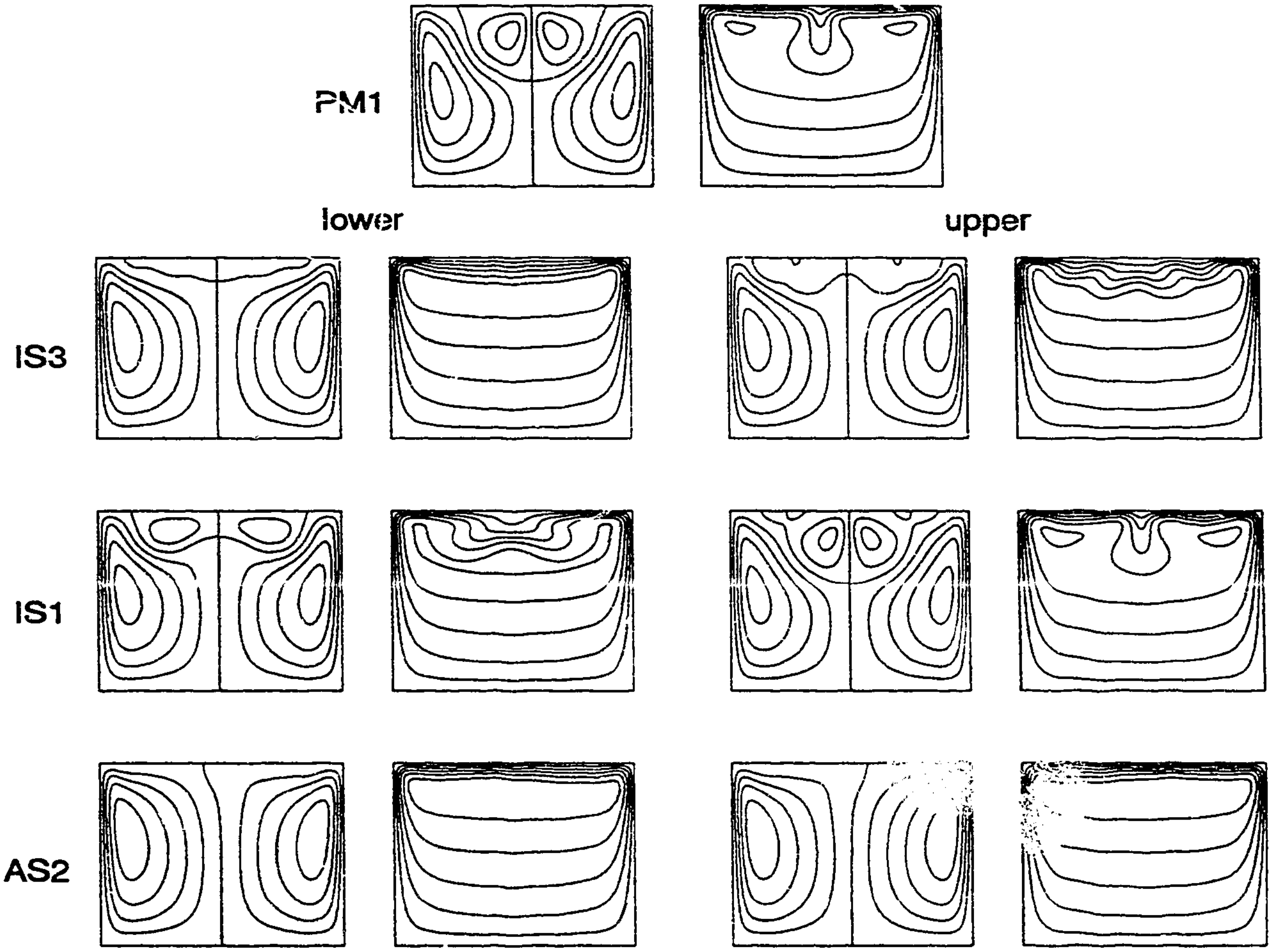

Figure 4.10: Streamlines and Isotherms for Solutions, $\phi = 0°, \gamma = 1.0, \xi = 0.000579, Pr = 7.0, Gr = 700000$

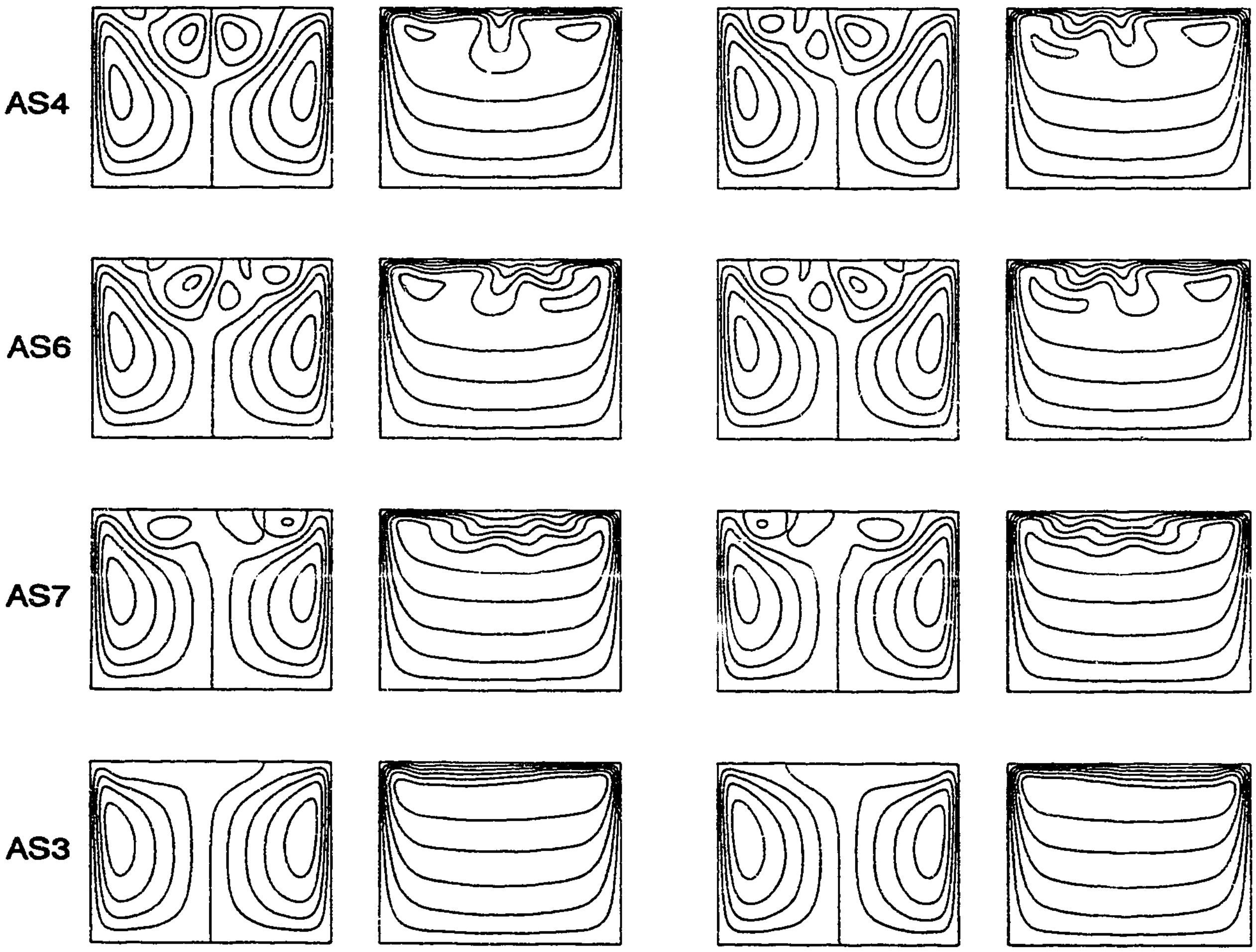

Figure 4.11: Streamlines and Isotherms for Solutions, $\phi = 0°, \gamma = 1.0, \xi = 0.000579, Pr = 7.0, Gr = 700000$ (continued)

the centreline of the system just below the upper wall in each pair of solutions shows the rationale behind choosing streamlines and isotherms at this point to illustrate the differences in solution branches.

Asymmetric solution branches AS6 and AS7 exhibit much more complex flow patterns than the other asymmetric solutions. Both have large primary flow cells, one well defined secondary cell and another secondary flow cell on the verge of development.

The pair of asymmetric solutions of branch AS4 do not exhibit the reflective symmetry that the other asymmetric solution pairs do. This branch should have a related branch with the same limit point and the two solution branches which are mirror images of the contour plots shown in Figure 4.11. However, this other asymmetric branch could not be located. One section of AS4 has a four cell flow established and a fifth cell starting to form in the upper left. At the other end of branch AS4, it is the fourth flow cell that is under development.

4.6 Stability of Solution Branches

The importance of a stability analysis in a bifurcation study and the method used to determine stability were outlined when the solution stability for the porous slab was discussed. A summary of the stability characteristics of various solution branches at several Grashof numbers within the domain are given in Tables 4.5 and 4.6.

Passing a bifurcation point along a solution path corresponds to an eigenvalue of the solution passing from the realm of stability to the realm of instability. Consider the behaviour of branch PM1. The lowest section of PM1 is stable, as it begins as a unique solution. When the limit point L2 is passed, an eigenvalue which

Grashof Number = 100000			
Branch	**Flow Pattern**	**Eigenvalue**	**Stability**
PM1	2 cell	0.97857	stable
Grashof Number = 200000			
PM1 low	2 cell	0.986866	stable
PM1 mid	2 cell	1.00829	unstable
PM1 high	4 cell	0.981628	stable
Grashof Number = 400000			
AS1	2 cell	1.021	unstable
IS1 low	weak 4 cell	1.363±i0.2928	unstable
IS1 high	weak 4 cell	1.327±i0.0558	unstable
PM1	4 cell	0.967±i0.0192	stable
Grashof Number = 500000			
IS3 low	2 cell	1.017±i0.0624	unstable

Table 4.5: Stability of Hele-Shaw Cell at Various Grashof Numbers, $\phi = 0^\circ, \gamma = 1.0, \xi = 0.000579, Pr = 7.0$. Maximum of 30 Iterations, Tolerance=$1.0E-5$

Grashof Number = 700000			
Branch	**Flow Pattern**	**Eigenvalue**	**Stability**
PM1	4 cell	0.9835	stable
IS1 low	4 cell	1.100	unstable
IS1 high	weak 6 cell	1.024±i0.0053	unstable
IS3 low	2 cell	1.1336	unstable
IS3 high	weak 4 cell	1.0829	unstable
AS2	2 cell	1.090±i0.0958	unstable
AS3	2 cell	1.127±i0.0571	unstable
AS6	4 cell	1.0584	unstable
AS7	weak 4 cell	1.1116	unstable
AS4 low	4 cell	1.0660	unstable
AS4 high	4 cell	1.0270	unstable

Table 4.6: Stability of the Hele-Shaw Cell at a Grashof Number of 700000, $\phi = 0^\circ, \gamma = 1.0, \xi = 0.000579, Pr = 7.0$. Maximum of 30 Iterations, Tolerance=$1.0E-5$

represents the a symmetric mode of the solution becomes positive. Thus, the solution is now unstable. Passing the symmetry-breaking point SB1 requires that another eigenvalue become positive. This second eigenvalue which becomes positive corresponds to an anti-symmetric mode of the solution. Finally, the limit point L1 is passed. The eigenvalue for the symmetric mode once again becomes negative. This still leaves one positive eigenvalue in the solution. However, the power iteration scheme used to determine stability calculated that the upper section of PM1 was stable. This implies that the upper section of branch PM1 is conditionally stable. It is stable with respect to a symmetric perturbation, but unstable if subjected to an asymmetric disturbance. Bara [104] found a similar behaviour for isothermal flow within a curved duct.

If the upper branch of PM1 can be isolated from asymmetric perturbations, it can remain stable. The result is a large region $165991.1 \leq Gr \leq 300034.0$ where two stable solutions exist.

All other branches within the solution domain are unstable with the exception of the region of IS3 between L4 and SB2, which was found to be stable.

4.7 Effect of Tilt Angle

4.7.1 Unfolding of Symmetry-Breaking Points

In order to characterize the effect changing the system parameters has on the solution structure, only the fold curves of the limit points and symmetry-breaking points will be considered. In the case of tilt, two ranges of tilt angle must be considered. The first range involves tilting the layer less than one degree above the horizontal. Over this range, several symmetry-breaking points unfold into nearby limit points. As an illustration, consider the limit points and symmetry-breaking points on either end of branch AS1. These pairs are L2-SB1 and L4-SB2, and the fold curves of the limit points are shown in Figure 4.12. As the layer is tilted, the symmetry within the solution is broken. The SB point is structurally unstable to tilt, so it unfolds into a limit point. As tilt increases, these limit points move closer together and eventually occupy the same position in parameter space. They then coalesce as a double limit point and unfold as a hysteresis point. This results in a branch rearrangement within the solution structure, as was seen in the porous slab solution structure.

The importance of this phenomenon is in its creation of oscillatory solutions. The points L2 and $L2'$ coalesce at a tilt angle of 0.0055°. Such a small angle is impossible to measure experimentally with any accuracy. However, along the fold curve of $L2'$, a B-point is located at a tilt angle of 0.0035°, as is labelled in Figure 4.12. This type of phenomenon is known as a Takens-Bogdanov singularity [101]. Following the path of these oscillatory solutions may lead to significant findings about the dynamics of this system. However, this would involve a routine which requires the solution of matrices twice the size of those needed to determine the solution structure. Therefore, the study of the dynamics of this fluid layer system will be left for future investigations. It should be noted that there is no corresponding B-point on the fold curve of $L4'$.

However, other pairs of limit and symmetry-breaking points can coalesce and have different results. Figure 4.13 shows the merging of L16 and $L16'$, which causes a change in IS1 and AS5. Here the merging of the two points occurs over a much larger range of tilt angles compared to the previous illustration. At a tilt angle of 0.36°, the two curves occupy the same position in parameter space, as compared to 0.0035° for L2 and SB1. This is due to the relatively large spacing between L16 and

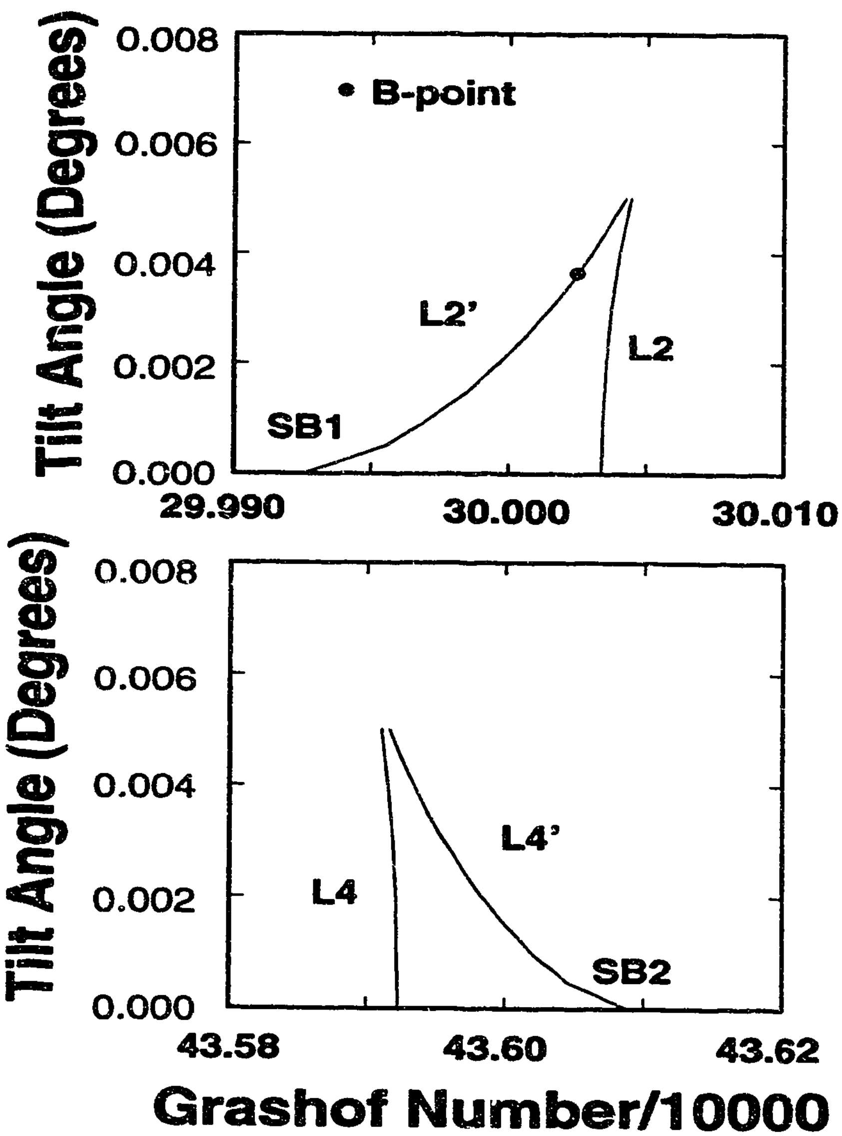

Figure 4.12: Merging of Limit and Symmetry-Breaking Points at either end of AS1, $\gamma = 1.0, \xi = 0.000579, Pr = 7.0$

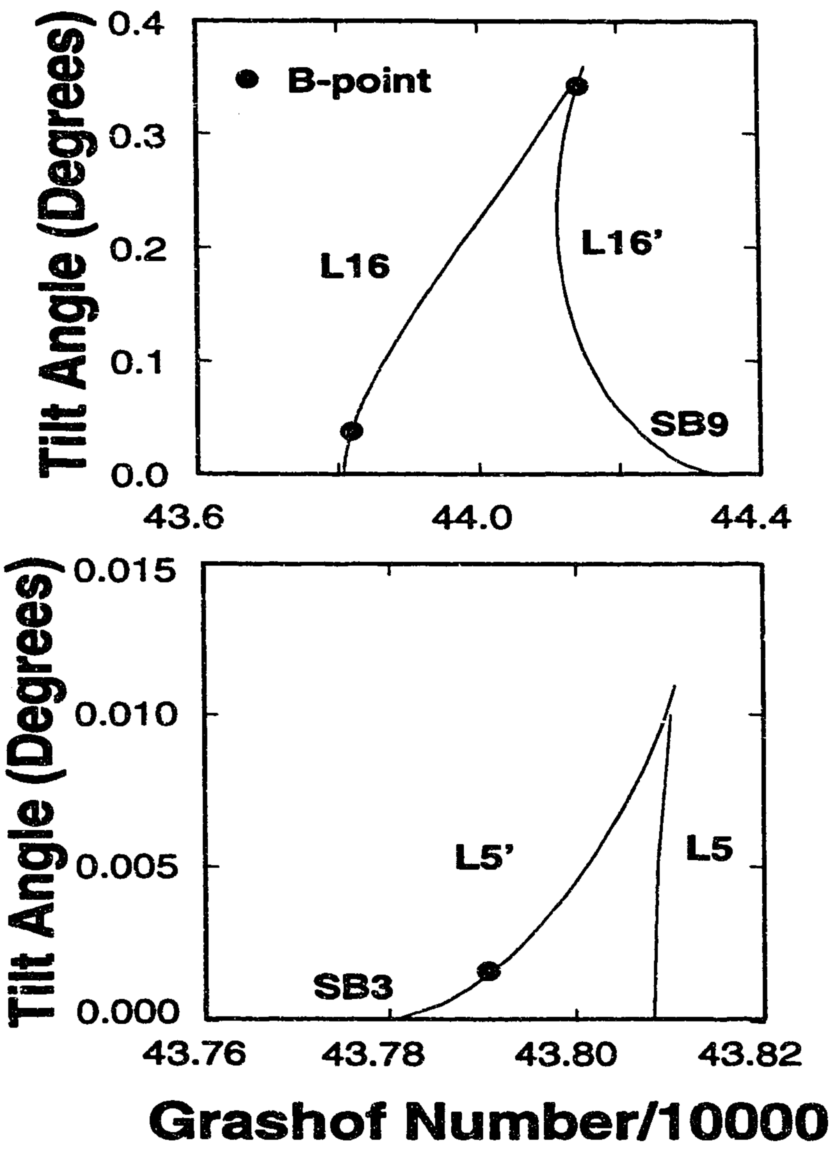

Figure 4.13: Merging of Limit and SB Points on IS3, $\gamma = 1.0, \xi = 0.000579, Pr = 7.0$

SB9 in the horizontal solution structure. Here, there are two B-points present. One is on the fold curve of L16, at a tilt angle of 0.036°, while the other is on $L16'$ at 0.35°, just before the coalescence of the two points. Also shown in Figure 4.13 is the merging of L5 and $L5'$, and the B-point located at 0.002°. The coalescence of these points is similar to that found in the unfolding of SB1 into L2.

The more interesting question deals with what happens at the other end of AS5 while L16 and $L16'$ are merging. Symmetry-breaking point SB8 is unstable to the asymmetric perturbation, and unfolds into a limit point. This causes a branch rearrangement with IS1 and AS5. The result is a continuous branch and a new isolated branch. This type of unfolding is the classical behavoiur of a pitchfork bifurcation. The limit point that exists on the new isolated solution is labelled L6 for future reference, and can be tracked as is any other limit point. The smallest value of tilt angle where L6 was found is 0.50°, while the limit point from SB8 could not be tracked beyond a tilt angle of 0.35°. A similar phenomenon occurs with SB7 on another section of IS1. The results is the formation of limit point L15.

In the case of SB6, there is a limit point nearby, but their interaction is unlike that of other combinations of limit points and SB points. It is the same type of behaviour seen with L8 and SB6 in the porous slab solution. When SB6 unfolds, there is branch switching, but the result is two limit points close to each other but unconnected. Limit point L8 continues to exist, and SB6 becomes limit point L14. This transition occurs at a tilt angle of less than 0.1°, due to the closeness of L8 and SB6.

4.7.2 Larger Tilt Angles

Several limit points are removed from the solution structure due to the unfolding of SB points and the subsequent formation of double limit points. Other SB points unfold to form limit points that remain at larger tilt angles. The fold curves of limit points that are robust with tilt are shown in Figure 4.14. The general trend of these curves is that the values of the Grashof number at the limit points increase with increasing tilt. However, there is no tilt angle where the primary solution branch is unique. In Figure 4.14, the fold curve of L1 is not asymptotic to 45° for a fluid layer with unit aspect ratio. A degree of reflective symmetry has been restored to the system, but it does not give rise to a unique solution throughout the domain.

The fact that the fold curves of L3, L8, L11, L13, L14 and L15 end suddenly is not due to any new phenomena. As the fold curves are tracked, the Grashof number increases to large values that would necessitate use of a more refined grid. Also, the fold curves tend to become almost vertical. This requires very small changes in tilt angle to continue following the curves. Following the curves beyond a certain tilt angle without decreasing the grid spacing will not give accurate results.

Several B-points were found on these fold curves, and they are labelled on Figure 4.14. These points give additional locations where interesting dynamic behaviour may be found.

4.8 Aspect Ratio

Variation of the aspect ratio of the fluid layer results in the stretching or compressing of the flow phenomena within the layer, as the relative length to height is varied. However, there are no symmetries broken. The fold curves in aspect ratio are shown in Figure 4.15. In general, the Grashof number at the limit point decreases with increasing aspect ratio. This trend is quite useful in compressing the solution structure, which moves limit points back into the parameter range considered.

The relative positioning of the limit points did not change within the solution

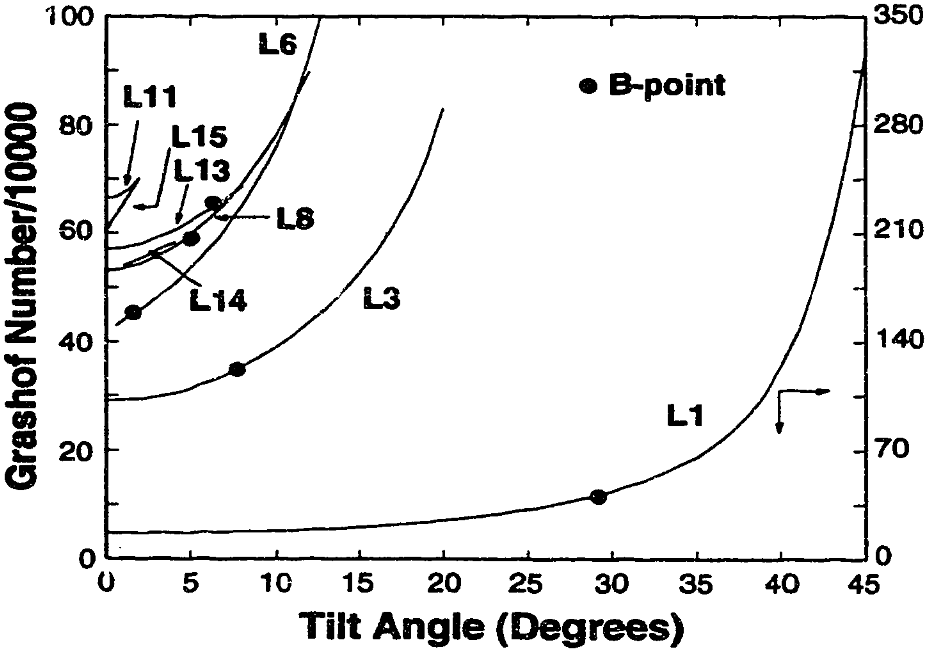

Figure 4.14: Fold Curves in Tilt Angle, $\gamma = 1.0, \xi = 0.000579, Pr = 7.0$

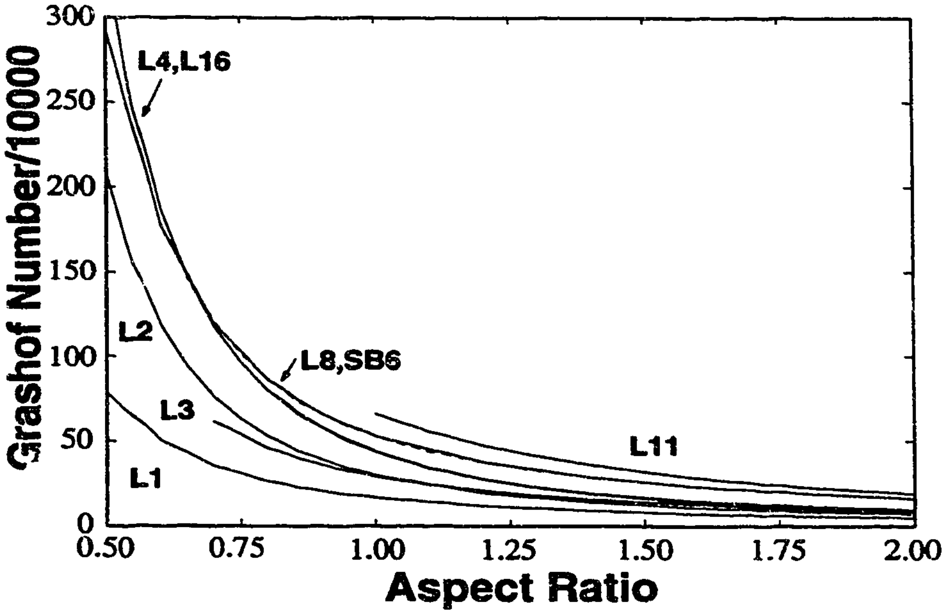

Figure 4.15: Fold Curves in Aspect Ratio, $\phi = 0°, \xi = 0.000579, Pr = 7.0$

structure. However, at aspect ratios below unity, it became difficult to track the fold curve of L8. It had a slope approaching infinity at $\gamma = 0.9$. It was postulated that there was a higher order bifurcation present, and attempts were made to track this fold curve further. These attempts were not successful.

At an aspect ratio of 2.0, the value of the Grashof number at the limit point appeared to level off near $Gr = 80000$. This appears to be a lower limit for the Grashof number of a limit point.

4.9 Prandtl Number

A change in Prandtl number corresponds to changing the fluid within the system. There are many possibilities for study in this area, and some work has been completed. For example, oscillatory solutions have been found in systems containing liquid metals [105]. However, it was decided to limit this study to the use of dilute aqueous solutions as a test fluid. Therefore, the Prandtl number was set 7.0.

4.10 Inertia Parameter

Variation of the inertia parameter results in determining the effects of the width of the gap relative to the vertical dimension of the fluid layer. This parameter turns out to be very important in linking the results of the Hele-Shaw cell solution with the solution structure of a porous slab with similar geometry. This link, and the reasoning behind it, are the next topic for discussion.

Chapter 5

Compare Porous and Fluid Layer Solutions

Now that the stationary solution structure of the heat transfer phenomena in both the porous layer and the Hele-Shaw cell have been fully described, a comparison of the two is in order. If the two solution structures are placed side by side, as is done in Figures 5.1 and 5.2, there are definite similarities between the two complicated structures. The relative positions of the limit points appear to be similar, with a few minor exceptions. The biggest difference appears to be the fact that in the porous layer there is only one isolated symmetric branch of solutions in the middle of the range studied, while the Hele-Shaw cell has two isolated symmetric solution branches in this range connected by an asymmetric solution branch.

5.1 Development of Equivalence

In order to compare the two solutions, a comparison of the two mathematical models and their parameters is needed. The model equations for the porous layer

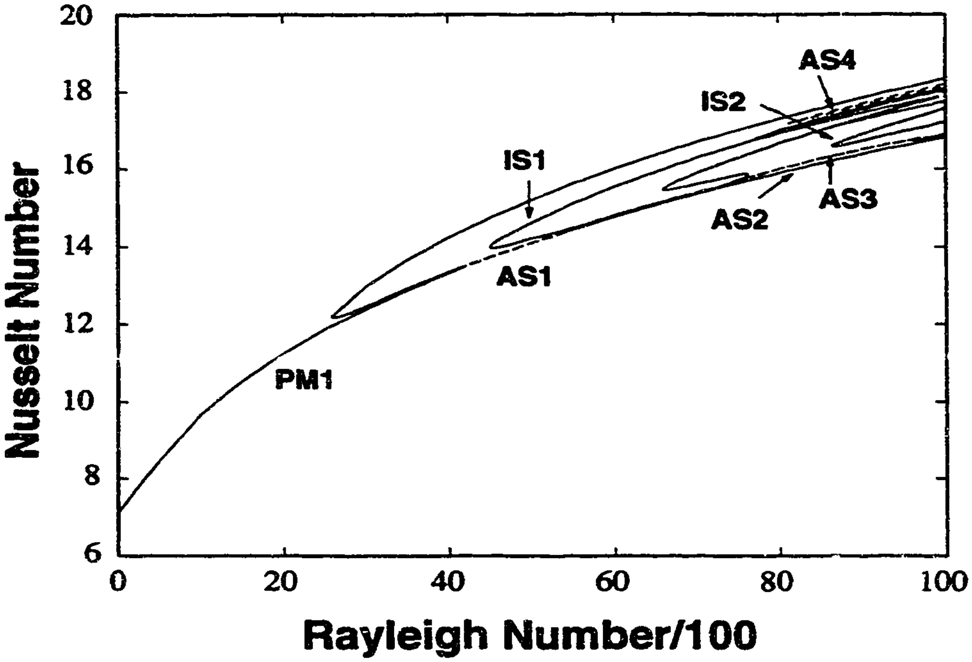

Figure 5.1: Stationary Solutions of a Thin Porous Slab, $\phi = 0°, \gamma = 1.0$

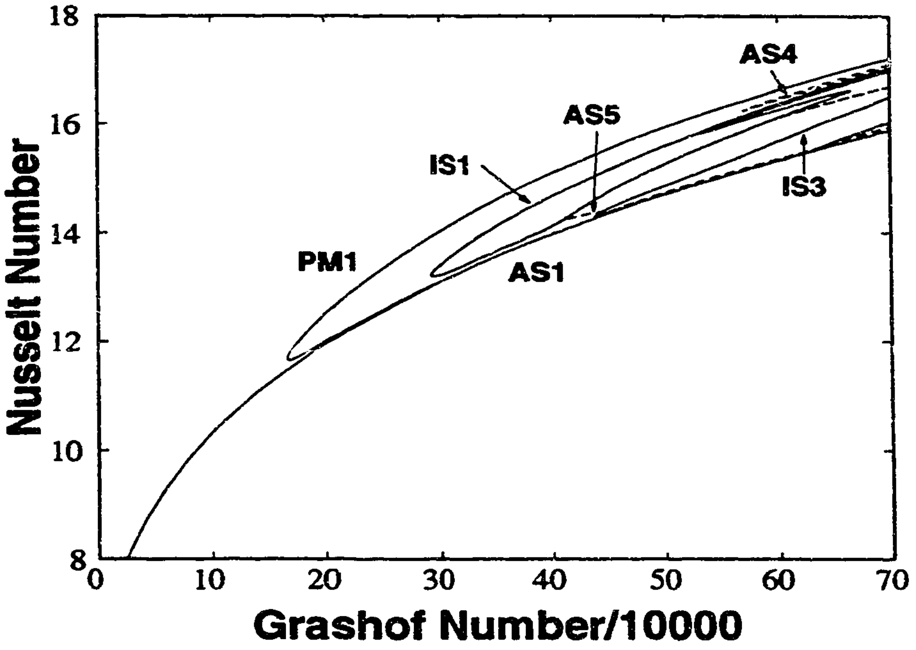

Figure 5.2: Stationary Solutions of a Hele-Shaw Cell, $\phi = 0°, \gamma = 1.0, \xi = 0.000579, Pr = 7.0$

are:

$$\Delta_\gamma\theta - \gamma[\psi,\theta] + \gamma/4 = 0 \tag{5.1}$$

$$\Delta_\gamma\psi - Ra\gamma(\theta_x \cos\phi - \gamma\theta_y \sin\phi) = 0 \tag{5.2}$$

$$Ra = (Kg\beta Q_g Ab)/(k\alpha\nu) \tag{5.3}$$

It should be noted here that the Rayleigh number defined here has a Prandtl number μ/α incorporated into it. For the Hele-Shaw cell, the equations used for modelling are:

$$\frac{1}{Pr}\Delta^H_\gamma\theta - \frac{1}{\gamma}[\psi,\theta] + \frac{1}{Pr} = 0 \tag{5.4}$$

$$\Delta^H_\gamma\Omega - \frac{6}{5\gamma}[\psi,\Omega] + Gr(\frac{1}{\gamma}\theta_x \cos\phi - \theta_y \sin\phi) - \frac{1}{\xi}\Omega = 0 \tag{5.5}$$

$$\Delta^H_\gamma\psi + \Omega = 0 \tag{5.6}$$

$$Gr = (g\beta Q_g a^5)/(k\nu^2) \tag{5.7}$$

In the scaling of this model, the Prandtl number was left separate.

There is no parameter within the model for the porous slab that corresponds with the inertia parameter ξ, as this parameter incorporates the width in the thin fluid layer. Consider the limiting case where $\xi \to 0$. Assume that the product $Gr\xi$ is a constant. Then if $\xi \to 0$, then $Gr \to \infty$. If Equation 5.5 is multiplied by ξ and then the $\lim_{\xi\to 0}$ is taken, the result is:

$$\Omega = Gr\xi(\frac{1}{\gamma}\theta_x \cos\phi - \theta_y \sin\phi)$$

Substitute into Equation 5.6 and obtain:

$$\Delta^H_\gamma\psi + Gr\xi(\frac{1}{\gamma}\theta^H_x \cos\phi - \theta^H_y \sin\phi) = 0 \tag{5.8}$$

The superscripts H and P are used to designate quantities for the Hele-Shaw cell and porous solutions respectively while this comparison is being derived. This equation is similar to Equation 5.2 from the porous model. There are differences in the scaling of temperature within the two models that must be accounted for.

$$\theta^H = \frac{T - T_w}{Q_g a^2/k} \qquad \theta^P = \frac{T_w - T}{Q_g A/k}$$

$$\theta^H = \frac{-(T_w - T)}{Q_g 4ab/k}\frac{4ab}{a^2} = -\theta^P \frac{4ab}{a^2}$$

Now consider an untilted layer of unit aspect ratio for both cases. For Equation 5.8, the result is:

$$\Delta_\gamma^H \psi + Gr\xi\theta_x^H = 0$$

Using the temperature scaling in the porous model, the equation becomes:

$$\Delta_\gamma^P \psi^P - 4Gr\xi\theta_x^P = 0$$

The porous expression for the equivalent porous slab was:

$$\Delta_\gamma^P \psi^P - Ra\theta_x^P = 0$$

It must be remembered that the scaling of the two dynamic parameters was different. For the porous model, the Prandtl number has been incorporated into the Rayleigh number, while the Hele-Shaw cell had left these parameters separate. Therefore, we must multiply the expression from the Hele-Shaw cell by $Pr = \nu/\alpha$. If the two expressions of dynamic parameter are broken down and compared:

$$Ra = \frac{d^2}{12}\frac{4g\beta Q_g a^2}{k\alpha\nu} = \frac{4g\beta Q_g a^5}{k\nu^2}\frac{d^2}{12a^2}\frac{\nu}{\alpha} = 4Gr\xi Pr$$

The expressions contain the same components. Thus, the correct equation for the equivalence is:

$$Ra = 4 * Gr * \xi * Pr$$

Therefore, as $\xi \to 0$ in the Hele-Shaw cell, the value of the expression $4 * Gr * \xi * Pr$ should approach the value of Ra in the corresponding bifurcation point in the porous solution. Confirmation of this type would provide quantitative equivalence between the two solution structures. The selection of the parameter range of Grashof number to be studied for the Hele-Shaw simulations was determined with Equation 5.1. For the porous layer, the highest value of dynamic parameter considered was $Ra = 10000$. The corresponding value for the Grashof number in the Hele-Shaw cell was

$$Gr = \frac{Ra}{4\xi Pr} = \frac{10000}{4 * 7.0 * 0.000579} = 616827$$

Thus, the maximum Grashof number of 700000 was a reasonable choice.

5.2 Similarities in the Solutions

5.2.1 Overall Solution Structure

Consideration of the graphs using dimensionless temperature as state variable are very useful in determining the strength of the analogy at points other than limit points. The porous layer graph is shown as Figure 5.3, with its fluid layer counterpart in Figure 5.4. In each case, the selected point where dimensionless temperature was obtained is in the region where secondary flow cells would develop. The difference in scaling of temperature explains the difference in the point selected for each model.

The similarity in shape between PM1 in both structures is striking. The relative shapes of AS1, AS2 and AS3 are the same, but are compressed in the porous layer as compared to the Hele-Shaw cell. Similar attachments between L8 and SB6 are present. The solution branches of AS7 are very similar as well. Thus, it can be stated that there is a great deal of qualitative correspondence in the details of the solution structures of the porous slab and thin fluid layer.

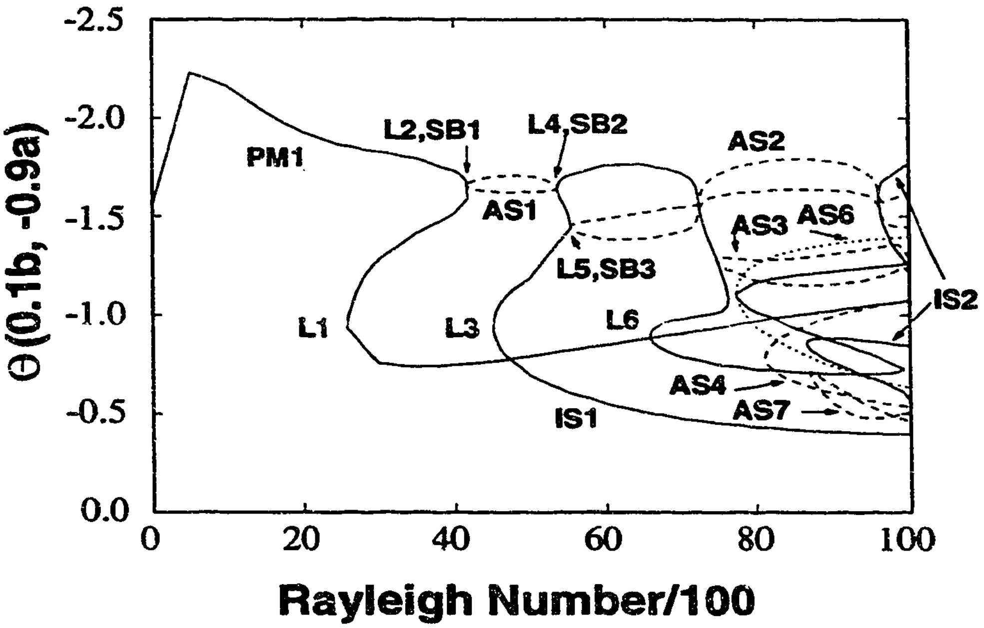

Figure 5.3: State Diagram for a Porous Layer using Dimensionless Temperature as State Variable, $\phi = 0°, \gamma = 1.0$

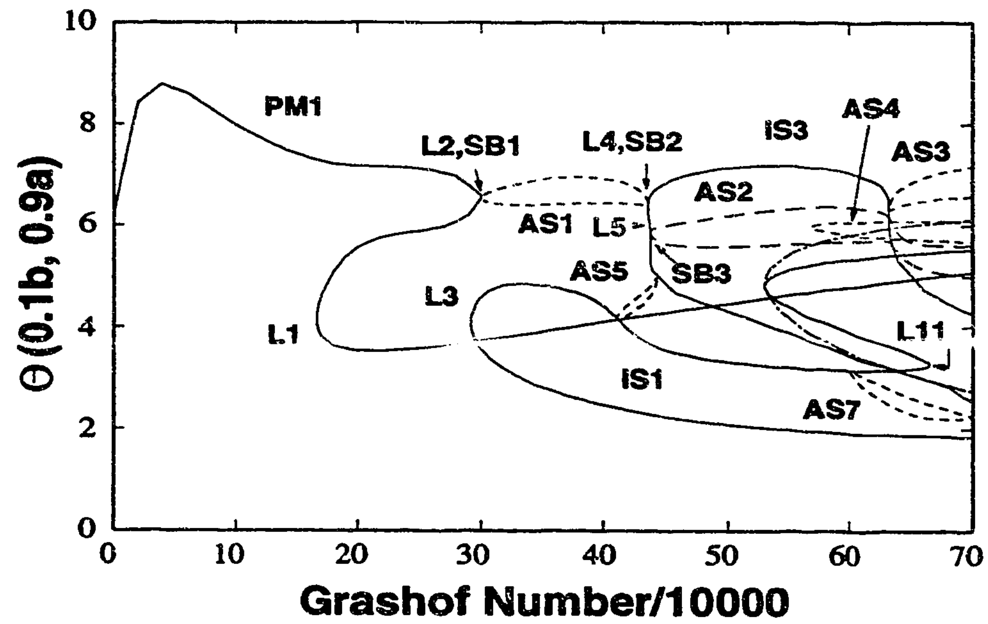

Figure 5.4: State Diagram for a Hele-Shaw cell using Dimensionless Temperature as State Variable, $' = 0^\circ, \gamma = 1.0, \xi = 0.000579, Pr = 7.0$

5.2.2 Limit Points and Symmetry-Breaking Points

It is impossible to deal with a system that has $\xi = 0$, as this corresponds to a fluid layer with no thickness. Therefore, a small, non-zero value of ξ must be chosen as a target. Following the solution paths at various values of ξ would be very time consuming. However, in the same way that the fold curves of limit points and SB points could be followed in tilt angle and aspect ratio, the fold curve of limit points in inertia parameter can be traced. These are characteristic points within the solution structure, so their correspondence would be most important in any case.

The fold curves in ξ are shown in Figure 5.5. The end points on the right of the fold curves correspond to the value of inertia parameter in the experimental system. The ξ value of $2.9E-5$ was deemed to be sufficiently close to zero. The fold curve in ξ would thus be traced over an order of magnitude. Note that fold curves of all limit points discovered in the Hele-Shaw cell solution approach limit points within the porous slab. The limit points within the porous slab solution are indicated with open circles in Figure 5.5 at $\xi = 0$. Symmetry-breaking points were more difficult to follow while ξ was varied, as solutions for SB points tended to converge very slowly. For this reason, only a few SB points were followed.

It is interesting to note that there was correspondence between the limit points L2 and L3 in both structures. This occurred despite the fact that the fold curves of these two limit points in ξ crossed. This implies that L2 occurs at a higher value of dynamic parameter in the Hele-Shaw cell than in the porous slab.

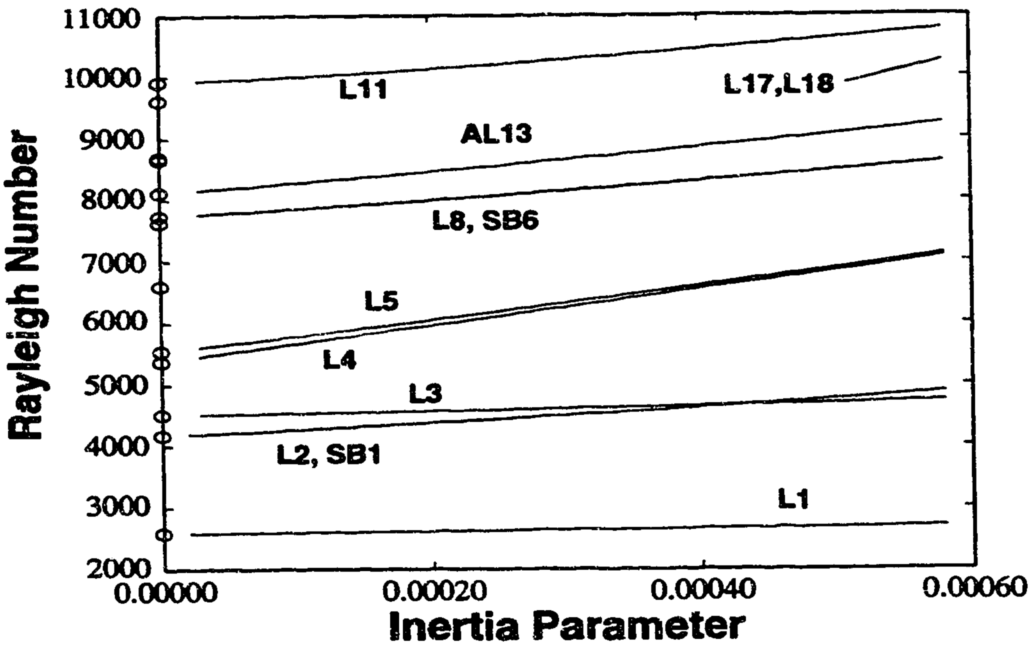

Figure 5.5: Fold Curves in Inertia Parameter, $\gamma = 1.0, \phi = 0°, Pr = 7.0$. The circles at $\xi = 0$ are the positions of limit points in the structure of the thin porous layer

5.3 Differences in Solution Structures

5.3.1 Limit Points L6 and L7

There are still great differences in the two solutions. An interesting situation is observed for the limit points L3 through L7. In the porous layer structure, these points all lie on the isolated branch IS1. However, in the fluid layer, there were two isolated branches IS1 and IS3, connected by the asymmetric branch AS5. Branch IS1 contained L3, but L4 and L5 were on IS3, with L6 and L7 not readily apparent in the fluid layer structure. Even though L3, L4 and L5 were on different branches in the structure of the fluid layer, they still approached values of limit points in the porous layer structure, where they all lay on one branch. This indicates that there is a significant rearrangement of branches as the inertia parameter is decreased toward zero, through higher order singularities.

The difference in structure between porous and fluid layers can be partially resolved by considering the region around AS5 in the fluid layer solution. The symmetry breaking point SB8 has been shown to unfold and become the missing limit point L6 as the cell is tilted. In order to determine if the point L6 in the Hele-Shaw solution did in fact correspond to the L6 in the porous slab, the positions at a tilt of one degree were used. Extrapolation to $\xi = 3.49E-4$ was possible, and the values for Ra in both cases were comparable. The results of this test are given in Table 5.1. This shows that the L6 in the fluid layer solution is in fact analogous to L6 in the porous slab. However, it exists as a SB point in a horizontal fluid layer. It is possible that the fold curve in ξ could not be extended further toward zero due to some higher order phenomenon that results in the change from SB8 to L6.

The presence of L7 in the fluid layer structure is less clear. The asymmetric branches AS3 in each structure have a similar appearance when the stream function

Hele-Shaw Cell		
Grashof Number	**Inertia Parameter**	$Ra = 4 * Gr * \xi * Pr$
439994.1	0.000579	7133.18
657715.9	0.000349	6611.36
Porous Slab		
	(0.00000)	6594.95

Table 5.1: Fold Curve in ξ for L6 in Hele-Shaw Cell, $\phi = 1°, \gamma = 1.0, Pr = 7.0$

and temperature graphs are considered, but there is a severe discrepancy in the values of the dynamic parameter. Also, there is no limit point on IS3 to match with L7, except for the limit point L18 near the edge of the domain. However, there was no numerical evidence found to support this speculated analogy.

5.3.2 Branch IS2 and Limit Points L9 and L10

There is no analogous limit point to match with L9 in the porous structure. The presence of L17 on IS3 appeared to be a match for L9. However, when the fold curve for ξ was computed, it was found to merge with the fold curve of L18 at $\xi = 0.000479$. These two limit points then collapse into each other and disappear. This leaves only the symmetry breaking point SB10, which is left by itself when L17 and L18 collapse. Since no analogue for IS2 could be found in the Hele-Shaw cell, it was impossible to follow the curve to find limit point L10. Extension of AS3, which originates at SB4, showed no sign of turning around as well, and thus gave no clues about this region.

5.4 Presence of AL13

In both cases, a mysterious branch of solutions appeared, and both were labelled AL13. Each solution is asymmetric, yet does not emanate from any symmetric solution branch located. Since an asymmetric branch must originate from a symmetric branch, there must be a symmetric branch outside the studied domain that was not located. These branches must occur as a pair of mirror-imaged asymmetric solutions, but the other branch in the pair was not located. More intriguing is the fact that in both cases the limit point L13 is in some way related to L8. They appear to be on different levels of a fold in the solution plane. In both cases, they were discovered by starting at L8, then varying the tilt angle and aspect ratio in a circular path and returning to the parameter set of origin. In the porous layer, this technique was required to circumvent a discontinuity in the fold curve. However, no such discontinuity exists in the fluid layer solution. Thus, the discontinuity appears to have nothing to do with the presence of this branch.

The most curious aspect of the presence of AL13 is that it is an asymmetric branch which appears to be connected to L8 through some type of bifurcation within the solution plane. No other work has presented an asymmetric solution connected to a symmetric solution through a higher order bifurcation. This asymmetric branch does not appear to be connected to another discovered solution branch in any manner. It is a most interesting phenomenon, and should be considered further in any future work with either a porous slab or a Hele-Shaw cell.

5.5 Comparison of the Behavior with Tilt

5.5.1 Unfolding of Symmetry-Breaking Points into Limit Points

In both cases, SB points unfolded into limit points at very small tilt angles. In the Hele-Shaw cells, the merging of these points took place at larger tilt angles, although for practical purposes the differences are insignificant. For the case of the merging of L2 and SB1, the porous layer coalescing occurred at 0.0038°, while in the fluid layer it occurred at an angle of 0.0054°. The larger magnitudes of the dynamic parameter in the fluid layer causes a greater distance between the two points in the solution space. Since the value of the dynamic parameter at the limit point varies slightly with tilt at small angles, the symmetry-breaking point must move a longer way to coalesce in the fluid layer structure.

There was no B-point found on the fold curve of SB2 in the Hele-Shaw cell, while there was a B-point on the corresponding curve in the porous slab. However, there was a B-point found on the fold curve of L16, as well as on SB9, with which it coalesces. These two symmetry-breaking points are in close vicinity, but are separated by the pair L5 and SB3. The close proximity of several bifurcation points leads to complex interactions as the layer is tilted. As the inertia parameter is varied, other such interactions are possible. This is the region that should lead to the merging of IS1 and IS3 of the fluid layer structure into one symmetric branch similar to IS1 in the porous layer. However, such a change in structure appears to involve a higher order bifurcation, as the fold curve in ξ for L6 ended at $\xi = 0.000349$. Higher order phenomena cannot be explored using the methods of this study. Therefore, a separate study is required to investigate the details of the transition of the two symmetric solution branches IS1 and IS3 in the fluid layer structure into one symmetric solution branch.

5.5.2 Fold Curves at Larger Tilt Angles

There are also some similarities in the structures as the tilt angle is increased. Fold curves for both systems contain B-points at larger tilt angles. The positions of these B-points are in the same vicinity in both systems, but do not correspond exactly. Except for the fold curve of L1, the B-points exist at smaller tilt angles in the Hele-Shaw cell. The B-points exist near discontinuities in the fold curves of L6, L8 and L10 in the porous layer. There could not be discontinuities on the fold curve of L10 in the Hele-Shaw solution, as a limit point corresponding to L10 was not located. However, no such discontinuities exist in the Hele-Shaw cell, yet the B-points occur. These points give locations to begin a study of dynamic behavior within the fluid layer, but will not give any insight into the presence of the fold curve discontinuities found in the porous layer.

The discontinuities of the fold curves in the porous structure were due to changes in the flow cells near the edge of the cell, which could lead to the development of more flow cells. Since the formation of more flow cells within the system was the manner in which bifurcations affect the system, it is not surprising that B-points were present near these discontinuities. Lack of discontinuity in the fluid layer indicates that these discontinuities are due to phenomena which affect a porous slab that do not occur in a thin fluid layer.

5.6 Stability

In both cases, the majority of the solution branches were found to be unstable at the highest value of dynamic parameter considered. The variation in stability of the Hele-Shaw cell with tilt was not considered, so only solutions at 0° may be compared.

Only one major difference exists in the stability characteristics of the two solutions. That is the fact that the upper part of PM1, which extends from limit point L1 to the end of the domain of interest, is unstable in the porous layer but is conditionally stable in the fluid layer. For both cases, the lower part of PM1, from the zero value of dynamic parameter to limit point L2, is stable. This creates a large region within the Hele-Shaw cell where there may exist two stable solutions for a given parameter set. This behaviour is considered in the experimental portion of this dissertation, which is discussed extensively in the next chapter.

5.7 What Does It All Mean?

The correspondence that has been found between the bifurcation diagrams for the thin porous slab and the Hele-Shaw cell is sufficient to state that there is a strong relationship in the bifurcation behavior of the two systems. This relationship has both a qualitative and quantitative basis. Any structure found in experiments with a thin fluid gap will have a corresponding structure in a thin porous layer. The connections of this structure to other parts of the solution may be different, but these connections may be predicted by analogy. This justifies the use of a fluid layer as a substitute for a porous slab when looking for bifurcations at steady state.

Chapter 6

Experimental Procedure and Results

The experimental portion of this study considers natural convective flow within a vertical Hele-Shaw cell, where the flow is driven by internal heat sources. One objective of the experimental study is to determine if the section of solution branch PM1, which contains a four-cell flow pattern, is stable. Numerical simulation has determined that this branch is conditionally stable. Any asymmetric perturbation will cause instability in this solution branch. If all asymmetric perturbations can be suppressed, then a set of parameters where two stable solutions exist can be investigated. Flow visualization is used to observe the flow patterns that do exist within the Hele-Shaw cell.

6.1 Previous Experimental Studies

Early experimental investigations considered fluid layers where the thin gap was parallel with a table top. The small dimension in the direction of gravity yielded a very small flow parameter, as the usual scaling of equations resulted in the flow parameter containing the cube of the vertical dimension. Initial studies dealt with fluid layers heated from below. A thin layer enabled the critical value of flow parameter to be surpassed with a relatively small heat input, and thus a small temperature gradient. The primary focus of these early studies was determination of this critical value for the onset of convection.

A typical apparatus consisted of transparent plexiglas containing walls on the sides of the cell. These side walls were considered to be adiabatic surfaces. The lower surface was a copper plate with the heating provided in one of two manners. Either an electric heater was implanted into the plate to act as a constant flux source, or a constant temperature was maintained by passing fluid through channels within the plate. Above the test layer would sit another copper plate equipped with cooling water channels. The test fluid within the cell was a fluid with well known physical and thermal properties. Common test fluids were water and mineral oils. The transparent walls enabled flow visualization to be performed with the aid of dyes or coloured particles. Interferometry was often used to obtain temperature data from within the cell.

Other investigators were interested in the behavior of a fluid layer where the convection was driven by internal heat sources. These systems usually had the upper boundary held at a constant temperature with cooling water, while the remaining boundaries were adiabatic. Again, the vertical dimension was kept small to prevent the dynamic parameter from attaining large values. For example, in the study of Tritton and Zarraga [16], the lateral walls formed a square of $29cm$ in length, and the vertical dimension chosen was $0.44cm$. The Rayleigh number used in this study contained the depth of the fluid layer to the fifth power. A thin layer was thus required in order to obtain reasonable Rayleigh numbers with moderate heat inputs.

6.2 Design Criteria

In the present study, the geometry of the system is slightly different. One difference is that a vertical Hele-Shaw cell is subjected to heating by internal heat sources, as opposed to heating from below. Another is that the layer is intended to be finite in dimension, with a length to height aspect ratio of unity. The entire periphery of the cell is held at a constant temperature. This combination of thermal boundary conditions and internal heating in a fluid layer has not been reported in the literature.

The basis of the apparatus is a $3/4in$ copper block. A schematic of the block is given in Figure 6.1. Copper was the most suitable material for the block due to its high thermal conductivity and successful use in previous studies. A thick block was selected to facilitate construction.

A rectangular piece was cut out of the centre of the copper block. This new inner chamber forms the test region. Eight holes were drilled to within $1/8in$ of the interior surfaces in order to house thermocouples. The holes were placed asymmetrically with respect to the centreline of the test region in order to detect the presence of parabolic or periodic temperature profiles along the test cell walls. Each thermocouple housing was capped with a Swagelock fitting and rubber ferule in order to hold the thermocouple in place.

Six other holes were drilled through to the interior surfaces of the block. Two of these penetrated the top wall of the test cell to serve as fill holes and to allow for fluid expansion upon heating. The four remaining holes, two in each interior

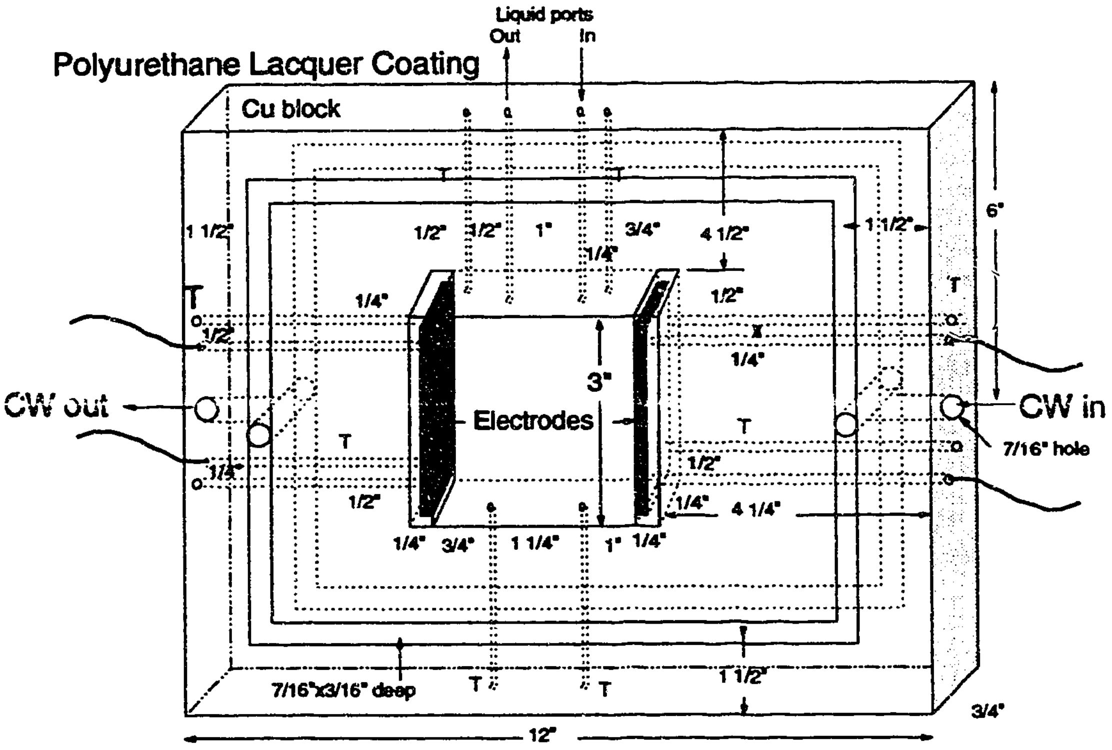

Figure 6.1: Copper Block used in Experimental Apparatus. Dimensions are as shown

side wall, serve as holes for the wires that leads to the electrodes. These electrodes supply the alternating current to the fluid layer which is the source for the heating.

A cooling water path was also cut into the block. Holes were drilled into the block at each end to serve as entrance and exit for the cooling water. These holes were each equipped with a fitting to allow a hose to be attached to each end of the cooling water path. Rectangular grooves were cut above and below the test region on either side of the block to carry the cooling water past the upper and lower surfaces. Several holes were also drilled into the face of the copper block in order to bolt the three pieces of the apparatus together.

The block was polished with fine sandpaper in order to remove imperfections in the inner surfaces, and to clean all surfaces that could come in contact with the test fluid.

In order to create a thin gap within the thick block, special plexiglas containing walls were constructed. A sheet of plexiglas was machined to the dimensions shown in Figure 6.2. The lip is sized to fit snugly inside the hole within the copper block. Garlock paper gaskets were used to seal the interface between the copper block and the plexiglas sheet. Dow Corning silicon stopcock sealant was used to prevent leaks of the test fluid through the wire holes in the copper block and around the edges of the plexiglas lip that protrudes into the copper block. Several holes were also drilled in these plexiglas walls to allow them to be fastened to the copper block.

The assembly of the copper block and two plexiglas sheets required 60 bolts for each plexiglas wall. The large number of bolts was necessary in order to prevent leaks of the test fluid and cooling water. With the two plexiglas sheets attached to the copper block, a thin gap remains in the centre region of the copper block. This is the test region.

Specific dimensions for the cell were arrived at in the following way. A gap width

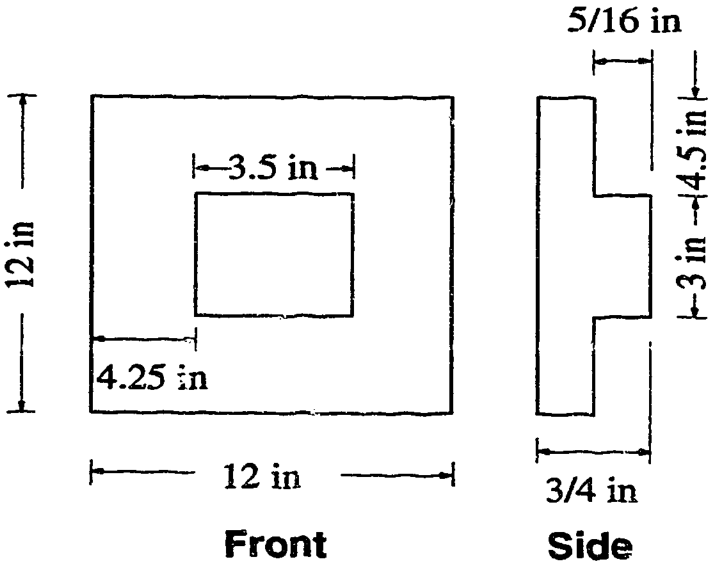

Figure 6.2: Plexiglas Walls Enclosing Test Region

of $1/8in$ was used in the work of Koster and Müller [1]. A gap of this width has commonly been used in experimental studies with fluid layers heated from below. Thus, it was selected for this cell. Koster and Müller also suggested that an aspect ratio of at least 20/1 be used for the height of the cell to the width. The selected height of the cell was $3in$, which results in a height to depth aspect ratio of 24/1. The parameter set chosen from the simulations for comparison had a unit aspect ratio of length to height. This set the length of the cell at $3in$.

The use of this type of plexiglas wall assembly facilitates the variation of gap width. A new set of walls with different lip size would give any desired gap width.

The internal heat sources were supplied through electrolytic heating. Instead of using water as the test fluid, a dilute aqueous solution of copper sulfate is the preferred choice. Most studies considering internally heated fluid layers use copper sulfate as the test fluid, as it is inexpensive and easy to obtain. A solution of five weight percent anhydrous copper sulfate in water does not significantly alter the physical properties of water, with the exception of electrical conductivity. The result is that physical properties of pure water can be substituted for those of a dilute aqueous solution without introducing significant errors.

The internal heating occurs when an alternating electric current is passed through the copper sulfate solution within the test cell. The electrodes are made of 16 gauge copper plate, and 14 gauge wire is used to provide the electric current. In addition to a high thermal conductivity, copper has a high electrical conductivity. A problem existed in that both the electrodes and the walls of the test region are both made of copper. No heating would occur within the fluid if current was allowed to leak out of the walls of the test cell.

It was decided to inhibit the electrical conductivity of the copper block. A thin layer of polyurethane lacquer [16] or Teflon [19] has been found to be effective for this purpose. A Teflon layer could easily be scratched off the block, as it is very soft. The polyurethane layer was found to be more durable, and no less effective in blocking the passage of electrical current through the block. Therefore, a polyurethane lacquer was considered more appropriate. The disadvantage of a polyurethane lacquer layer is in the difficulty of uniform application. The variation in the thickness of the lacquer layer were not significant compared to the height of the test region.

However, the electodes could not be coated, and they would be in direct contact with the walls. For this reason it was decided to mount the electrodes on thin pieces of Teflon. The $1/4in$ piece of Teflon used for this purpose did not have a significant impact on the heat removal at the side walls.

The assembled apparatus is mounted on a steel bracket with a hole cut into it to allow the test region to be seen from either side. This opening also allows light to pass through by for aid in flow visualization.

Undyed polystyrene beads $250\mu m$ in diameter were added to the fluid to make the flow visible. The particle concentration was very small, and thus did not significantly affect the properties of the fluid. An aqueous copper sulfate solution of proper density results in beads which are neutrally buoyant. Adjustment of the solution density was critical in the experiment. In the experimental runs, the fluid density would change as the solution heated up. This required that the particle density be matched with the density of the solution when warmed to the steady state temperature. Any density difference between the density of copper sulfate and the beads would lead to settling velocities of the particles which would be of the same order of magnitude as the velocity of the flow. In many cases, the particles did settle out of the solution, which necessitated a change in side wall temperature to negate the mismatch in fluid and particle density. If required, the particles are resuspended by stirring the solution with a piece of thin tubing inserted through a fill hole. A flashlight was shone behind the test region to illuminate the flow cells. Photographs were taken with a Nikon $35mm$ camera. The low light provided by the flashlight allowed an exposure time of ten seconds to be used for the photographs. Such a long exposure time allowed the particles to move a significant distance while the aperture was open. Paths that the particles travel appear as streaks on the photograph. A black velvet background was used to increase the contrast between the particles and the solution. The layout used for flow visualization is depicted in Figure 6.3.

The bracket and test cell are then mounted on a steel stand with three adjustable legs to allow for levelling. The bracket attaches to the stand with a pivot to allow the test cell to be tilted to any desired angle between 0° and 90°.

Measurements of the data associated with the cell were performed with the following instruments. A J-12 thermocouple was placed within each of the eight wells drilled into the copper block. These thermocouples were grounded at their tips. The temperatures were read using an OPTO22 data acquisition system with software produced within the Department of Chemical Engineering. Each thermocouple has an optically isolated module that sends the signal through a serial port to a Zenith XT personal computer. The thermocouples are calibrated to be accurate to within 0.1°C, but the resolution of the data acquisition system is 0.5°C. One additional thermocouple was also present. It was used to determine the temperature at one point within the fluid when the convection reached steady state.

A Fluke 77 multimeter and a Beckman Tech 310 multimeter were used to measure the current and voltage inputs, respectively, to the fluid. Two Variac regulators were used to supply the power from a wall outlet of 120 Hz, 60 cycle. The use of two regulators in series allowed fine control of the power input to the fluid within the cell. Due to the small fluid volume, a small change in the power input had a large

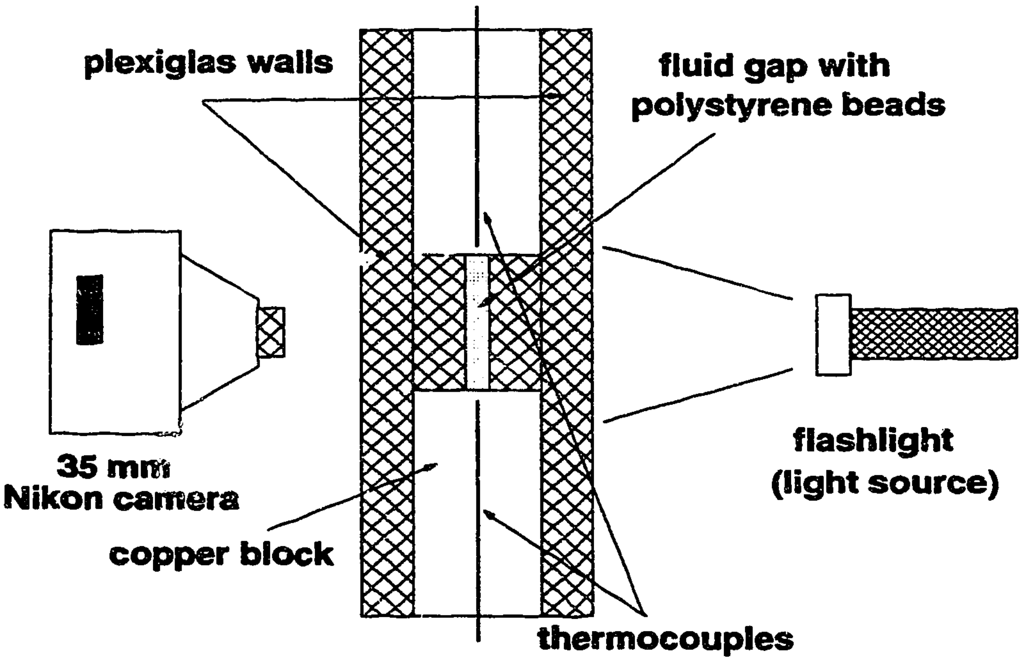

Figure 6.3: Top View of Layout for Flow Visualization

change in the value of the Grashof number. Power factors for the system were very close to unity.

The cooling water was supplied from a domestic source. The experiments were performed at night in order to limit the disturbances to the cooling water and allow the water temperature to stay fairly constant.

A sketch of the complete apparatus is given in Figure 6.4.

6.3 Experimental Procedure

The first step of the experiments was to make a new batch of copper sulfate solution. The volume of fluid within the Hele-Shaw cell was $17ml$, so only $50ml$ of solution was made at a time. A mass of 4.8 grams copper sulfate was added to 57.8 grams of distilled water. Each mass was determined using a Mettler PC 8000 balance. Tap water tended to foul the electrodes more quickly than did distilled water. The solution was stirred vigourously until all crystals had dissolved. Polystyrene beads of diameter $250\mu m$ were added in sufficient concentration to allow the fluid structures to be easily seen. The solution was injected into the cell with a syringe fitted with a 16 gauge needle. Such a large needle was required to enable the particles to enter the cell with the copper sulfate solution. All air bubbles within the fluid were removed by stirring the fluid with a piece of tubing inserted into one of the fill holes.

The test region was set to the desired value of inclination. If horizontal, a carpenter's level was used as a check. For inclined layers, the graduations on the stand were used. The cooling water was turned on and allowed to run until the eight thermocouples within the copper block all read the same temperature. The power source was then turned on, and the variacs adjusted to the desired value.

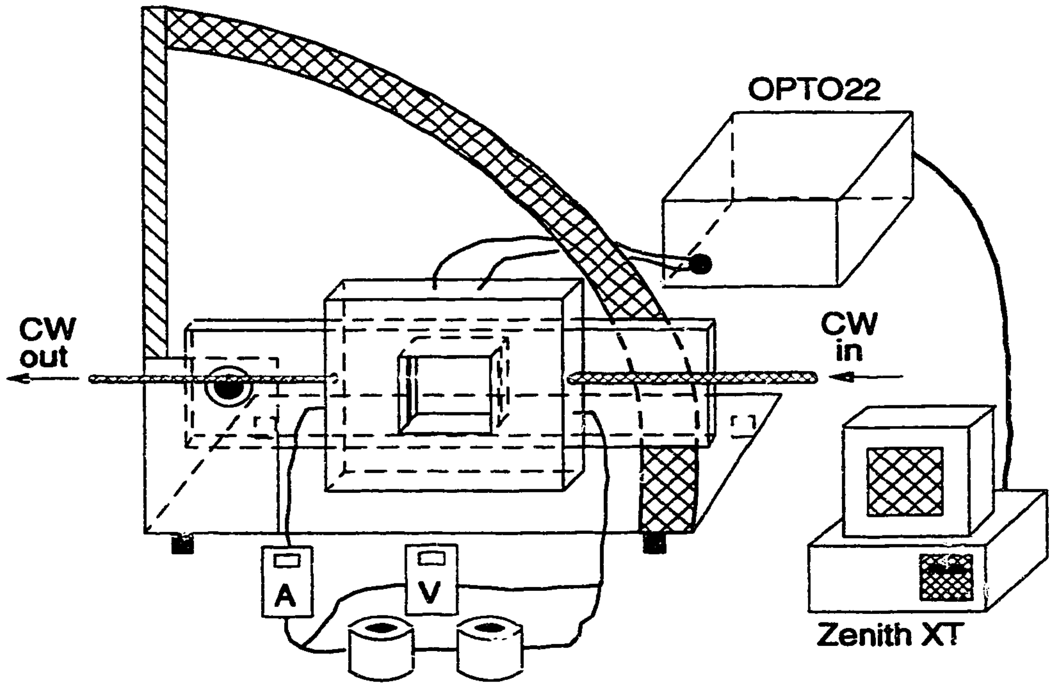

Figure 6.4: The Complete Experimental Apparatus

The initial value of the current and voltage were recorded. Electical conductivity is a strong function of temperature [19], so the current and voltage readings vary significantly as the fluid heats up. Temperature readings were taken every fifteen seconds until steady state was reached. Steady state is considered to occur when the beads within the cell were moving in a steady pattern, and that the voltage and current readings had not changed for ten minutes. At steady state, a thermocouple was placed within the fluid through the left fill hole. The temperature was read by the data acquisition system. Any observations of the convective state present were noted, as were any strange flow patterns seen during the transient evolution. The power input was then changed to the next desired level, and the process repeated.

The following steps are taken to shut down the apparatus. Both variacs were turned off and disconnected. The current and voltage meters were turned off. Cooling water was allowed to run through the system until the apparatus was cool, and was then turned off. The fluid within the cell was removed using the syringe and a tubing extension.

6.4 Uncertainties and Errors in Experiments

6.4.1 Quantified Errors

With every experimental measurement there is uncertainty. Computed quantities based on these measurements also have errors associated with them. In order to determine the error in computed values, the method outlined in Appendix A is used. This method determines a relative error based on the formula for the computed quantity. For example, Grashof number is determined using the formula:

$$Gr = Q_g \beta g a^5 / (k \nu^2)$$

and the relative error is determined using the relation:

$$\frac{\Delta Gr}{Gr} = \sqrt{(\frac{\Delta Q_g}{Q_g})^2 + (\frac{\Delta \beta}{\beta})^2 + (\frac{5\Delta a}{a})^2 + (\frac{\Delta k}{k})^2 + (\frac{2\Delta \nu}{\nu})^2}$$

The Grashof numbers calculated were found to have an error of approximately 15% associated with them. Dimensionless temperature was plotted as the other variable in order to find the region of dual solutions. The error in θ was in the range of $30 - 40\%$, depending on the value of the temperature of the copper walls. This error was largely due to the uncertainty in the measured temperatures.

6.4.2 Other Errors

Some errors in the system are not as easily quantified. There is some heat loss from the fluid layer through the plexiglas containing walls. Since the thermal mass of the copper block is very large compared to the thermal mass of the plexiglas pieces, the heat loss through the side walls should not be large. Most experimental runs had the apparatus at a temperature close to room temperature. Other tests used copper block temperatures which were well below room temperature. In both cases, the data collected was of good quality. Therefore, the temperature of the copper block had little effect on the quality of the data, which indicates that the heat loss from the plexiglas walls was insignificant.

The driving force supplied by electrolytic heating may not be uniform. Triton and Zarraga [16] reported up to a 10% variation in the internal heating within various regions of the fluid. This factor is very significant, as such a variation could lead to an asymmetric perturbation that would make the upper section of PM1 unstable.

The addition of the polystyrene beads to make the flow visible could have an effect on the physical properties of the copper sulfate solution. Only a very small mass of particles was added to the solution. Their easy dispersal through the fluid made the flow visible, but the amount of material added is insignificant compared to the amount of fluid.

However, the possible mismatch in the densities of the fluid and the polystyrene beads may be very significant. The presence of any density difference between fluid and solid would lead to the particles having terminal velocities of the same order of magnitude as the flows being visualized. This would have a significant effect on what was seen.

It is also difficult to quantify the amount of error in the tilt angle when the layer is untilted. A carpenter's level was used to determine if the test cell was untilted. The error associated with the air bubble and the marked lines on the level is a function of the care in the manufacturing of the level. In the simulation results, there were B-points found at tilt angles of the order of thousandths of a degree. It is impossible to determine a tilt angle to that degree of accuracy with the equipment available.

6.5 Experimental Results

6.5.1 Transient Phenomena

This study considers only steady solutions and flow patterns. However, some interesting effects were observed in the evolution toward steady flow patterns. Initially, the fluid is at rest. As the alternating current begins to pass through the fluid, downward flow begins near both electrodes. The first flow pattern which is evident contains four vertical flow cells. Continued heating causes the flow cells near the edges to grow toward the centre of the test region. The central pair of flow cells shrink toward the top center part of the fluid layer. Eventually, the large primary cells overcome the small secondary flow cells, and a two cell pattern becomes prevalent. This evolution is diagrammed in Figure 6.5. The time frame for the completion of this evolution is approximately 40 minutes.

In a few other experimental runs, a state was observed that could not come to a steady state. The fluid was heated by the copper walls as well as the electrolytic heating. The flows observed were similar to those found for bottom heated fluid layers. Primary flow cells moved upward along the edges, and secondary flow cells formed in the bottom part of the test region. As the fluid continued to heat up, it became warmer than the containing walls. At this point the flow pattern would begin to again follow the transient patterns described previously.

6.5.2 Region of Parameters Between L1 and L2

Several multiple solution regions were predicted in the simulations for the Hele-Shaw cell. However, only two had more than one stable solution branch. One was the range $435923 < Gr < 436088$, where branch IS3 is stable, and PM1 is conditionally stable. However, this range is very small, and it would be difficult to reach IS3 experimentally. The other range of multiple stable solutions is $165991 < Gr < 300034$, where the lower section of PM1 is stable, and the upper section of PM1 is conditionally stable. This region is sufficiently large to pursue experimentally. It is simple to reach one solution branch, as the lower section of PM1 is one of the stable branches encountered, and it contains the unique solution region. The upper section of PM1 was found to contain solutions with a four-cell flow pattern. There is some question as to whether this solution branch would be stable in the experimental runs, as numerical simulation predicted that it is conditionally stable. All asymmetric pertubations be removed from the experiment in order to

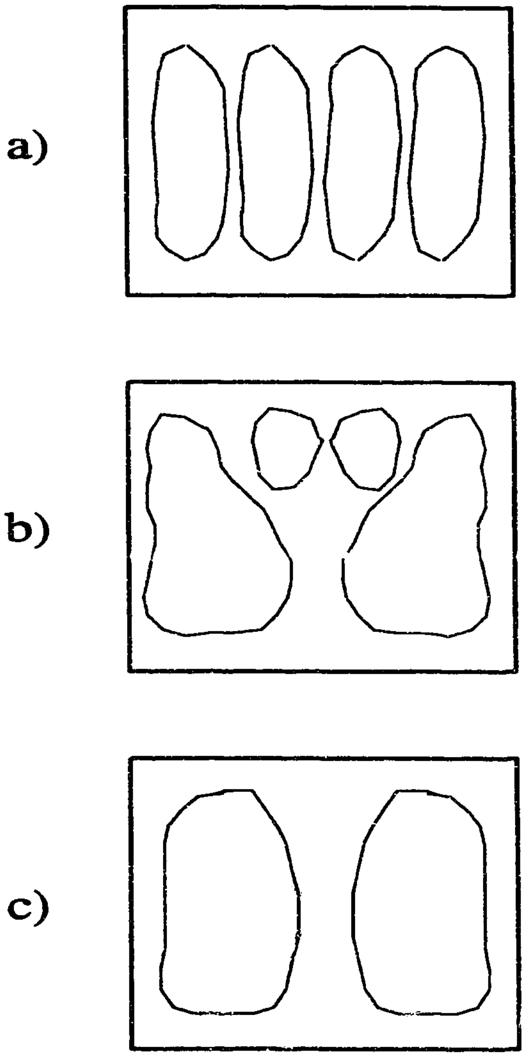

Figure 6.5: Transient Behaviour Observed in the Evolution of a Two-Cell Steady Flow from Rest

obtain a stable flow which corresponds to this branch.

The raw experimental data and information on the data reduction procedure is given in Appendix B. A plot of the numerical and experimental data for the region $Gr < 400000$ is shown in Figure 6.6.

The experimental temperatures within the fluid do not match very well with those in the numerical results. A possible explanation for this involves the manner in which the temperature within the fluid was measured. All measurements involve the disturbance of that which is to be measured. The difference is in the degree of the disturbacne caused by the measurement. Some techniques, such as holography and other optical methods, have a minimal effect on the system. In the case of the method used to determine the temperature at one point within the test fluid, the disturbance turned out to be quite large. It was necessary to place a thermocouple into the fluid. Since the gap is very thin, the fluid cannot flow around the thermocouple. The thermocouples used in this study were grounded at their tip. Fluid passing by the thermocouple would be a mixture of cooler fluid packets from near the wall of the cell, and other packets that were originally near the measurement point. The result is a measured temperature which is much cooler than expected.

This method of determining temperatures has an important effect. When the thermocouple used to measure the temperature inside the fluid is removed from the test region, secondary flow cells may be induced within the fluid. The inclusion of the thermocouple within one fill hole forces a small amount of test fluid up into the other fill hole. As the thermocouple is removed, the fluid within the fill hole returns to the test cell. The result is a vertical flow in a region where only horizontal flow lines exist in a two-cell flow pattern. This disturbance results in the creation of smaller flow cells near the fill holes.

For several of the experimental runs, the insertion and removal of the

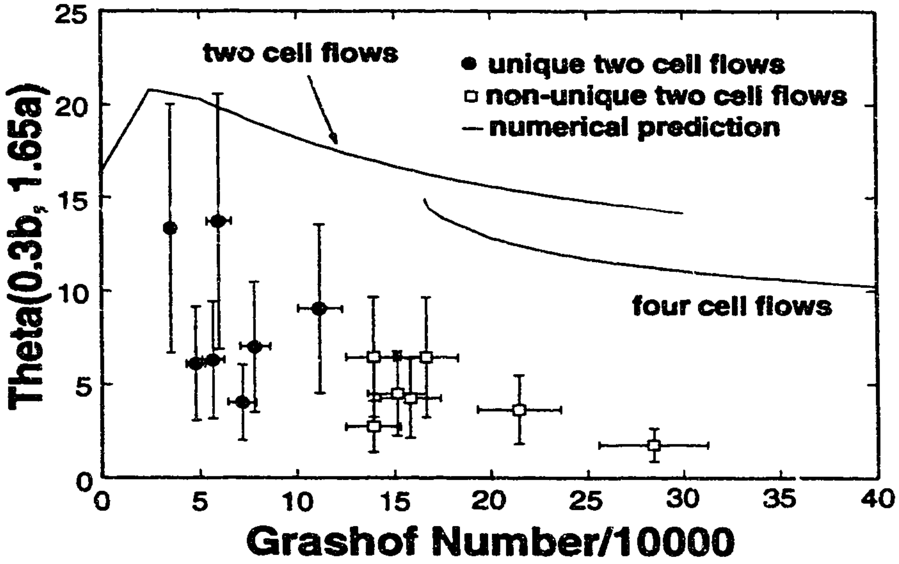

Figure 6.6: Experimental Two Cell Flows within the Hele-Shaw cell. $\phi = 0°, \gamma = 1.0$

thermocouple did not cause any change in the observed flow pattern. The disturbance quickly dissipated after the thermocouple was removed. These points are indicated by filled circles in Figure 6.6. This region corresponds to the unique solution region of the domain, where the only solution is this stable two cell flow pattern. Such a flow pattern is shown in Figure 6.7. The end of the unique solution region occurs at limit point L1. Beyond L1, there are three possible solutions. The numerical solution predicts the Grashof number at L1 to be 165591. In the experimental work, no unique solution was obtained for $Gr > 138000$. There is a 16% difference in these two values, which is within the experimental error of the Grashof number. This result verifies that the transition from the unique solution region to a multiple solution region is near the parameter set predicted by the mathematical model.

In other cases, observation of the test cell for several hours after the removal of the thermocouple showed that no flow pattern became stable. Several four cell flow flow patterns were apparent within the cell. A photo of one of these states also appears in Figure 6.7. This region, where a two cell flow pattern was stable and a perturbation caused an unstable four-cell flow pattern, corresponds with the parameter set between limit points L1 and L2. In this region of parameter space, the mathematical model predicts three possible solutions. One solution is a stable two-cell flow, the second is an unstable two-cell flow, while the third is a conditionally stable four-cell flow. The range of Grashof numbers in this region found experimentally is $139000 < Gr < 284000$, while the region between L1 and L2 predicted by numerical simulation is $165991 < Gr < 300034$.

In the region beyond $Gr = 283000$, no experimental data is shown in Figure 6.6, as no stable two-cell flow pattern was found. Only four-cell flow patterns could be found, and no stable flow pattern was obtained. The discrepancy between the

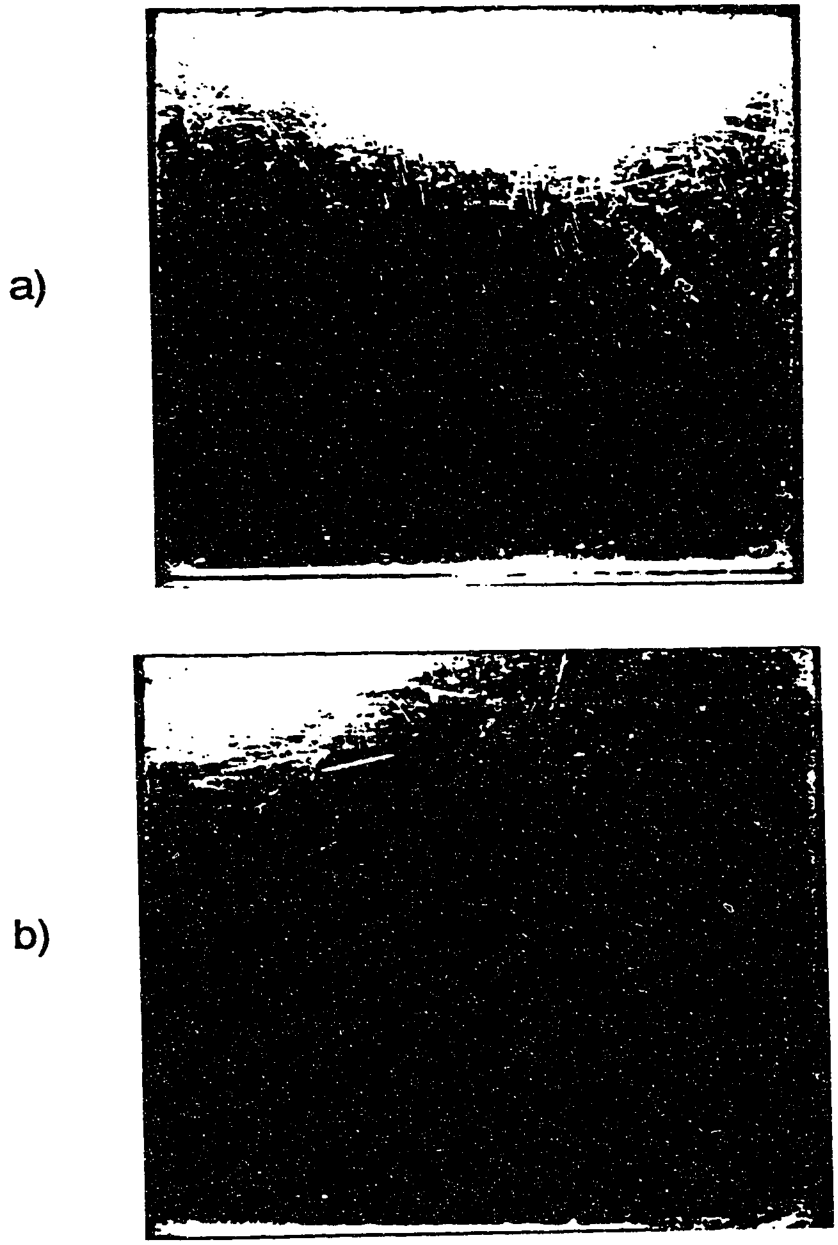

Figure 6.7: Flow Visualizations within the Hele-Shaw Cell, a) stable two-cell flow, b) one unstable four cell-flow pattern. $\phi = 0^\circ, \gamma = 1.0, Gr = 158000$

numerical prediction of L2 and the observed transition between the presence and absence of a stable two-cell flow is approximately 6%. Such a difference is well within the error calculated for the Grashof number.

The failure to obtain a stable four-cell flow pattern within the experimental apparatus is due to the inability to produce uniform internal heating. The temperature variations within the fluid, even at steady state, causes a significant variation in the amount of heating that occurs at various points within the fluid. In addition, inhomogeneity of the solution may cause nonuniform heating. Improper mixing during the preparation of the solution may have introduced a significant amount of air into the solution. The presence of the polystyrene beads is another factor contributing to imhomogeneity. Such substances would cause a variation in thermal conductivity within the solution that would generate a nonuniform internal heating.

6.5.3 Tilted Layers

Flow visualizations were also performed for Hele-Shaw cells which were tilted. A visualization at a tilt angle of 29° was performed, and its results are shown in Figure 6.8. A strong, asymmetric two cell flow was present. Attempts to perturb this flow and find another flow pattern were unsuccessful. This is not surprising, since the limit point L1 does not exist until $Gr = 409600$. Producing a state with such a Grashof number was not attempted, as the heat input necessary would require voltage and current values which would be beyond the capacity that the apparatus was designed to handle.

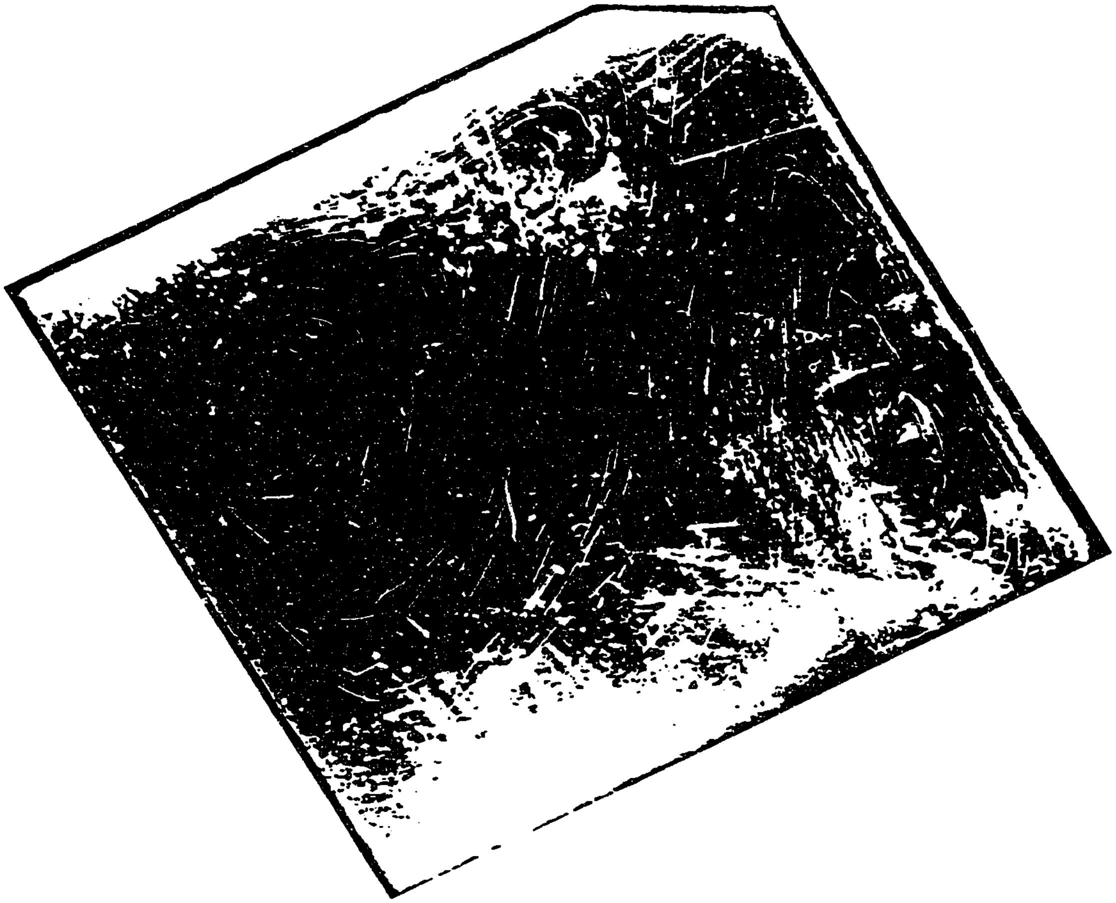

Figure 6.8: Flow Visualization for a Tilted Hele-Shaw Cell, $Gr = 163000, \phi = 29°, \gamma = 1.0$

Chapter 7

Conclusions and Recommendations

There were three objectives in the study outlined in this dissertation. The first was to consider the effect of tilt on the bifurcation diagram for steady state natural convection within a porous slab saturated with a single phase fluid. Another goal was to develop the bifurcation diagram for steady natural convective heat transfer within a thin fluid layer. In both cases, the convection was driven by the presence of internal heat sources. Previous authors have determined situations where flow within a thin fluid layer is an acceptable substitute for flow within a porous layer. Here, bifurcation diagrams for the two layers were generated. Qualitative and quantitative comparison of the two diagrams indicated the strength of the analogy between these two similar systems. Finally, an experimental of the Hele-Shaw cell was performed. Through flow visualization, a set of parameters where two stable solutions exist in the flow within the thin fluid layer was found. This discovery comfirmed the prediction from the computer simulations.

7.1 Porous Layer

There is a significant change in the bifurcation diagram for a thin porous slab when the system is subjected to tilt. A diagram of the heat transfer for an untilted slab contains one primary symmetric branch, two isolated symmetric branches and six asymmetric solution branches. When the slab is tilted to an angle of only one degree, significant change in the bifurcation diagram is evident. A primary solution branch remains, but there are seven isolated solution branches. All solution branches in the tilted domain are asymmetric, as all symmetry within the system has been broken. With increasing tilt, these isolated branches move to higher Rayleigh numbers. In the case of a slab with unit aspect ratio and tilt of 45°, the primary branch is unique and globally stable.

Numerical simulation of the porous slab also resulted in the discovery of three new asymmetric solution branches in the untilted bifurcation structure. These branches were discovered in the course of study of the effects of tilt on the domain.

As the porous slab was tilted, several regions were discovered where dynamic studies could be focussed. With tilt, symmetry-breaking points unfolded into limit points. This phenomenon led to origins of Hopf bifurcations. These tended to occur at tilt angles which are too small to be measured accurately. Their presence can be confirmed through comparison with dynamic simulations and stability calculations. Within the tilted structure there are branches that become unstable without a detectable bifurcation point in the vicinity. This change in stability may be due to the movement of the path of oscillatory solutions past the stationary branch. A routine to follow a path of oscillatory solutions through the domain is not available at this time, so confirmation of this conjecture is impossible.

Additional B-points were found by following the locus of limit point positions with varying tilt. In the case of three limit points, L6, L8 and L10, these B-points were in close proximity to a discontinuity in the fold curve. Consideration of the flow patterns near these discontinuities indicated that a change in the number of flow cells was occurring. The region around these discontinuites and B-points should be investigated further, as some interesting dynamic behavoiur could be found here.

7.2 Fluid Layer

A mathematical model for the convective heat transfer driven by internal heating within a thin fluid layer was developed. Simulations with this model gave a bifurcation diagram similar to that found with a fluid saturated porous slab, but with several key differences. The structure for an untitled layer contains a primary symmetric branch, two isolated symmetric branches and five asymmetric branches. Many of these branches corresponded to those found within the porous bifurcation diagram, but some did not. The major difference was a small asymmetric branch which links the two symmetric solution branches.

Within the fluid layer model was an inertia parameter which represents a difference between the behaviours in the porous layer and the fluid layer. Limit points in the fluid layer structure were tracked with varying inertia parameter. It was determined that the bifurcation diagram of the porous structure could be viewed as a special case of fluid layer behaviour when the inertia parameter tends toward zero. In terms of bifurcation points, the porous layer structure provides limiting values for the fluid layer as the gap width approaches zero. This may be seen as a quantitative measure of the similarities of the two bifurcation diagrams. Inspection of plots using dimensionless temperature as a state parameter shows strong qualitative evidence that a fluid layer behaves in a similar manner to a porous slab. Therefore, in terms of bifurcation structure, a thin fluid layer is a reasonable substitute for a porous layer.

As was the case for the porous layer, several B-points were discovered. These are places to begin any future study of the dynamics of convective flow within an internally heated Hele-Shaw cell. Origins of Hopf bifurcations were discovered due to the unfloding of symmetry-breaking points into limit points. At larger tilt angles, B-points were again found on the fold curves of the limit points with tilt. The positions of these B-points corresponded closely with the positions of B-points found in the porous layer.

One major difference between the bifurcation diagrams in the two systems is due to stability factors. For an untilted system, the primary branch from the conduction state to L2 is stable in both cases. The section of the primary branch from L1 to the edge of the domain is unstable for the porous slab, but was found to be stable for the thin fluid layer. The result is that for the fluid layer there exists a region of two stable solutions.

The dynamics of flow in Hele-Shaw cells with internal heating should be considered. Several B-points have been located, which provide excellent places to begin such a study. When a numerical study of the dynamics is complete, a comparison with existing dynamic simulations of porous layers with internal heating would be in order. Such a comparison would be another significant contribution to the study of situations where thin fluid layers can be substituted for porous layers. In addition, experimental study of the dynamics within a Hele-Shaw cell where internal heating drives the convection is possible.

7.3 Experimental Program

An experimental apparatus was constructed to correspond with the fluid layer simulated. The main objective was to determine if the conditionally stable section of branch PM1 could be observed experimentally. If so, then a region of two stable solutions with one set of parameters could be verified. Flow visualization was used to determine the flow patterns found within the test region. However, the four-cell flow pattern was not stable in the experimental apparatus. This implies an asymmetric perturbation exists within the apparatus. The most probable cause of this asymmetry is variation in the internal heating within various sections of the fluid layer.

The positions of limit points L1 and L2 were verified for an untilted layer. The presence of L1 indicates the end of the unique solution region. For all experimental measurements where $Gr < 138000$, perturbation of the two-cell flow pattern present did not result in any significant change. In a very short time, the perturbation died out, and the two-cell flow was restored. The numerical solution indicated that L1 was present at a Grashof number of 165991 for an untilted layer. For the experimnetal runs where $138000 < Gr < 283000$, perturbation of the two-cell flow gave rise to a four-cell flow pattern. However, this four-cell flow was unstable. Several different flow patterns were observed, but none remained within the cell for more than 10 minutes. For all experimental points with a Grashof number above 283000, no stable flow pattern was evident. Beyond the limit point L2, there is no stable two-cell flow. In the case [illegible] both L1 and L2, the numerical predictions for the limit points were within the experimental error of the Grashof numbers where the transitions were observed to occur.

Flow patterns at other tilt angles were found through flow visualization as well.

The two cell flow patterns expected at the parameter set investigated were observed. It must be noted that the velocity of the fluid was very slow. Any difference in density between the fluid and the polystyrene beads resulted in the beads having a terminal velocity of the same order of magnitude as the flows being visualized.

Some improvements could be made to the experimental setup. Instead of determining temperatures within the fluid by inserting a thermocouple into the flow, interferometry or another form of non-intrusive temperature sensation should be used. If higher heat inputs were required for future study, another cooling water channel should be cut into the copper block. Another improvement in the apparatus would be to drill two additional fill holes in the top of the copper block. This would facilitate the removal of air bubbles from the fluid layer.

An experimental study of the dynamics would be difficult with the experimental setup used here. The flows are very slow within the cell, especially at low heat inputs. In order to induce swifter flows without significant increase in the heating, a slightly wider gap is a reasonable alternative. A small change of the gap width would also cause a large decrease in the value of Grashof number for all bifurcation points. Increasing the gap width must be done with care, as a fluid layer which is too thick jeopardizes the use of the small gap approximation in the mathematical model.

References

[1] J. N. Koster and U. Müller. Free convection in vertical gaps. *Journal of Fluid Mechanics*, 125:429, 1982.

[2] J. N. Koster and U. Müller. Oscillatory convection in vertical slots. *Journal of Fluid Mechanics*, 139:363, 1984.

[3] H. J. Weinitschke, K. Nandakumar, and S. Ravi Sankar. A bifurcation study of convective heat transfer in porous media. *Physics of Fluids A*, 2:912, 1990.

[4] L. Buhler, P. Erhard, C. Gunther, U. Müller, and G. Zimmerman. Natural convection in vertical gaps heated at the lower side - an experimental and numerical study. In *Bifurcation Phenomena in Thermal Processes and Convection*, page 67, 1987.

[5] Lord Rayleigh. On convective currents in a horizontal layer of fluid when the higher temperature is on the under side. *Phil. Mus.*, 32:529, 1916.

[6] H. Bénard. Les tourbillons cellulaires dans une nappe liquide, methods optiques d'observation et d'enrigistrement. *Journale de Physique*, 10:254, 1901.

[7] A. Pellew and R. V. Southwell. On maintained convective motion in a fluid

layer heated from below. *Proceedings of the Royal Society of London (A)*, 176:312, 1940.

[8] W. V. F. Malkus and G. Veronis. Finite amplitude cellular convection. *Journal of Fluid Mechanics*, 4:225, 1958.

[9] E. Palm. On the tendency toward hexagonal cells in steady convection. *Journal of Fluid Mechanics*, 8:183, 1960.

[10] L. Segal and J. T. Stuart. On the question of the prefered mode in cellular thermal convection. *Journal of Fluid Mechanics*, 13:289, 1962.

[11] A. Schlüber, D. Lortz, and F. Busse. On the stability of steady finite amplitude cellular convection. *Journal of Fluid Mechanics*, 23:129, 1965.

[12] R. Krishnamurti. On the transition to turbulent convection. part 1: The transition from two- to three-dimensional flow. *Journal of Fluid Mechanics*, 42:295, 1970.

[13] R. Krishnamurti. On the transition to turbulent convection. part 2: The transition to time-dependent flow. *Journal of Fluid Mechanics*, 42:309, 1970.

[14] W. Arten and A. C. Newell. Numerical simulation of Rayleigh-Bénard convection in shallow tanks. *Physics of Fluids*, 31:2474, 1988.

[15] S. Chandrasekhar. *Hydrodynamic and Hydromagnetic Stability*. Clarendon, Oxford, 1961.

[16] D. J. Tritton and M. N. Zarraga. Convection in horizontal layers with internal heat generation. *Journal of Fluid Mechanics*, 30:21, 1967. Part 1.

[17] P. H. Roberts. Convection in horizontal layers with internal heat generation. theory. *Journal of Fluid Mechanics*, 30:33, 1967. Part I.

[18] R. Thirlby. Convection in an internally heated layer. *Journal of Fluid Mechanics*, 44:673, 1970. Part IV.

[19] E. W. Schwiderski and H. J. A. Schwab. Convection experiments with electrolytically heated fluid layers. *Journal of Fluid Mechanics*, 48:78, 1971. Part IV.

[20] F. A. Kulacki and R. J. Goldstein. Thermal convection in a horizontal fluid layer with uniform volumetric energy sources. *Journal of Fluid Mechanics*, 55:271, 1972.

[21] F. A. Kulacki and M. E. Nagle. Natural convection in a horizontal fluid layer with volumetric energy sources. *ASME Journal of Heat Transfer*, 97:204, 1975.

[22] M. Tveitereid and E. Palm. Convection due to internal heat sources. *Journal of Fluid Mechanics*, 76:481, 1976. Part III.

[23] F. B. Cheung. Natural convection in a volumetrically heated fluid layer at high Rayleigh number. *International Journal of Heat and Mass Transfer*, 20:499, 1977.

[24] F. B. Cheung. Correlation equation for turbulent thermal convection in a horizontal fluid layer heated internally and from below. *ASME Journal of Heat Transfer*, 100:416, 1978.

[25] P. Boo-Long, T. W. Lester, and R. E. Faw. Convective heat transfer in an internally heated horizontal fluid layer with unequal boundary temperatures. *International Journal of Heat and Mass Transfer*, 22:437, 1979.

[26] Y. Kikuchi, T. Kawasaki, and T. Shioyama. Thermal convection in a horizontal fluid layer heated internally and from below. *International Journal of Heat and Mass Transfer*, 25:363, 1982.

[27] H. S. Hele Shaw. Investigation of the nature of surface resistance of water and of streamline motion under certain experimental conditions. *Trans. Instn. Nav. Archit.*, 40:21, 1898.

[28] R. A. Wooding. Instabilities of a viscous liquid of variable density in a vertical Hele-Shaw cell. *Journal of Fluid Mechanics*, 7:501, 1960.

[29] B. K. Hartline and C. R. B. Lister. Thermal convection in a Hele-Shaw cell. *Journal of Fluid Mechanics*, 79:379, 1977.

[30] O. Kvernvold. On the stability of non-linear convection in a Hele-Shaw cell. *International Journal of Heat and Mass Transfer*, 22:395, 1979.

[31] H. Frick and R. M. Clever. The influence of side walls on finite-amplitude convection in a layer heated from below. *Journal of Fluid Mechanics*, 114:467, 1982.

[32] J. N. Koster, P. Ehrhard, and U. Müller. Nonsteady end effects in Hele-Shaw cells. *Physical Review Letters*, 56:1802, 1986.

[33] C.-W. Park and G. M. Homsy. Two-phase displacement in Hele-Shaw cells. *Journal of Fluid Mechanics*, 139:291, 1984.

[34] A. R. Kopf-Sill and G. M. Homsy. Bubble motion in a Hele-Shaw cell. *Physics of Fluids*, 31:18, 1988.

[35] A. Pumir and H. Aref. A model of bubble dynamics in a Hele-Shaw cell. *Physics of Fluids*, 31:752, 1988.

[36] A. R. Kopf-Sill and G. M. Homsy. Non-linear unstable viscous fingers in Hele-Shaw flows. 1. Experiments. *Physics of Fluids*, 31:242, 1988.

[37] A. R. Kopf-Sill and G. M. Homsy. Non-linear unstable viscous fingers in hele-shaw flows. 2. Numerical simulation. *Physics of Fluids*, 31:429, 1988.

[38] S. Tanveer and P. G. Saffman. The effect of nonzero viscosity ratio on the stability of fingers and bubbles in a Hele-Shaw cell. *Physics of Fluids*, 31:3188, 1988.

[39] J. M. Aitchison and S. D. Howison. Computation of Hele-Shaw flows with free boundaries. *Journal of Computational Physics*, 60:376, 1985.

[40] S.-H. Hwang and H.-C. Chang. Non-Boussinesq effects on transitions in Hele-Shaw convection. *Physics of Fluids A*, 1:924, 1989.

[41] C. W. Horton and F. T. Rogers. Convection currents in a porous medium. *Journal of Applied Physics*, 16:367, 1945.

[42] E. R. Lapwood. Convection of a fluid in a porous medium. *Proc. Camb. Phil. Soc.*, 44:508, 1948.

[43] Y. Katto and T. Masuoka. Criterion for the onset of convective flow in a fluid in a porous medium. *International Journal of Heat and Mass Transfer*, 10:297, 1967.

[44] V. Prasad and F. A. Kulacki. Convective heat transfer in a rectangular porous cavity - effect of aspect ratio on flow structure and heat transfer. *ASME Journal of Heat Transfer*, 106:158, 1984.

[45] J. P. Caltagirone and S. A. Bories. Solutions and stability criteria of natural convective flow in an inclined porous layer. *Journal of Fluid Mechanics*,

155:267, 1985.

[46] R. J. Buretta. *Thermal convection in a fluid-filled porous layer with uniform internal heat sources.* PhD thesis, University of Minnesota, 1972.

[47] V. Prasad, F. A. Kulacki, and M. Keyhani. Natural convection in porous media. *Journal of Fluid Mechanics*, 150:89, 1985.

[48] V. Prasad and F. A. Kulacki. Natural convection in porous media bounded by short concentric vertical cylinders. *ASME Journal of Heat Transfer*, 107:147, 1985.

[49] B.-X. Wang and X. Zhang. Natural convection in liquid-saturated porous media between concentric inclined cylinders. *International Journal of Heat and Mass Transfer*, 33:827, 1990.

[50] V. Prasad and F. A. Kulacki. Natural convection in a rectangular porous cavity with constant heat flux on one vertical wall. *ASME Journal of Heat Transfer*, 106:152, 1984.

[51] D. Poulikakos. A departure from the darcy model in boundary layer natural convection in a vertical porous layer with uniform heat flux from the side. *ASME Journal of Heat Transfer*, 107:716, 1985.

[52] M. Sen, P. Vasseur, and L. Robillard. Parallel flow convection in a tilted two-dimensional porous layer heated from all sides. *Physics of Fluids*, 31:3480, 1988.

[53] S. Kimura, A. Bejan, and I. Pop. Natural convection near a cold plate facing upward in a porous medium. *ASME Journal of Heat Transfer*, 107:819, 1985.

[54] R. M. Islam and K. Nandakumar. Mixed convection heat transfer in porous media in the non-Darcy regime. *Canadian Journal of Chemical Engineering*, 66:68, 1988.

[55] W.-J. Chang and J.-Y. Jang. Inertia effects on vortex instability of a horizontal natural convection flow in a saturated porous medium. *International Journal of Heat and Mass Transfer*, 32:541, 1989.

[56] K. Vafai and C. L. Tien. Boundary and inertia effects on flow and heat transfer in porous media. *International Journal of Heat and Mass Transfer*, 24:195, 1981.

[57] W.-J. Chang and J.-Y. Jang. Non-Darcian effects on vortex instability of a horizontal natural convection flow in a porous medium. *International Journal of Heat and Mass Transfer*, 32:529, 1989.

[58] P. Vasseur, C. H. Wang, and M. Sen. The brinkman model for natural convection in a shallow porous cavity with uniform heat flux. *Numerical Heat Transfer, Part A*, 15:221, 1989.

[59] R. McKibben and P. A. Tyvand. Thermal convection in a porous medium composed of alternating thick and thin layers. *International Journal of Heat and Mass Transfer*, 26:761, 1983.

[60] A. Bejan. Natural convection heat transfer from a circular cylinder a saturated porous medium. *International Journal of Heat and Mass Transfer*, 26:815, 1983.

[61] S. Kimura. Transient forced convection heat transfer from a circular cylinder in a saturated porous medium. *International Journal of Heat and Mass Transfer*, 32:192, 1989.

[62] S. J. Kim and K. Vafai. Analysis of natural convection about a vertical plate embedded in a porous medium. *International Journal of Heat and Mass Transfer*, 32:665, 1989.

[63] R. N. Horne and M. J. O'Sullivan. Oscillatory convection in a porous medium heated from below. *Journal of Fluid Mechanics*, 66:339, 1974. Part 2.

[64] S. Kimura, G. Schubert, and J. M. Straus. Route to chaos in porous-medium thermal convection. *Journal of Fluid Mechanics*, 166:305, 1986.

[65] P. Steen and C. K. Aidun. Time-periodic convection in porous media. *Journal of Fluid Mechanics*, 196:263, 1988.

[66] D. A. S. Rees and D. S. Riley. The effects of boundary imperfection on convection in a saturated porous layer: Near resonant wavelength excitation. *Journal of Fluid Mechanics*, 133:133, 1989.

[67] S. A. Bories, M. Combarnous, and J. Y. Jaffrennou. Observation des differentes formes d'ecoulements thermoconvectifs dans une couche poreuse inclinee. *C. R. Acad. Sci., Ser. A.*, 275:857, 1972.

[68] J. P. Caltagirone, M. Cloupeau, and M. A. Combarnous. Convection naturelle fluctuante dans une couche poreuse horizontale. *C. R. Acad. Sci. Paris, Ser. B*, 273:833, 1971.

[69] S. A. Bories and M. A. Combarnous. Natural convection in a sloping porous layer. *Journal of Fluid Mechanics*, 57:63, 1973.

[70] M. A. Combarnous and S. A. Bories. Hydrothermal convection in saturated porous media. *Advances in Hydroscience*, 10:237, 1975.

[71] H. Inaba and N. Seki. Transient behaviors of natural convective heat transfer through a vertical porous slot. *Applied Science Resources*, 37:257, 1981.

[72] J. G. Georgiadis and I. Catton. Free convective motion in an infinite vertical porous slot: The non-Darcian regime. *International Journal of Heat and Mass Transfer*, 28:2389, 1985.

[73] M. A. Combarnous. *Convection naturelle et convection mixte en mileu poreux.* PhD thesis, University of Paris, 1970.

[74] P. H. Holst and K. Aziz. A theoretical and experimental study of natural convection in a confined porous medium. *Canadian Journal of Chemical Engineering*, 50:232, 1972.

[75] P. H. Holst and K. Aziz. Transient three-dimensional natural convection in confined porous media. *International Journal of Heat and Mass Transfer*, 15:73, 1972.

[76] J. P. Walch and B. Dulieu. Convection de Rayleigh-Bénard dans une cavite poreuse faiblement inclinee. *Journal de Physiques Lettres*, 43:103, 1982.

[77] T. Kaneko, M. F. Mohtadi, and K. Aziz. An experimental study of natural convection in inclined porous media. *International Journal of Heat and Mass Transfer*, 17:485, 1974.

[78] M. A. Combarnous and S. A. Bories. Modelisation de la convection naturelle au sein d'une couche poreuse horizontale a l'aide d'un coefficient de transfert solide-fluide. *International Journal of Heat and Mass Transfer*, 17:505, 1974.

[79] Y. T. Chan and S. Banerjee. Analysis of transient three-dimensional natural convection in porous media. *ASME Journal of Heat Transfer*, 10:242, 1983.

[80] R. D. Gasser and M. S. Kazimi. Onset of convection in a porous medium with internal heat generation. *ASME Journal of Heat Transfer*, 98:49, 1976.

[81] R. J. Buretta and A. S. Berman. Convective heat transfer in a liquid saturated porous layer. *Journal of Applied Mechanics*, 43:249, 1976.

[82] M. Tveitereid. Thermal convection in a horizontal porous layer with internal heat sources. *International Journal of Heat and Mass Transfer*, 20:1045, 1977.

[83] F. Chen and C. F. Chen. Experimental investigation of convective stability in a superposed fluid and porous layer when heated from below. *Journal of Fluid Mechanics*, 207:311, 1989.

[84] T. Schulenberg and U. Müller. Natural convection in saturated porous layers with internal heat sources. *International Journal of Heat and Mass Transfer*, 27:677, 1984.

[85] D. Poulikakos. Thermal instability in a horizontal fluid layer superposed on a heat-generating porous bed. *Numerical Heat Transfer*, 12:83, 1987.

[86] K. J. Beukema, S. Bruin, and J. Schenk. Three-dimensional natural convection in a confined porous medium with internal heat generation. *International Journal of Heat and Mass Transfer*, 26:451, 1983.

[87] M. Haajizadeh and C. L. Tien. Combined natural and forced convection in a horizontal porous channel. *International Journal of Heat and Mass Transfer*, 27:799, 1984.

[88] R. M. Islam and K. Nandakumar. Multiple solutions for buoyancy induced flow in saturated porous media for large Peclet number. *ASME Journal of Heat Transfer*, 108:866, 1986.

[89] M. R. Islam and K. Nandakumar. Transient convection in saturated porous layers with internal heat sources. *International Journal of Heat and Mass Transfer*, 33:151, 1990.

[90] K. Nandakumar and H. J. Weinitschke. A bifurcation study of mixed-convection heat transfer in horizontal ducts. *Journal of Fluid Mechanics*, 231:157, 1991.

[91] K. H. Winters. A bifurcation study of laminar flow in a curved tube of rectangular cross-section. *Journal of Fluid Mechanics*, 180:343, 1987.

[92] K. S. Ball and B. Farouk. Bifurcation phenomena in Taylor-Couette flow with buoyancy effects. *Journal of Fluid Mechanics*, 197:479, 1988.

[93] K. A. Cliffe and K. H. Winters. A numerical study of the cusp catastrophe for B'enard convection in tilted cavities. *Journal of Computational Physics*, 54:531, 1984.

[94] D. S. Riley and K. H. Winters. A bifurcation study of convection in a two-dimensional saturated porous cavity. In *Bifurcation Phenomena in Thermal Processes and Convection*. American Society for Mechanical Engineering, 1987. Winter Annual Meeting.

[95] D. S. Riley and K. H. Winters. Modal exchange mechanisms in Lapwood convection. *Journal of Fluid Mechanics*, 204:325, 1989.

[96] D. K. Ryland and K. Nandakumar. A bifurcation study of convective heat transfer in porous media. part II. Effect of tilt on stationary and nonstationary solutions. *Physics of Fluids A*, 4:1945, 1992.

[97] E. Chu, A. George, J. Liu, and E. Ng. Sparspak. Technical Report CS-84-36, Department of Computer Science, University of Waterloo, 1984.

[98] G. Moore and A. Spence. The calculation of turning points of nonlinear equations. *SIAM Journal on Numerical Analysis*, 17:567, 1980.

[99] H. J. Weinitschke. On the calculation of limit and bifurcation points in stability problems of elastic shells. *International Journal of Solids and Structures*, 21:79, 1985.

[100] B. Werner and A. Spence. The computation of symmetry-breaking bifurcation points. *SIAM Journal on Numerical Analysis*, 21:388, 1984.

[101] D. Roose and B. de Dier. Numerical determination of an emanating branch of Hopf bifurcation points in a two-parameter problem. *SIAM Journal of Scientific Statistical Computation*, 10:671, 1989.

[102] H. B. Keller. Continuation methods in computational fluid dynamics. In T. Cebeci, editor, *Numerical and Physical Aspects of Aerodynamic Flows*. Springer, 1981.

[103] S. S. Vorontsov, A. V. Gorin, V. Ye. Nakoryakov, A. G. Khoruzhenko, and V. M. Chupin. Natural convection in a hele-shaw cell. *International Journal of Heat and Mass Transfer*, 34:703, 1991.

[104] B. Bara. *Experimental investigation of developing and fully developed flow in a curved duct of square cross section*. PhD thesis, University of Alberta, 1991.

[105] M. Buffat and D. Henry. Numerical simulation of 3D instabilities in liquid metal by a finite element method. In *Numerical Methods for Thermal Problems, Part VII*, page 488, 1991.

[106] H. Schenck. *Theories of Engineering Experimentation*. McGraw Hill, 3rd edition, 1979.

[107] Robert C. Weast, editor. *CRC Handbook of Chemistry and Physics*, pages D–231, E–10, F–5, F–38. CRC Press, 64th edition, 1983.

Appendix A

Method of Uncertainty Analysis

To estimate the uncertainty of the variables in the experimental study, a method based on the equation used to determine the value of the variable is employed. For any calculated variable $Y = f(A, B, C, D)$, the uncertainty in Y can be determined using the uncertainties in the quantities A, B, C and D, which are known from measurements. If the total derivative of Y is determined, the result is:

$$dY = \frac{\partial f}{\partial A}dA + \frac{\partial f}{\partial B}dB + \frac{\partial f}{\partial C}dC + \frac{\partial f}{\partial D}dD \tag{A.1}$$

If the errors in the quantities are small, the term dY may be replaced with ΔY to give:

$$\Delta Y = \frac{\partial f}{\partial A}\Delta A + \frac{\partial f}{\partial B}\Delta B + \frac{\partial f}{\partial C}\Delta C + \frac{\partial f}{\partial D}\Delta D \tag{A.2}$$

Equation A.2 cannot be used to determine ΔX, as the signs of the errors may be different and lead to an erroneous magnitude of error. To remove this difficulty, each term may be squared. This leads to the use of the mean squared error. If the measured quantities A, B, C and D are all statistically independent and symmetrically distributed random variables [106], the cross product terms vanish.

The resulting error relation is:

$$(\Delta Y)^2 = (\frac{\partial f}{\partial A}\Delta A)^2 + (\frac{\partial f}{\partial B}\Delta B)^2 + (\frac{\partial f}{\partial C}\Delta C)^2 + \frac{\partial f}{\partial D}\Delta D)^2 \tag{A.3}$$

As an example, consider a function for Y of the form:

$$Y = \frac{AB^m}{C^n D} \tag{A.4}$$

Taking the partial derivatives and substituting into equation A.3 results in:

$$\begin{aligned}(\Delta Y)^2 &= (\frac{B^m}{C^n D}\Delta A)^2 + (\frac{mAB^{m-1}}{C^n D}\Delta B)^2 \\ &+(\frac{nAB^m}{C^{N+1}D}\Delta C)^2 + (\frac{AB^m}{C^n D^2}\Delta D)^2\end{aligned} \tag{A.5}$$

Dividing by equation A.4 gives the following relation for the fractional uncertainty in the calculated variable Y:

$$(\frac{\Delta Y}{Y})^2 = (\frac{\Delta A}{A})^2 + (\frac{m\Delta B}{B})^2 + (\frac{n\Delta C}{C})^2 + (\frac{\Delta D}{D})^2 \tag{A.6}$$

For any variable determined from a functional relation of the form of equation A.4, the fractional uncertainty of the variable can be expressed as an equation of the form of equation A.6. Any exponent of the measured variables ends up as a weighting factor in the fractional uncertainty.

Appendix B

Raw Experimental Data and Data Reduction

The raw data taken from the experimental apparatus is outlined in Tables B.1 and B.2. Reduction of the data was accomplished in the following manner. The model equations are scaled so that all temperature dependent quantities are evaluated at the temperature of the constant temperature walls. Values for the required physical properties of pure water are available from the *CRC Handbook of Chemistry and Physics* [107]. These properties are thermal conductivity, viscosity, density and coefficient of thermal expansion. All physical properties for the dilute copper sulfate solution are assumed to have similar temperature variations as does pure water. Values for the density and viscosity of copper sulfate solutions of various concentrations are also available, and these factors are also implemented. The amount of internal heating was determined by finding the product of current and voltage, and dividing by the volume of fluid in the cell. These are all the quantities needed to calculate the Grashof number and dimensionless temperature.

Untilted Fluid Layers						
Run	Voltage (Volts)	Current (Amps)	Wall Temp (C)	Fluid Temp (C)	Gr	theta
6-1	0.66	0.009	17.6	19.6	166600	6.42
9-1	0.79	0.004	15.5	17.6	60110	13.71
9-2	1.15	0.006	14.9	17.4	139100	6.43
10-2	[illegible]	0.004	19.5	21.2	112000	9.04
11-1	[illegible]	0.005	7.9	12.6	35070	13.34
11-2	1.58	0.008	7.5	11.8	57040	6.28
11-3	1.70	0.009	6.5	6.8	48120	6.07
11-4	1.94	0.010	6.8	11.3	71900	4.01
12-1	1.40	0.009	14.0	16.5	214600	3.65
12-2	1.57	0.010	14.2	15.8	284400	1.76
12-3	1.14	0.007	14.5	16.5	151500	4.49
13-1	0.54	0.004	13.4	16.3	31600	26.51
13-2	0.82	0.005	14.0	15.8	78500	6.99
13-3	1.03	0.007	14.6	15.8	139000	2.74
14-1	1.44	0.007	13.0	15.4	158100	4.24
Layer Tilted 29 Degrees						
14-2	1.45	0.007	13.0	—	163300	—

Table B.1: Raw Experimental Data and Calculated Results for Two-Cell Flow Patterns

Run	Voltage (Volts)	Current (Amps)	[illegible] (C)	Gr
1-1	1.68	0.065	22.8	314700
2-1	0.97	0.011	20.0	379400
2-2	1.26	0.014	19.6	599800
3-1	0.65	0.007	21.9	194100
5-1	1.01	0.013	21.4	547700
5-2	1.29	0.016	21.3	839400
6-2	0.66	0.009	17.4	167800
10-1	1.01	0.005	19.8	172300

Table B.2: Raw Experimental Data and Calculated Results for Four-Cell Flow Patterns in an Untitled Hele-Shaw Cell